UNDERSTANDING AND CALIBRATING THE DS-ECAL FOR T2K'S ND280

A Thesis in High Energy Physics

by

Gavin Davies
MPhys (Hons)

Submitted in partial fulfilment
of the requirements for the Degree of
Doctor of Philosophy

Department of Physics
Lancaster University

January 2011

No part of this thesis has been previously submitted for the award of a higher degree.

My religion consists of a humble admiration of the illimitable superior spirit who reveals himself in the slight details we are able to perceive with our frail and feeble mind.

–Albert Einstein

Dedicated to my parents

and my beautiful wife.

Table of Contents

List of Tables

List of Figures

Author's Contribution

Specific to the DS-ECal, I was responsible for much of the mechanical and optical quality assurance (QA) which was performed at Lancaster University on the plastic scintillator bars received from Fermilab. This is detailed in Chapter 5. Specifically, I was involved in performing the Mechanical QA of the scintillator bars and completing the subsequent analysis of the Mechanical QA results, the result of which is described in detail in Appendix A. I also helped to produce the optical QA setup at Lancaster University and carried out all of the optical QA tests, producing the analysis results in turn. The mechanical and optical QA analysis results are all my own work.

I took a leading role in all aspects of the 2D scan work and systems integration, including assisting with development and testing of the procedures. I was fully responsible for the analysis and validation of the layer scans for the final third of the DS-ECal layers. Most signifcantly however are the many hours that I spent improving the techniques and methods employed during the construction of the DS-ECal. I was able to pass on my knowledge and experience garnered during this phase to collaborators working on the construction of subsequent ECal modules.

During the beam tests that are discussed in Chapter 7 I participated both in the data-taking and data analysis at CERN. I produced hit distribution maps in order to aid with the identificaton of hot and 'dead' channels.

Using cosmic ray data that was also collected whilst the DS-ECal was at CERN, I worked to produce attenuation constants to feed into the calibration chain for the detector. I developed and was responsible for a track reconstruction algorithm that calculated attenuation calibration constants in collaboration with a colleague. The code will be further developed in the future to calculate constants for all ECal modules in T2K's ND280. The algorithm's method and results are described in Chapter 8.

Abstract

The T2K (Tokai to Kamioka) experiment is an off-axis long-baseline neutrino oscillation experiment with a baseline of 295 km to the Super-Kamiokande far detector. The near detector, ND280, measures the flux and energy spectra of electron and muon neutrinos 280m from the muon neutrino beam source. Electromagnetic calorimeters constructed from lead and plastic scintillator bars cover the largest active area in ND280. The most downstream calorimeter is the Downstream Electromagnetic Calorimeter (DS-ECal). This thesis details aspects of the construction and calibration of the DS-ECal.

Construction of the DS-ECal and quality assurance of the scintillator bars was performed at Lancaster University. All scintillator bars that were selected for optical quality assurance tests were accepted for use in the construction of the DS-ECal. Each bar that was tested was shown to have a light yield within $\sim 2\sigma$ of the mean light yield of 35.9 ± 4.9 photoelectrons per minimum-ionising particle, measured at 66 cm from the scintillator bar end with three wavelength-shifting fibres coupled to a photomultiplier readout.

Cosmic ray data collected at CERN, upon the successful construction of the DS-ECal, was used to develop a simple track-selection algorithm that reconstructed the position of charge deposits in the DS-ECal. The resulting attenuation profiles of all bars have been demonstrated to be consistent with one another within uncertainties using a developed quadruple-exponential function that describes the attenuation of the detected light along the length of the DS-ECal scintillator bars both quantitatively and qualitatively. The attenuation length of light traveling along the length of scintillator bars within the calorimeter has been measured to be 341 ± 90 cm. This is consistent with expected values of the order of 350 cm for Y11 WLS fibres.

The Tokai ($in - situ$) and CERN cosmic ray data are also shown to be consistent with within approximately 1% as calculated from the mean most probable value of a convoluted Landau-Gaussian distribution of charge hits at several positions along the bars for all channels in the detector combined. The DS-ECal is currently collecting neutrino data for inclusion in the T2K 2010a physics run and is in good working order with only 11 dead channels from a total of 3400.

Abbreviations

APD Avalanche Photodiode

CCQE Charged Current Quasi-Elastic

CR Cosmic Ray

DS-ECal Downstream Electromagnetic Calorimeter

FNAL Fermi national Accelerator Laboratory

FGD Fine Grained Detector

MPPC Multi-Pixel Photon Counter

NC Neutral Current

TPC Time Projection Chamber

PDE Photon Detection Efficiency

PE Photo-electron

P0D Pi-Zero Detector

QA Quality Assurance

RMM Readout Merger Module

SMRD Side Muon Range Detector

SNP Solar Neutrino Problem

SPE Single Photo-electron

TFB Trip-t Frontend Board

WLS Wavelength-Shifting Fibre

Acknowledgements

Thank you to Laura Kormos and Iain Bertram for getting me to the end. Your patience and support has been invaluable. I am indebted to you for accomplishing everything that I have on T2K. I especially thank Laura and her continued perseverance in her attempts to turn me into a Physicist.

I thank everyone in T2K for your help and advice throughout my thesis.

I would also like to thank everybody in the Lancaster HEP group, in particular Peter Ratoff for making this PhD happen in the first place and securing my financial support. Thank you to Alex Finch for continued computing and intellectual support and Alex Chilingarov who is a fountain of knowledge. Thanks go to Ian Mercer with apologies too. City will never win the League as long as there is a Red half to Manchester. I owe a huge thanks to Athanasios Hatzikoutelis for all of the banter and for encouraging me at every turn, not forgetting the fact that you allowed me to introduce you to some real English culture.

I also thank Tom Maryon for listening to all of my moaning and for help getting to grips with the T2K software. Thanks to Steve Bentham for getting me to collaboration meetings early and on time and the spam recipes.

I would like to thank the Lancaster University Physics Department for its financial support during this thesis, and I thank the Faculty of Science and Technology for helping to fund my travels to conferences.

I thank my Mum, Dad, sister Kirsty, brother Andy and my Grandparents for your continued love and support and without whom this would be meaningless. I also thank Larry and Joanette for accepting me into their family.

Finally, my biggest thank you is reserved for my wonderful wife for your continued understanding and support. Thank you for believing in me!

Chapter 1

Introduction

This thesis will walk you through most aspects of bringing to life a particle detector, in particular an Electromagnetic Calorimeter (ECal). It will summarise how it is possible to achieve the objective of reconstructing a physics event in an ECal and ultimately to be in a position to measure the energy of the particles that are involved in said physics event.

The T2K experiment, discussed in Chapter 3, is a second-generation long-baseline neutrino oscillation experiment designed to measure parameters of the Maki-Nakagawa-Sakata-Pontecorvo (MNSP) matrix that governs the mathematical mechanism by which neutrinos oscillate. Chapter 2 will discuss the history of the neutrino and subsequently the mathematical formalisms that govern neutrino oscillations. The experiment primarily intends to determine the mixing angle θ_{13} via the observation of ν_e appearance from a ν_μ beam. The ν_μ beam is directed 295 km to the Super-Kamiokande detector, the T2K far detector. A near detector suite is installed 280 m downstream from the beam source and consists of two detectors: the on-axis INGRID and off-axis ND280. The Downstream Electromagnetic Calorimeter (DS-ECal) is the most downstream of sub-detectors in the off-axis ND280 and is the primary focus of this thesis. The purpose, design and construction of the DS-ECal is discussed in Chapter 4. The complete construction of the DS-ECal was performed at Lancaster University. I was responsible for carrying out several phases of construction of the DS-ECal and the quality assurance of the scintillator bars, discussed in Chapter 5. I took a leading role in all aspects of the 2D scan work and systems integration, including assisting with development and testing of the procedures. Once the DS-ECal module construction was completed it spent a period of 3 months at Rutherford Appleton Laboratory collecting limited cosmic ray data during an initial commissioning phase. The DS-ECal was then transported to the East Hall area at CERN to undergo beam tests. The CERN

testbeam setup and my contribution in providing hit distribution maps to be able to identify hot channels and 'dead' channels quickly is discussed in Chapter 7. The hit maps also serve their purpose in checking the distribution of charge hits. Importantly for the work in this thesis, the DS-ECal collected cosmic ray data during the CERN testbeam period, which provided a sample of muons for commissioning and calibration of the final DS-ECal module system before proceeding to Tokai for integration into the ND280. The attenuation calibration of the system is discussed in Chapter 8. The attenuation correction study in Chapter 8 made use of the large CR data-set collected in the DS-ECal during time at CERN. The thesis culminates in a detailed study of the attenuation profiles of the detector channels in order to calculate an attenuation correction factor that can consequently be applied to correct the detected charge.

The experiment needs to be able to understand the neutrino energy spectrum at the T2K Far Detector, SuperKamiokande, with a precision of approximately 10%. This means that we need to measure the unoscillated neutrino spectrum at ND280 with a precision of better than 10%. The energy resolution provided by the ECal plays an important role in the ND280 off-axis detector to support the energy measurements made by the Time Projection Chambers (TPCs) for charged particles, and by providing an energy measurement for neutral particles. This will ultimately feed into the measurement of θ_{13} by the T2K experiment.

At the time of writing the DS-ECal is located in the ND280 detector suite collecting neutrino data as part of the T2K 2010a physics run.

Chapter 2

Neutrino Physics

2.1 History of the Neutrino

The idea of the neutrino was born in 1930 through Wolfgang Pauli's proposal [1] of the existence of an electrically neutral, spin-$\frac{1}{2}$ particle that would maintain the conservation laws in beta decay. We now are aware that one type of beta decay is the decay of a neutron into a proton with the emission of an electron and a (electron anti-) neutrino, but in 1930 the neutrino was not known. The problem in beta decay, at the time, was that the emitted electrons had an unexpected continuous distribution of energy. This violated the conservation laws governing energy and momentum for what was thought to be a two-body decay with the electron carrying all of the kinetic energy. In order to resolve this conflict, Pauli postulated that another particle, a chargeless, massless particle, must be produced by the beta decay to carry the missing energy. In 1932 James Chadwick discovered the neutron [2] which is chargeless. However, neutrons are heavy and so their discovery did not correspond to the particle imagined by Pauli. They did, however, change the picture of the atom and helped accelerate discoveries in particle physics. The neutron was ideal for bombarding other nuclei and, consequently, looking at the decay of a neutron in beta decay led to the discovery of the neutrino. At the end of 1933, Enrico Fermi introduced a comprehensive theory of radioactive decays [3], incorporating Pauli's theoretical particle, and thus went on to christen this particle the neutrino, distinguishing it from the neutron. This translates as 'little neutral one'. The name was conveniently chosen to match the zero mass and zero charge hypothesized for the neutrino. These attributes explain why, at the time of the postulation of its existence, it was undetected. So the question arose, 'How was the physics world going to prove the existence of the neutrino if it appeared to be undetectable?'

Another important discovery that went a long way to convince Pauli and Fermi of the neutrino's existence was that of the positron. In 1936 Carl Anderson found the first anti-particle [4], the anti-electron, more commonly known as the positron because of its positive charge. This only went further to support the conjecture that it was an anti-neutrino that was missing in the beta decay of a neutron. With the notion of anti-matter firmly established in particle physics theories, the obvious step now was to find this elusive (anti-) neutrino. Through the extensive research by Irene and Frederic Juliot-Curie into artificial radioactivity, followed by the first atom bomb explosion in 1945, the discovery of the neutrino seemed a great possibility. An atom bomb is a great source of neutrinos. Fred Reines realized this and, with the help of fellow physicist Clyde Cowan Jr., he used a more acceptable nuclear source of neutrinos, a nuclear reactor.

Twenty-six years after Pauli's postulation, Reines and Cowan Jr. successfully devised an experiment to detect neutrinos that utilized beta decay of fission products in a nuclear reactor [5]. Reines and Cowan believed that nuclear reactors would produce very high neutrino fluxes, on the order of $10^{12} - 10^{13}$ neutrinos per cm^2. The experiment that is credited with finally discovering the neutrino was carried out near the nuclear plant of Savannah River, South Carolina in 1956. The experiment was located 11 m from the nuclear reactor's centre and shielded against cosmic ray background radiation because it was 12 m underground. The experiment consisted of two tanks filled with a total of 200 litres of water and 40 kg of cadmium chloride ($CdCl_2$) which acted as a target for the reactor neutrinos. More specifically, they were looking for the interaction of electron anti-neutrinos with protons that produce neutrons and positrons:

$$\overline{\nu}_e + p \rightarrow n + e^+$$

The positrons are annihilated along with a partner electron via pair-annihilation producing two 0.5 MeV photons in opposite directions. The photons produced scintillation light in liquid scintillator above and below the water tanks which was detected by photomultiplier tubes. The neutrons were observed via the following neutron capture interaction:

$$n + {}^{108}Cd \rightarrow {}^{109}Cd^{*} \rightarrow {}^{109}Cd + \gamma$$

When absorbing a neutron, ^{108}Cd produces an excited state of ^{109}Cd which subsequently emits a photon. The photons from the neutron capture were also detected in the scintillator microseconds after the two photons from the pair-annihilation. In this way, Reines and Cowan Jr. confirmed the neutrino-induced events and therefore discovered the neutrino. Fred Reines went on to call the neutrino "... the most tiny quantity of reality ever imagined by a human being."; a fitting description to what has become an integral part of the Standard Model.

2.2 The Standard Model of Particle Physics

In order to introduce the theory of neutrino oscillations it is important to address the the current 'standard' theory of particle physics, namely the Standard Model (SM). There are two types of fundamental particles within the SM, fermions and bosons. Fermions account for observed matter and consist of quarks and leptons which all have half-integer spin and obey Fermi-Dirac statistics. Bosons, on the other hand, obey Bose-Einstein statistics, have integer spin and are the force carrier particles for the strong and electroweak forces.

For later understanding it is important to briefly explain that the spin of a particle can be used to define the particle's handedness: "left-handed" (LH) and "right-handed" (RH) states exist. To understand handedness requires introducing helicity. The particle's helicity is the projection of its spin vector onto its momentum vector. The relation that helicity has to handedness

is such that helicity can be written as a linear combination of the particle's handedness. For massless particles, including neutrinos, handedness is identical to helicity. The helicity of a particle is right-handed if the direction of its spin is the same as the direction of its momentum and left-handed if the directions of spin and momentum are opposite, shown graphically in Figure 2.1. Massive particles have both LH and RH components because the observed helicity is dependent on the frame of reference of the observer. An observer in a frame of reference which is moving faster than the particle would see the momentum of the particle as changing sign whereas, an observer in the particle's rest frame would not see this. In both cases, the sign of the spin remains the same; hence, for the observer in the first frame of reference the particle's helicity flips. It is impossible to move to a frame of reference where helicity changes sign for massless particles travelling at the speed of light. In the Standard Model neutrinos are left-handed and anti-neutrinos are right-handed when considering a massless (anti-)neutrino. The existence of non-zero neutrino masses complicates this situation as this would suggest that there is a right-handed neutrino and left-handed anti-neutrino couterpart though neither has been observed. If they do exist their properties are substantially different from the observed left-handed neutrino and right-handed anti-neutrino. A number of theories exist Beyond the Standard Model (BSM) that suggest that they are either heavy on the order of the Grand Unified Theory scale through the Seesaw Mechanism, do not participate in weak interactions and are thus called 'sterile neutrinos', or both [6]. The extension of this discussion is beyond the scope of this thesis.

Figure 2.2 shows a table of the known particles of the SM, listing the corresponding mass, charge and spin of each particle. The SM contains 12 flavours, or types, of fermions which make up the matter of the universe. There is also a corresponding anti-particle for each of the 12 fermions, identical in all aspects except that the electric charges are of opposite sign, or in the case of neutral particles, the quantum numbers are of opposite value. The fermions are divided into three generations (or families) of four particles so that there are two quarks and

Fig. 2.1. A particle's helicity is the sign of the projection of its spin vector, S, onto the momentum vector, p. The helicity of a particle is right-handed if the direction of its spin is the same as the direction of its momentum and left-handed if the directions of spin and momentum are opposite. Helicity and handedness are the same for massless particles.

two leptons in each generation. For example, the first generation consists of the up and down quarks, the electron neutrino and the the electron. The two quarks within each generation are one up-type with charge $+\frac{2}{3}$ and one down-type with charge $-\frac{1}{3}$. The quarks combine to form either mesons composed of one quark and one anti-quark, or baryons composed of three quarks such as the protons and neutrons [7].

The two leptons within each generation are classified as charged leptons (the electron, muon or tau) and neutral leptons(electron-, muon- and tau-neutrinos). Generations differ by mass only, with mass increasing as you go up through the generations.

The four bosons shown in Figure 2.2 mediate the strong, electromagnetic and weak forces. The strong force is mediated by eight gluons, which interact with colour-charged particles. Gluons themselves are colour-charged with a mixture of two colours, as are quarks which carry only one of three colour charges.

The electromagnetic force is mediated by the massless, chargeless photon which interacts with electrically charged particles. The range of the forces is related to the mass (M) of the exchanged boson by the Yukawa potential [8]

$$V_{Yukawa}(r) = -g^2 \frac{exp(-Mr)}{r} , \tag{2.1}$$

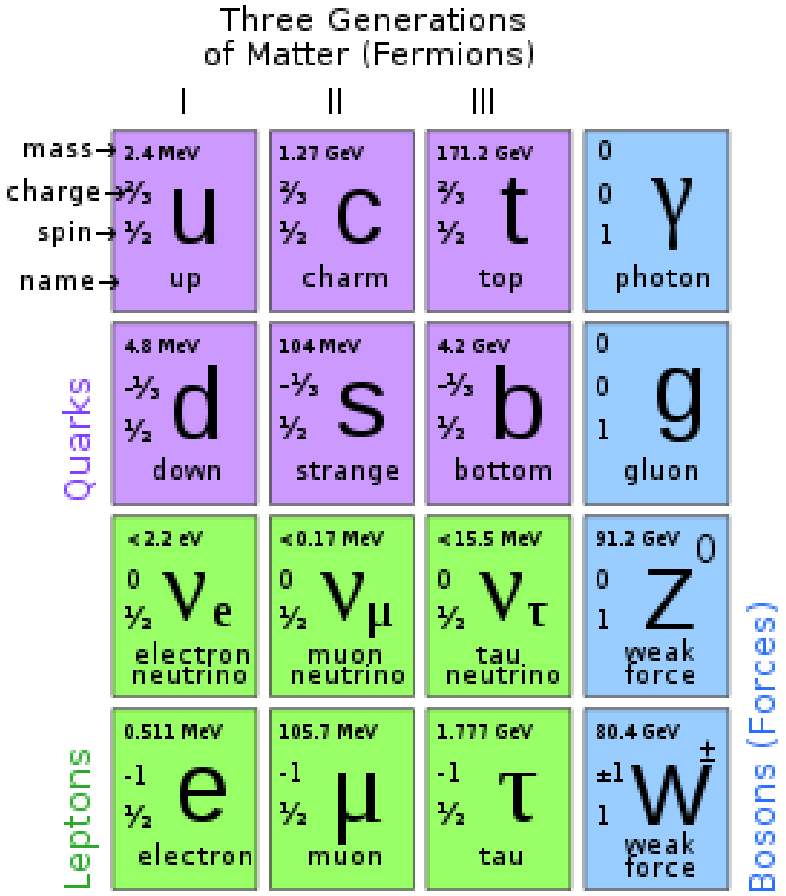

Fig. 2.2. Fundamental particles of the Standard Model [7]. The constituents of matter are fermions (first 3 columns) made up of quarks (upper half) and leptons (lower half). The bosons (fourth column) are the force carriers. The table shows the mass, charge and spin of each particle. Each of the 12 fermions has a corresponding anti-particle that has identical mass and spin but has opposite quantum number labels. These labels are electric charge, colour charge, flavour, electron number, muon number, tau number, and baryon number.

where g is the coupling strength for the boson and r is the radial distance to the boson. Equation 2.1 reduces to the Coulomb potential for $M \rightarrow 0$, hence the massless nature of the photon explains the infinite range of the electromagnetic force.

The weak force is carried by the massive $W^{\pm}$ and Z^0 bosons and due to their large masses the force is suppressed at low energy such that its field strength is 10^{-3} times that of the electromagnetic force and 10^{-6} of the strong force. The weak interactions only take place between LH fermions and RH anti-fermions and, other than gravity (which is negligibly small at the length

and mass differences pertinent to particle physics), is the only force that acts on neutrinos. Experiments of Wu *et.al* [9], Garwin *et.al* [10] and Goldhaber *et.al* [11] showed that the weak interaction maximally violates parity and that the massless SM neutrino must be LH. The number of neutrino species, N_ν, derives from the measurement of the Z^0 boson decays into neutrinos which form the invisible Z^0 width, Γ_{inv}. In the Standard Model $N_\nu = \Gamma_{inv}\Gamma_\nu$ where Γ_ν is the decay width of the Z^0 into each neutrino family. The total Z^0 width (Γ_{tot}) is a combination of its partial width into hadrons (Γ_{had}) and leptons (Γ_{lept})

$$\Gamma_{tot} = \Gamma_{had} + 3\Gamma_{lep} + N_\nu\Gamma_{inv}$$

Using the above the number of neutrino species can be deduced. Measurements of the width of the Z^0 boson at CERN and SLC (Stanford Linear Collider) demonstrated that there are three neutrinos that couple to the Z^0, in fact measuring that the number of neutrino species is 2.984 ± 0.008, which strongly supports that there are only 3 generations of leptons in the SM [12, 13].

The energy and momentum of the neutrino is deduced from the particles resulting from a neutrino interaction. The cross-section, σ, for neutrino-induced interactions is proportional to the neutrino energy E ($\sigma \simeq 10^{-41}$E cm^2, E expressed in MeV) so a large flux of accelerator-produced neutrinos can be indirectly detected through their interactions, even though the interaction probability in a one kiloton target/detector is only of the order of 1 in a billion for energies in the 100 GeV range [14].

There are two types of neutrino interactions, charged current (CC) and neutral current (NC) interactions, since the weak force is carried by the charged W and neutral Z bosons.

2.2.1 Charged Current Interactions

Weak interactions involving a $W^{\pm}$ boson are called CC interactions. In one type of CC interaction the W boson couples to a charged lepton and a neutrino or anti-neutrino. The neutrino is always the same flavour as the charged lepton, implying lepton flavour is conserved in weak interactions. As a result, the flavour of the neutrino in a CC interaction can be identified by the flavour of the charged lepton observed in the interaction. The main process at the T2K peak neutrino energy of around 700 MeV is a charged-current quasi-elastic (CCQE) event. Figure 2.3 shows a CCQE interaction, where l is the charged lepton, either e or μ. In terms of T2K, an incoming ν_μ interacts with the neutron in the nucleus of detector target material via the weak interaction, mediated by the W boson. This interaction results in a final state outgoing muon and a recoil proton. There is insufficient energy to produce a τ particle at T2K energies. The CCQE events are the easiest for reconstructing the neutrino energy since this is a two-body process and the initial neutrino energy can be calculated from the outgoing lepton momentum and direction, ignoring the binding energy and Fermi motion within the nucleus. This makes CCQE events ideal for measuring the T2K neutrino energy spectrum and flux.

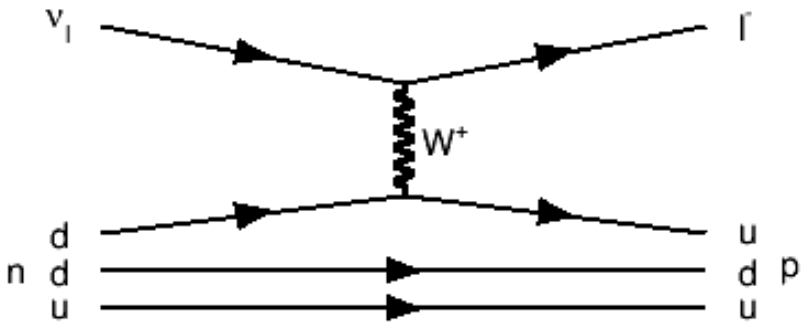

Fig. 2.3. Feynman diagram of a CCQE interaction, where l = e or μ. This is the dominant channel in T2K and the one in which it is easiest to reconstruct the neutrino energy. Left shows the initial state, right shows the final state.

This process is dominant for neutrinos up to 1.1 GeV. CC non-QE interactions (CCnQE) add to the background of measurements since it is much harder to determine the energy of the neutrino using the final state energy due to the final states being mis-identified or due to lost energy. Some typical CCnQE interactions are CC events with one pion (CC1π), multiple pions (CC-multiπ) or resonant pion production where the W boson transfers enough energy to convert the nucleon into an excited resonant baryon state. Above 10 GeV, CCnQE interactions are dominated by deep inelastic scattering (DIS); the neutrino interacts directly with the quark structure of a nucleon, instead of the nucleon as a whole. DIS will be rare in T2K due to the large neutrino energy required. This is clear from Figure 2.4 which shows the fractional cross-sections of the CC interactions and their dependence on energy for the energy range of the T2K ν_μ neutrino beam. The dominance of CCQE interactions at the peak T2K neutrino energy region of ~ 0.7 GeV is also apparent, up to 1.1 GeV where single pion CCnQE interactions are peaked.

2.2.2 Neutral Current Interactions

Interactions mediated by the Z^0 boson are called neutral current (NC) interactions because there is no flow of electric charge. Only momentum and energy are transferred in the interaction. For low energy neutrino-nucleon interactions, the target nucleon remains unchanged, and may or may not leave the target nucleus. At higher energy, sufficient energy may be passed to create other particles, generally pions. The largest NC background interaction is the neutral current single π^0 (NC-π^0) interaction. In this interaction, only a single new particle is produced, a π^0 meson. The π^0 decays with a mean life time of $(8.4 \pm 0.6) \times 10^{-17}$ s, and 99% of the time it decays to two photons [7]. Figure 2.5 is a Feynman diagram of a NC-π^0 interaction which occurs when a baryon resonance is excited and the baryon subsequently decays back to its ground state nucleon, emitting one (or more) mesons in the process, such as the π^0. This is called “resonant”

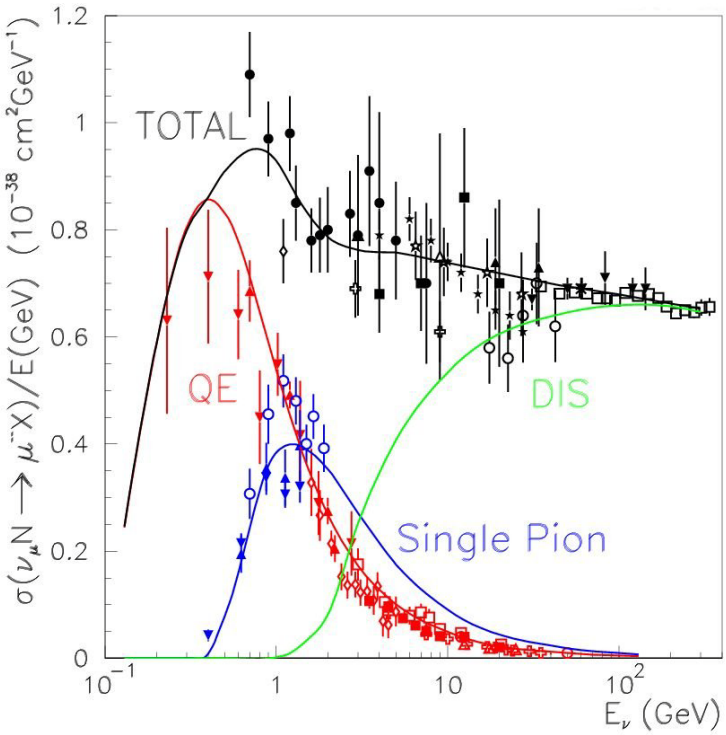

Fig. 2.4. The fractional cross-sections of charged-current interactions as a function of neutrino energy for QE, 1-π and DIS events [15]. T2K neutrino energy peaks at 0.7 GeV.

π^0 production and is the most dominant process for single π^0 production. There are also "coherent" NC-π^0 processes in which the neutrino interacts with a nucleus as a whole rather than the individual nucleons. The process is referred to as "coherent" because the nucleus recoils as a whole without breaking up. The NC-π^0 cross-section is not well known in the T2K energy region.

2.3 The Solar and Atmospheric Neutrino Problems

Experiments through the years proved that neutrinos oscillate between flavours as they travel and so after a time t and distance L an electron neutrino can become a muon or tau neutrino. The first evidence for this was found when the measured intensity of electron neutrinos produced during nuclear fusion and originating from the core of the Sun was found to be less than what was expected theoretically. This was called the solar neutrino problem (SNP). The

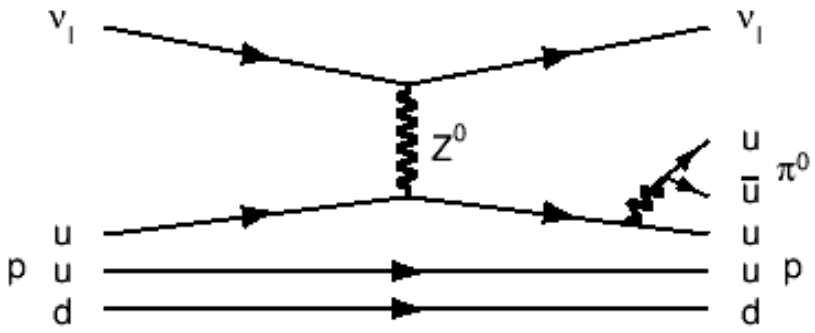

Fig. 2.5. Feynman diagram of a NC-π^0 interaction detected by T2K. This is a "resonant" π^0 production process as it occurs when a baryon resonance is excited and subsequently decays back to its ground state nucleon, emitting the π^0 in the process. Initial state is on the left, final state is on the right.

SNP was discovered by Ray Davis *et.al* in measurements made by the Homestake radiochemical experiment [16] which detected solar neutrinos through the inverse beta decay Cl-Ar reaction:

$$\overline{\nu}_e + {}^{37}Cl(n) \rightarrow {}^{37}Ar(p) + e^-$$

Theorist John Bahcall *et.al* had predicted a solar neutrino flux rate between 6.6 and 8.1 Solar Neutrino Units (1 SNU = one interaction per 10^{36} target atoms per second) [17].

In 1968, the first data of the Homestake experiment indicated that the solar neutrino flux was 2.56 ± 0.16(stat) ± 0.16(syst.) SNU [18], about $\frac{1}{3}$ of the flux predicted by Bahcall in the Standard Solar Model (SSM). In subsequent years, a series of experiments provided independent confirmation of the Homestake measurement. The first confirmation of the SNP came from the Kamioka Nucleon Decay Experiment II (Kamiokande II) [19]. This experiment detected solar neutrinos via Cherenkov light emitted by the electrons produced in neutrino interactions in a 0.68 kT fiducial volume of water [20]. From [6] and [21], the average neutrino flux measured in the Kamiokande experiment from January 1987 to February 1995 (2079 days) was 2.80 ±

0.19 (stat) ± 0.33 (syst.) x 10^6 $cm^{-2}s^{-1}$, consistent in SNUs with the Homestake measurement. Several other experiments, including GALLEX [22], SAGE [23], GNO [24] and Borexino [25], have provided further independent confirmation of the SNP.

Even though these experiments had found evidence of neutrino disappearance, this alone does not constitute evidence of neutrino flavour change or neutrino oscillations. The evidence of neutrino oscillations was first reported by the Super-Kamiokande (Super-K) experiment in 1998 [26]. Super-K, an upgrade of Kamiokande, measured a zenith angle dependent deficit of atmospheric muon neutrinos; that is, the experiment observed that the flux of upward-moving muon neutrinos was smaller than the flux of downward-moving muon neutrinos. The SNO (Sudbury Neutrino Observatory) experiment directly demonstrated neutrino flavour-changing in solar neutrinos in 2001 [27]. SNO used the deuterium in heavy water as a target for solar neutrinos. This allowed for a direct measurement of both the electron neutrino flux via the CC interaction $\nu_e + d \rightarrow p + p + e^-$, and the flux of all active neutrino flavours (ν_l) via the NC interactions $\nu_l + d \rightarrow p + n + \nu_l$. The result is that SNO was then able to make a comparison of the measured electron neutrino flux against the flux measurement of the electron, muon and tau neutrinos. The NC flux measurement agreed with Bahcall's SSM prediction which lead to the firm belief that flavour change between neutrinos explained the solar neutrino problem.

Atmospheric neutrinos are produced in the upper layers of the Earth's atmosphere as a result of cosmic ray interactions. Theoretically there should be twice as many ν_μ as ν_e observed; however, this ratio has not been observed experimentally. The IMB (Irvine-Michigan-Brookhaven) experiment [28] and the Kamiokande and Super-K experiments, all built primarily with the goal of observing proton decay, reported a deficit in the number of muon neutrinos created in the atmosphere with respect to the number of electron neutrinos. The deficit became known as the atmospheric neutrino anomaly and provided further evidence for neutrino oscillations.

The K2K (KEK-to-Kamioka) experiment [29] (of which T2K can be regarded as the successor) collected accelerator-produced neutrino data from 1999 to 2004. K2K produced a ν_μ beam at KEK, Japan with a mean energy of 1.3 GeV and directed it towards Super-K 250 km away. The experiment demonstrated the disappearance of muon neutrinos to the extent that the probability of observing the experimental results if there was no neutrino oscillation was 0.0050 % corresponding to 4.0 σ [30]. The K2K data are consistent with the oscillation effects previously reported by Super-K, using data from atmospheric neutrinos.

2.4 Neutrino Oscillations in Vacuum

In 1975-1976 S. Eliezer and A.R. Swift [31], H. Fritzsch and P. Minkowski [32], and S.M. Bilenky and B. Pontecorvo [33, 34] developed the idea of a plane-wave approximation for neutrino oscillations, such that the three flavour neutrinos ν_e , ν_μ , ν_τ (weak eigenstates) are unitary linear combinations of three massive neutrinos ν_1 , ν_2 , ν_3 (mass eigenstates) and thus the theory of neutrino oscillations was born. As the neutrinos travel they can be described as a quantum mechanical state in which they exist as all flavours of neutrinos at once. This admixture of flavour states can be represented mathematically as a wave.

2.4.1 Two Flavour Mixing

Following the formalism by R.D. Peccei [35], who initially considered vacuum oscillations of neutrinos of just two flavours, ν_e and ν_μ, we describe briefly the derivation for the two-flavour case which can be generalised to three flavours. Here we treat the two-flavour neutrinos as unitary linear combinations of two mass eigenstates ν_1 and ν_2:

$$\begin{pmatrix} \nu_\mu & \nu_e \end{pmatrix} = \begin{pmatrix} \cos\theta & \sin\theta \\ -\sin\theta & \cos\theta \end{pmatrix} \begin{pmatrix} \nu_1 & \nu_2 \end{pmatrix}, \tag{2.2}$$

where θ is the mixing angle between the two sets of neutrino states. The wave functions are orthonormal states of the weak and mass eigenstates of the two neutrinos as prescribed below using the Dirac 'Bra-Ket' notation:

$$|\nu_\mu\rangle = \cos\theta|\nu_1\rangle + \sin\theta|\nu_2\rangle \tag{2.3}$$

$$|\nu_e\rangle = -\sin\theta|\nu_1\rangle + \cos\theta|\nu_2\rangle \tag{2.4}$$

Setting $\hbar = c = 1$, the mass eigenstates propagate in space with a time evolution following from the Schrodinger equation:

$$|\nu_1(t)\rangle = e^{-iE_1t}|\nu_1(0)\rangle \tag{2.5}$$

$$|\nu_2(t)\rangle = e^{-iE_2t}|\nu_2(0)\rangle \tag{2.6}$$

$$\text{where } E_i = \sqrt{|\vec{p}^2| + m_i^2} \tag{2.7}$$

The weak interaction eigenstate ν_e produced at t = 0 evolves in time into a superposition of ν_e and ν_μ states since $m_1 \neq m_2$. By definition $|\nu_i\rangle \equiv |\nu_i(0)\rangle$ so it can be shown by substituting Equation 2.5 for $|\nu_e\rangle$ that:

$$|\nu_e(t)\rangle = \cos\theta e^{-iE_1t}|\nu_1\rangle + \sin\theta e^{-iE_2t}|\nu_2\rangle \tag{2.8}$$

$$= \left(\cos^2\theta e^{-iE_1t} + \sin^2\theta e^{-iE_2t}\right)|\nu_e\rangle + \left(\cos\theta\sin\theta\left(e^{-iE_2t} - e^{-iE_1t}\right)\right)|\nu_\mu\rangle \tag{2.9}$$

$$\equiv A_{ee}(t)|\nu_e\rangle + A_{e\mu}(t)|\nu_\mu\rangle \tag{2.10}$$

, where $A_{ee}(t) = \langle \nu_e | \nu_e(t) \rangle$, is the quantum mechanical transition amplitude that describes this transition. Likewise, $A_{e\mu}(t) = \langle \nu_\mu | \nu_e(t) \rangle$ describes the transition of a ν_e state into a ν_μ state. To calculate the probability that at a time t the pure ν_e state is either a ν_e ("*survival probability*") or a ν_μ weak eigenstate ("*oscillation probability*") requires using the fact that the probability is the square of the transition amplitude.

Let us calculate the probability for a pure ν_e state to oscillate into a ν_μ state after time t:

$$P(\nu_e \to \nu_\mu; t) = |\langle \nu_\mu | \nu_e(t) \rangle|^2 \equiv A_{e\mu}(t)^* A_{e\mu}(t) \tag{2.11}$$

$$= 2\cos^2\theta \sin^2\theta + \cos^2\theta \sin^2\theta \left(e^{i(E_2 - E_1)t} - e^{-i(E_2 - E_1)t} \right) \tag{2.12}$$

$$= 2\cos^2\theta \sin^2\theta - 2\cos^2\theta \sin^2\theta \left[\cos\left(E_2 - E_1\right) t \right] \tag{2.13}$$

Equation 2.11 makes use of Fourier transfrom and the Kronecker delta, $\delta_{ij} \equiv \langle \nu_i | \nu_j \rangle$. Euler's formula reduces the argument of the second $\cos^2\theta \sin^2\theta$ in Equation 2.12. Using the trigonometric relation $\cos 2\theta = \cos^2\theta - \sin^2\theta$, the above equation becomes

$$P(\nu_e \to \nu_\mu; t) = \frac{1}{2} \sin^2 2\theta \left[1 - \cos\left(E_2 - E_1\right) t \right]. \tag{2.14}$$

Since the neutrino is ultra-relativistic, we can make the substitution $t \simeq L$, where L is the distance travelled by the neutrino in time t. We can also apply Taylor's expansion to Equation 2.7 and keep the first term of the expansion since the neutrino mass is small compared to its momentum. Applying the substitutions and using the trigonometric relation $(1 - \cos 2\theta)/2 = \sin^2\theta$, Equation

2.14 becomes

$$P(\nu_e \rightarrow \nu_\mu) = \sin^2 2\theta \sin^2\left(\frac{\Delta m^2 L}{4p}\right) \tag{2.15}$$

$$= \sin^2 2\theta \sin^2\left(\frac{\Delta m^2 L}{4E_\nu}\right), \tag{2.16}$$

where $p \simeq E_\nu$ and $\Delta m^2 = m_2^2 - m_1^2$. Finally we can make the argument dimensionless by introducing the appropriate number of $\hbar$'s and c's and expressing quantities with convenient units, specifically L in metres, $\Delta m^2 c^4$ in $(\mathrm{eV})^2$ and E in MeV. We can then write:

$$\left(\frac{\Delta m^2 c^4}{4\hbar c}\frac{L}{E_\nu}\right) \Rightarrow \left(\frac{\Delta m^2 c^4}{4 \text{ x } 197\mathrm{eV}\cdot\mathrm{nm}}\frac{L}{E_\nu}\right)\left(\frac{10^{-6}\mathrm{MeV/eV}}{10^{-9}\mathrm{m/nm}}\right) = \left(1.27\Delta m^2 \frac{L}{E_\nu}\right). \tag{2.17}$$

The probabilities for a pure ν_e state to oscillate into a ν_μ state or to remain as a ν_e state are respectively

$$P(\nu_e \rightarrow \nu_\mu) = \sin^2 2\theta \sin^2\left(\frac{1.27\Delta m^2 L}{E}\right) \tag{2.18}$$

$$P(\nu_e \rightarrow \nu_e) = 1 - \sin^2 2\theta \sin^2\left(\frac{1.27\Delta m^2 L}{E}\right) \tag{2.19}$$

$$\text{since } P(\nu_e \rightarrow \nu_e) \equiv 1 - P(\nu_e \rightarrow \nu_\mu). \tag{2.20}$$

The same formalism can be followed to calculate the probability for a ν_μ to oscillate into a ν_e state, since this is most relevant to the T2K experiment which produces a pure ν_μ beam and searches for ν_e appearance 295 km away. This probability for oscillation and opposing survival probability of the ν_μ state is

$$P(\nu_\mu \rightarrow \nu_e) = \sin^2 2\theta \sin^2\left(\frac{1.27\Delta m^2 L}{E}\right) \tag{2.21}$$

$$P(\nu_\mu \rightarrow \nu_\mu) = 1 - \sin^2 2\theta \sin^2\left(\frac{1.27\Delta m^2 L}{E}\right) \tag{2.22}$$

.

In the three-flavour mixing, the neutrino flavour eigenstates are written as linear combinations of the mass eigenstates using a 3 x 3 unitary mixing matrix U_{kj}:

$$\begin{pmatrix} \nu_\mu & \nu_e & \nu_\tau \end{pmatrix} = \begin{pmatrix} U_{e1} & U_{e2} & U_{e3} \\ U_{\mu 1} & U_{\mu 2} & U_{\mu 3} \\ U_{\tau 1} & U_{\tau 2} & U_{\tau 3} \end{pmatrix} \begin{pmatrix} \nu_1 & \nu_2 & \nu_3 \end{pmatrix}. \tag{2.23}$$

This matrix is referred to as the MNSP (Maki-Nakagawa-Sakata-Pontecorvo) mixing matrix [36] and can be written for three active neutrino flavours as the product of three rotation matrices, where one of them has a phase:

$$U = U_{23}(\theta_{23}) U_{13}(\theta_{13}, \delta) U_{12}(\theta_{12}). \tag{2.24}$$

Neutrino oscillations can be described by six parameters in the three-flavour picture: two independent mass-squared differences (δm^2_{12}, δm^2_{23} [1]), three mixing angles (θ_{12}, θ_{23}, θ_{13}) and a

[1] $\delta m^2_{kj} \equiv |m^2_k - m^2_j|$

CP-violating phase δ.

$$U_{kj} = \begin{pmatrix} 1 & 0 & 0 \\ 0 & c_{23} & s_{23} \\ 0 & -s_{23} & c_{23} \end{pmatrix} \begin{pmatrix} c_{13} & 0 & s_{13}e^{-i\delta} \\ 0 & 1 & 0 \\ -s_{13}e^{-i\delta} & 0 & c_{13} \end{pmatrix} \begin{pmatrix} c_{12} & s_{12} & 0 \\ -s_{12} & c_{12} & 0 \\ 0 & 0 & 1 \end{pmatrix}, \tag{2.25}$$

where $c_{kj} = \cos\theta_{kj}$ and $s_{kj} = \sin\theta_{kj}$, δ is the CP-violating phase.

For non-degenerate mass eigenstates and small θ_{13}, oscillations of solar neutrinos are dominated by the third sub-matrix and θ_{12}. The second sub-matrix is tested by reactor and accelerator measurements and involves the CP-violating phase δ and the first is dominated by atmospheric neutrinos. The 3 x 3 MNSP matrix is defined as follows:

$$U = \begin{pmatrix} c_{13}c_{12} & c_{13}s_{12} & s_{13}e^{-i\delta} \\ c_{23}s_{12} - s_{13}c_{12}s_{23}e^{i\delta} & c_{23}c_{12} - s_{13}s_{12}s_{23}e^{i\delta} & c_{13}s_{23} \\ s_{23}s_{12} - s_{13}c_{12}c23e^{i\delta} & -s_{23}c_{12} - s_{13}s_{12}c_{23}e^{i\delta} & c_{13}c_{23} \end{pmatrix} \begin{pmatrix} 1 \\ e^{i\alpha} \\ e^{i\beta} \end{pmatrix}, \tag{2.26}$$

where $c_{kj} = \cos\theta_{kj}$ and $s_{kj} = \sin\theta_{kj}$, δ is the Dirac phase and α, β are Majorana phases. These phases are non-zero if CP violation occurs.

The Dirac and Majorana phases are related to the nature of the neutrino. Charged fermions are referred to as Dirac particles as a consequence of charge conservation. Neutrinos do not carry charge as they are neutral particles so lepton number is the relevant quantum number used to distinguish neutrinos from their anti-particles. If neutrinos are observed to be Dirac particles then the Majorana phases vanish, leading to multiplication by a unit matrix on

the right-hand side of Equation 2.26. On the other hand, the total lepton number of the fermion can be broken and if this occurs it is possible for neutrinos to be identical to their own anti-particle. In the scenario that a fermion (not exclusively a neutrino) is its own anti-particle they are generally known as Majorana particles. Assuming neutrinos are Majorana particles then the observation of neutrinoless double β-decay (${}^{A}_{Z}\mathrm{X} \rightarrow {}^{A}_{Z+2}\mathrm{X}' + 2\mathrm{e}^{-}$) would be possible. Several experiments [37–41] are now looking for evidence of this process. The T2K experiment, as well as most of neutrino physics and other neutrino oscillation experiments, is however insensitive to addressing the Majorana or Dirac nature of the neutrino.

2.4.2 MSW Effect

As a beam of neutrinos traverses a medium, the neutrinos can interact with electrons in the medium. The neutrinos can also interact with the nucleons, but the cross-section is much smaller than with electrons. Interactions with matter can alter the neutrino oscillation probability. An electron neutrino interacts differently with electrons compared with the other two neutrinos. Specifically, electron neutrinos can interact by exchanging either a W or Z boson while the muon neutrino and tau neutrino can interact only by exchanging a Z boson. The interaction of all three neutrinos by exchanging the Z boson gives rise to a potential energy term in the Hamiltonian. This potential energy term is the same for all three neutrino flavours and thus can be absorbed into a global phase of the neutrino fields. However, the potential energy term of an electron neutrino, because of exchanging the W boson, cannot be absorbed and hence has physical consequences. This is called the Mikheyev-Smirnov-Wolfenstein (MSW) effect and it was used to explain the flavour conversion of solar neutrinos [36]. The MSW-mediated oscillation of solar neutrinos has provided the sign of the solar mass squared splitting from the ability to probe the exact flavour content of a specific mass eigenstate. T2K is not sensitive to this effect because the neutrinos do not travel far enough through dense matter, hence this effect will not be discussed further in this work.

2.5 Neutrino Experiments to Date

Many neutrino experiments have been built to study neutrino flavour change since the confirmation by the SNO collaboration that flavour change of neutrinos is the solution to the SNP. Neutrino oscillations have been discovered in atmospheric and solar neutrinos and consequently their discovery has been confirmed by experiments using neutrinos produced by accelerators and reactors.

Two mixing angles have been measured and they have been found to be much larger than the mixing angles in the quark sector. Atmospheric and accelerator neutrino oscillation experiments, T2K included, measure the mixing angle θ_{23} which parameterises the mixing of the second and the third lepton generation and the corresponding squared mass difference, Δm^2_{23}. Solar and reactor (with baseline around 100 km) neutrino oscillation experiments measure the mixing angle θ_{12} between the first and second generation.

The separate two-neutrino analyses in the atmospheric and solar regimes give two mass squared splittings, $| \Delta m^2_{atm} | \gg | m^2_{12} |$ as shown in Figure 2.7. The sign of the atmospheric mass squared difference has yet to be measured so within a three neutrino framework this leaves only two possible hierarchies of masses. By definition we associate the solar mass squared splitting to that between mass eigenstates 1 and 2, and the atmospheric splitting to that between eigenstates 2 and 3. We can then write the two possible hierarchies as $m_3 \gg m_2 > m_1$, which we call the normal hierarchy, and $m_2 > m_1 \gg m_3$ which we call the inverted hierarchy. The normal hierarchy is so named as it follows the same pattern seen in the other Standard Model particles of increasing mass differences with each generation. The inverted is named to infer that the lightest mass eigenstate consists primarily of the heavier charged lepton flavour eigenstates μ and τ.

A third neutrino oscillation regime has also been suggested in results from the Liquid Scintillator Neutrino Detector (LSND) experiment [42]. This regime, the LSND regime, does not fit within a three neutrino framework. The LSND experiment reported seeing a larger

$\Delta m^2_{LSND} \simeq 1$ eV^2 splitting, depending on the mixing angle, as a result of an excess of $\overline{\nu}_e$ events from a $\overline{\nu}_\mu$ beam. Several experiments in the same regime as LSND, notably KARMEN2 [43] and NOMAD [44], failed to confirm this result. The MiniBooNE experiment also saw no excess in the predicted region and thus excluded the LSND parameter space by searching for electron neutrino appearance [45]. The LSND result is neglected in neutrino oscillation analyses as standard practice.

Experiments in the atmospheric regime, such as Soudan-2 and Super-K, look at atmospheric neutrinos and are primarily sensitive to θ_{23}. For this reason, this mixing angle is often referred to as θ_{atm}. Long-baseline accelerator experiments such as K2K [2], MINOS [3], T2K [4] and NOνA [5] are sensitive to Δm^2_{23} ($\equiv \Delta m^2_{atm}$) because the distance travelled (L) and neutrino energies (E) are known and so the L/E dependence of the oscillation probability can be observed and the mixing angle measured. These experiments look for muon neutrino disappearance using a beam of ν_μ. The far detector in each case is placed some distance away from the beam source and the beam energy is tuned to maximise the oscillation signal at the far detector.

Figure 2.6 shows a summary of regions of mass-squared splitting and mixing angle favoured or excluded by various experiments as of 2010. The different line styles identify the different flavour states or the different experimental searches. The filled regions are used to distinguish between multiple confidence limits (CL) and for ease of tracking the experiment's prefered region for a particular oscillation state. For example, the large blue region that covers approximately half the length of the paramater space is the preferred region for ν_e disappearance at the 95% CL as measured by the GALLEX [22] and SAGE [23] experiments. The LSND prefered region for $\overline{\nu}_\mu$ to $\overline{\nu}_e$ appearance at the 90% and 99% is covered across the top half of Figure 2.6 by the turquoise and yellow regions respectively. One can see that the KARMEN2, NOMAD and MiniBooNE excluded regions cover this parameter space almost entirely. Also

[2] KEK-to-Kamioka
[3] Main Injector Neutrino Oscillation Search
[4] Tokai-to-Kamioka
[5] NuMI Off-Axis ν_e Appearance

shown are the constraints on the solar parameters due to the SNO and KamLAND (Kamioka Liquid scintillator Anti-Neutrino Detector) experiments. The KamLAND experiment was built to detect electron anti-neutrinos from nearby nuclear power reactors. It has a relatively short baseline with a mean distance of ~180 km from the reactors making it insensitive to matter effects. KamLAND was able to observe an oscillation in anti-neutrino deficit and also measure the anti-neutrino energy spectrum [46]. By accurately measuring the energy spectrum, KamLAND was able to make a precise measurement of the mass difference in the solar neutrino sector. Figure 2.6 shows that KamLAND makes the most precise measurement of the solar mass splitting term and can be combined with the SNO experiment and all other solar neutrino data to make the best solar neutrino oscillation parameter determination to date. Similarly, for the atmospheric oscillations the combination of the Super-K and MINOS results constrain the parameter space and produce the best atmospheric parameters. The precision with which the MINOS experiment has measured the ν_μ disappearance is highlighted by the small parameter space enclosed by the 90% CL dashed red line approximately in the centre of Figure 2.6.

The results from the latest MINOS data release [47] are

$$| \Delta m^2_{atm} | = (2.43 \pm 0.13) \times 10^{-3} \text{ eV}^2; \ \sin^2 2\theta_{atm} > 0.9 \text{ (90\% C.L.)}. \tag{2.27}$$

The MINOS measurement of the mixing angle θ_{atm} is consistent with that measured by all previous experiments as can be seen in Figure 2.6. This is most apparent when comparing to the Super-K measurements at the 90% CL as they overlap one another in the parameter space. The sign of the mass squared difference quoted in Equation 2.27 can only be obtained from neutrinos that have been affected by matter effects thus experiments that are sensitive to the MSW effect. Extra long baselines are in design for future neutrino, β-beam or neutrino factory experiments. NOνA [48] is a long-baseline neutrino oscillation experiment under construction

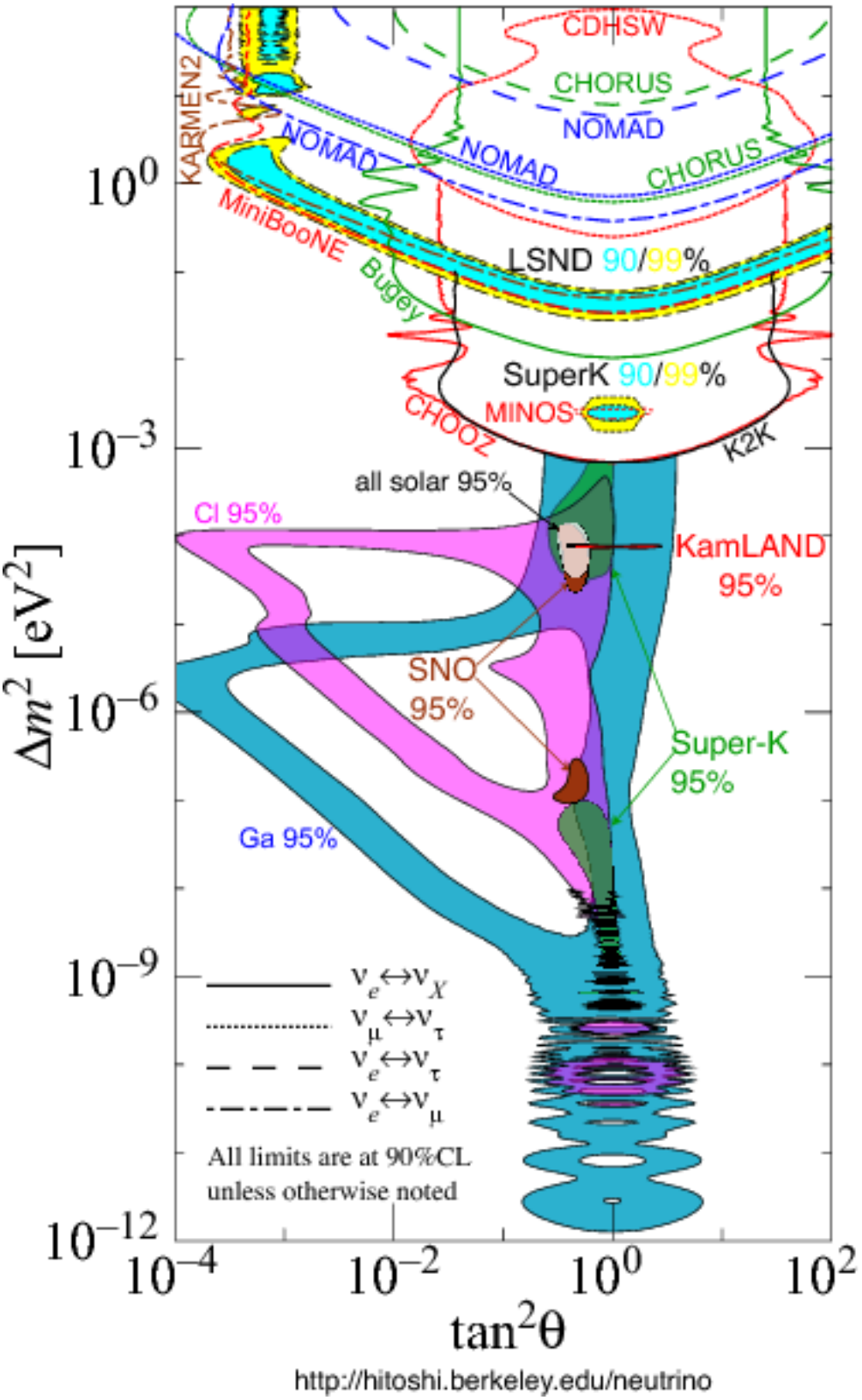

Fig. 2.6. Summary of neutrino oscillation experiment measurements up to 2010. The flavour states are identified by the line style as shown. All limits are at 90% confidence limit (C.L.) unless specified [7]

in the United States, utilising the existing NuMI beamline used by the MINOS experiment, but with a new set of near and far detectors. Its main goals are to measure θ_{13} and determine the mass hierarchy (sign of Δm^2_{atm}).

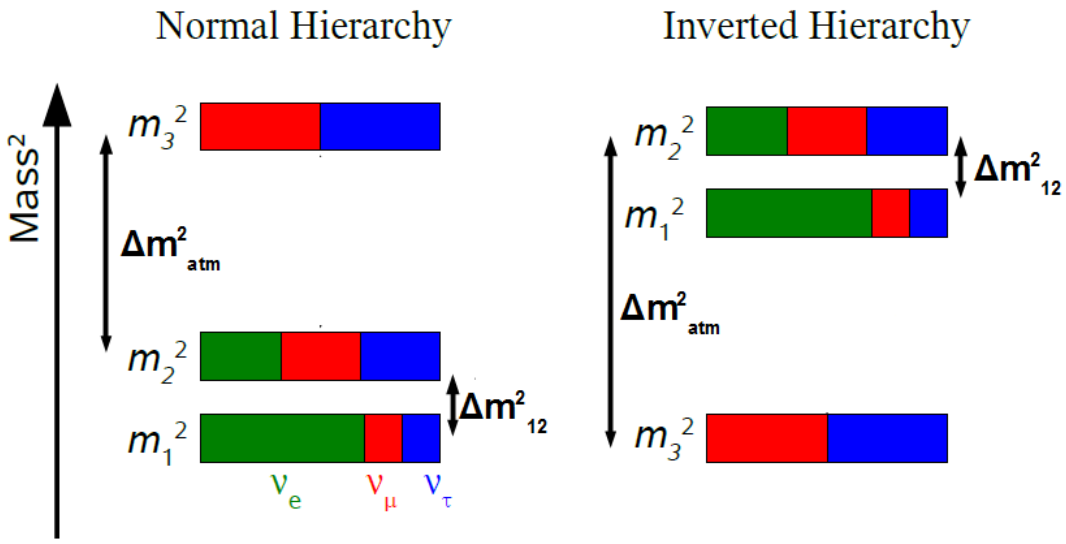

Fig. 2.7. Normal and inverted neutrino mass hierachies. The flavour content of each eigenstate is shown, approximately reflecting current data [49].

In order to measure θ_{13} one must work in the 3-flavour framework of neutrino oscillations. Table 2.1 summarises the three-flavour neutrino oscillation parameters extracted by [50] from analysing global data. A number of experiments contribute to the experimental limit on the value of θ_{13}, however the current limit is driven by the CHOOZ experiment [51]. The CHOOZ experiment measured the flux of $\overline{\nu}_e$ at a distance of 1 km from the Chooz reactor in France. Given the strong constraints on Δm^2_{13} arising from the other oscillation results we know that a suppression of this flux should have been seen if θ_{13} were large (like the two other angles). Therefore it is possible to constrain $\sin^2\theta_{13}$ to be less than ~6 x 10^{-2} at the 90% CL. T2K will be sensitive to values of the mixing angle $\sin^2 2\theta_{13}$ an order of magnitude below the CHOOZ limit. T2K will determine this by the measurement of a $\nu_\mu \rightarrow \nu_e$ signal. T2K will also be able

to make a more precise measurement of the atmospheric neutrino parameters, Δm^2_{atm} and the mixing angle $\sin^2 2\theta_{atm}$, than has been achieved to this date [49].

parameter	best fit	2σ	3σ
Δm^2_{21} [10^{-5} eV^2]	$7.59^{+0.23}_{-0.18}$	7.22 - 8.03	7.03 - 8.27
$\mid \Delta m^2_{31} \mid$ [10^{-3} eV^2]	$2.40^{+0.12}_{-0.11}$	2.18 - 2.64	2.07 - 2.75
$\sin^2 \theta_{12}$	$0.318^{+0.019}_{-0.016}$	0.29 - 0.36	0.27 - 0.38
$\sin^2 \theta_{23}$	$0.50^{+0.07}_{-0.06}$	0.39 - 0.63	0.36 - 0.67
$\sin^2 \theta_{13}$	$0.013^{+0.013}_{-0.009}$	$\leq$0.039	$\leq$0.053

Table 2.1. Best-fit values with 1σ errors and 2σ and 3σ intervals (1 d.o.f.) for the three-flavour neutrino oscillation parameters from global data including solar, atmospheric, reactor (KamLAND and CHOOZ) and accelerator (K2K and MINOS) experiments [50].

Chapter 3

The T2K Experiment

The T2K experiment is a second-generation long-baseline neutrino oscillation experiment designed to measure parameters of the MNSP matrix that governs the mechanism by which neutrinos oscillate. The experiment primarily intends to determine the mixing angle θ_{13} via the observation of ν_e appearance from a ν_μ beam. The T2K neutrino beam is generated using the 30 GeV proton synchrotron at the Japan Proton Accelerator Research Complex (J-PARC) on the east coast of Japan in Tokai, Ibaraki prefecture. The ν_μ beam is directed 295 km to the Kamioka mines under Mt. Denoyama in the Gifu prefecture, Japan, where Super-Kamiokande is situated and used as the far detector. The near detector suite is installed 280 m downstream from the beam source and consists of two detectors: the on-axis INGRID and off-axis ND280. The T2K beamline is described in Section 3.1, the near detectors are described in Section 3.2 and the far detector is described in Section 3.3.

The ν_μ to ν_e transition and ν_μ survival probabilities in vacuum can be approximately given by

$$P(\nu_\mu \rightarrow \nu_e) \approx \sin^2 2\theta_{13} \sin^2 \theta_{23} \sin^2 \left(\frac{\Delta m^2_{23} L}{4E_\nu} \right) \tag{3.1}$$

$$P(\nu_\mu \rightarrow \nu_\mu) \approx 1 - \sin^2 \theta_{23} \sin^2 \left(\frac{\Delta m^2_{23} L}{4E_\nu} \right) \tag{3.2}$$

by using the 3-flavour analogue of the 2-flavour oscillation probability described in Section 2.4.1, where L is the neutrino flight distance, and E_ν is the neutrino energy. It follows from this expression that the maximum sensitivity to the $\nu_\mu \rightarrow \nu_e$ transition is expected around the

oscillation maximum for $\Delta m^2_{13} \simeq \Delta m^2_{23} = \Delta m^2_{atm} \simeq 2.5$ x 10^{-3} eV^2. Based on this value, the ratio of L/E_ν was tuned so that the experiment maximizes its sensitivity to muon neutrino oscillations by producing a neutrino beam with an energy spectrum peaking in the range of the oscillation probability maximum. The parameters θ_{13}, θ_{23} and Δm^2_{23} can be derived from measurements of the probability as a function of L/E_ν. The length of the baseline was chosen as 295 km and the maximum of the oscillation probability will therefore be at a neutrino energy of 700 MeV/c as shown in the lower plot of Figure 3.1.

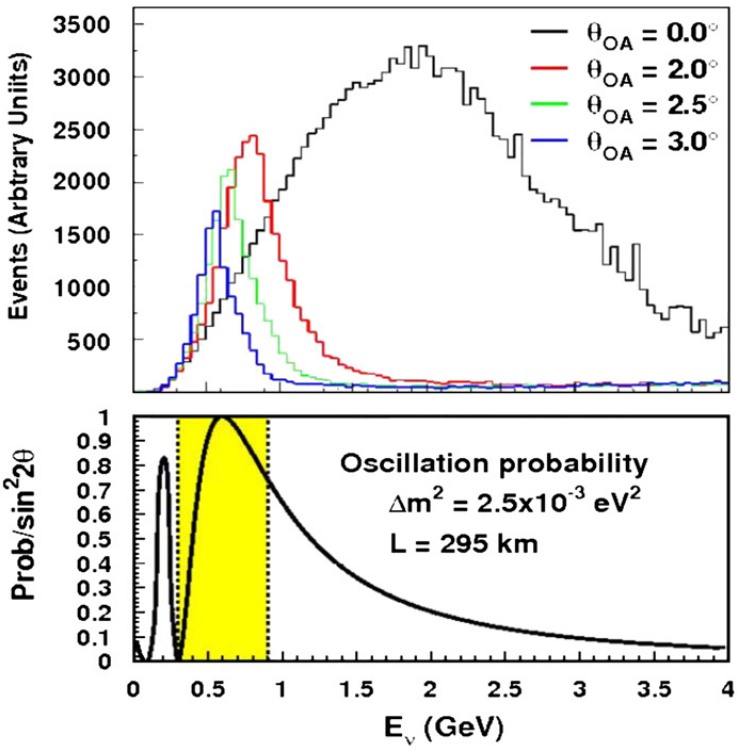

Fig. 3.1. Neutrino energy spectra at Super-K at different off-axis angles, 3.0°, 2.5°, 2.0°and on-axis shown as 0.0°off-axis (upper), with the oscillation probability as a function of neutrino energy below it (lower). The shaded region on the lower plot is the neutrino energy region of interest for T2K [49].

The neutrinos come from the interactions on a graphite target of the 30 GeV proton beam produced in a synchrotron accelerator in the JPARC facility, creating pions and kaons which are then focused by a series of electromagnetic horns in the forward direction. The mesons decay

in flight into ν_μ's and muons in a Decay Volume and charged particles are then stopped in the beam dump leaving the ν_μ beam with some beam contamination. The beam production process is described in more detail in Section 3.1.

T2K will adopt an off-axis beam configuration in which neutrino energy is almost independent of pion energy and a quasi-monochromatic neutrino spectrum can be achieved. The exploitation of the kinematics of the main pion decay channel provides a narrow neutrino spectrum with mean neutrino energies from 0.7 to 0.9 GeV, as shown in Figure 3.1 which illustrates that neutrino energy is not strongly dependent on pion energy at a fixed decay angle in the lab frame.

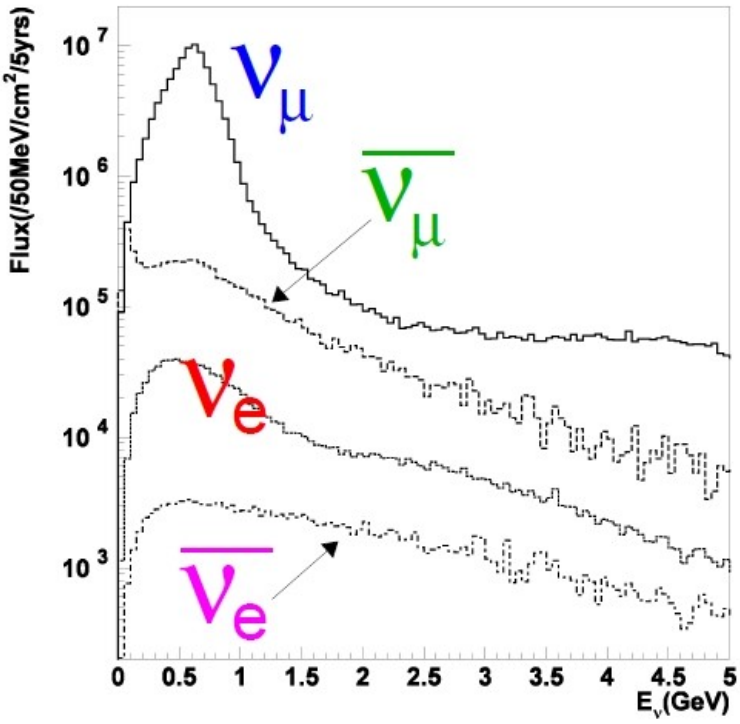

Fig. 3.2. The predicted neutrino fluxes at Super-K per 50 MeV/cm^2 in five years data as a function of neutrino energy. The flux of the ν_μ beam is shown with a predicted ν_e contamination of approximately 0.5%. The corresponding fluxes are shown for the neutrino beam in anti-neutrino mode [52].

The high energy tail is considerably reduced at 2.5° in comparison with the standard on-axis wide-band beam. This minimizes the neutral current π^0 background in the ν_e appearance search in Super-K. Moreover, the intrinsic contamination of ν_e's from muon and kaon decays is expected to be about 0.5% around the ν_μ peak energy at 2.5°, a factor of 5 lower than for the K2K on-axis beam. Figure 3.2 shows this 0.5% predicted ν_μ beam contamination of ν_e's at the ν_μ peak.

It is necessary to tune and monitor the ν_μ beam direction precisely to within 1 mrad because the peak of the ν_μ energy spectrum shifts according to the ν_μ beam direction ($\Delta\, E_{peak}$ = 2% per mrad). This is done by a series of beam monitors and the on-axis detector at the ND280 site described in Section 3.1.1.

The appearance of ν_e in a ν_μ beam is a sub-dominant process relative to the $\nu_\mu \rightarrow \nu_\tau$ mixing, due to the small value of θ_{13} relative to the other MNSP mixing angles. The T2K experiment will use a ν_e appearance measurement from a ν_μ beam in order to determine θ_{13} which involves determining $\sin^2\theta_{13}$ from the sub-dominant $\nu_\mu \rightarrow \nu_e$ appearance. T2K will also make a precision measurement of the mixing parameters $\sin^2\theta_{23}$ and Δm^2_{23} by measuring the dominant process $\nu_\mu \rightarrow \nu_x$ disappearance. This precision measurement is vital for the determination of θ_{13}. It has not yet been shown whether θ_{23} is maximal, and this is important in some models for the possibility of a minimal θ_{13}. Furthermore, if θ_{13} is non-zero this introduces the possibility of a measurable CP violating phase δ. Figure 3.3 shows T2K's sensitivity to θ_{13} at the 90% confidence level as a function of Δm^2_{23}. The sensitivity shown is for normal hierarchy. I do not shown the equivalent for inverted hierarchy as it is very similar due to the fact that T2K is insensitive to matter effects. The T2K sensitivity to θ_{13} will be a factor of 20 better than the current experimental limit. In the case of a non-zero θ_{13} T2K would search for δ by running in anti-neutrino mode and studyng the differences in the oscillation probability for neutrinos and anti-neutrinos. It should be noted however that T2K does not plan to produce a $\overline{\nu}_\mu$, at least in its first phase, thus T2K will not be able to determine the mass hierarchy and to discover CP violation.

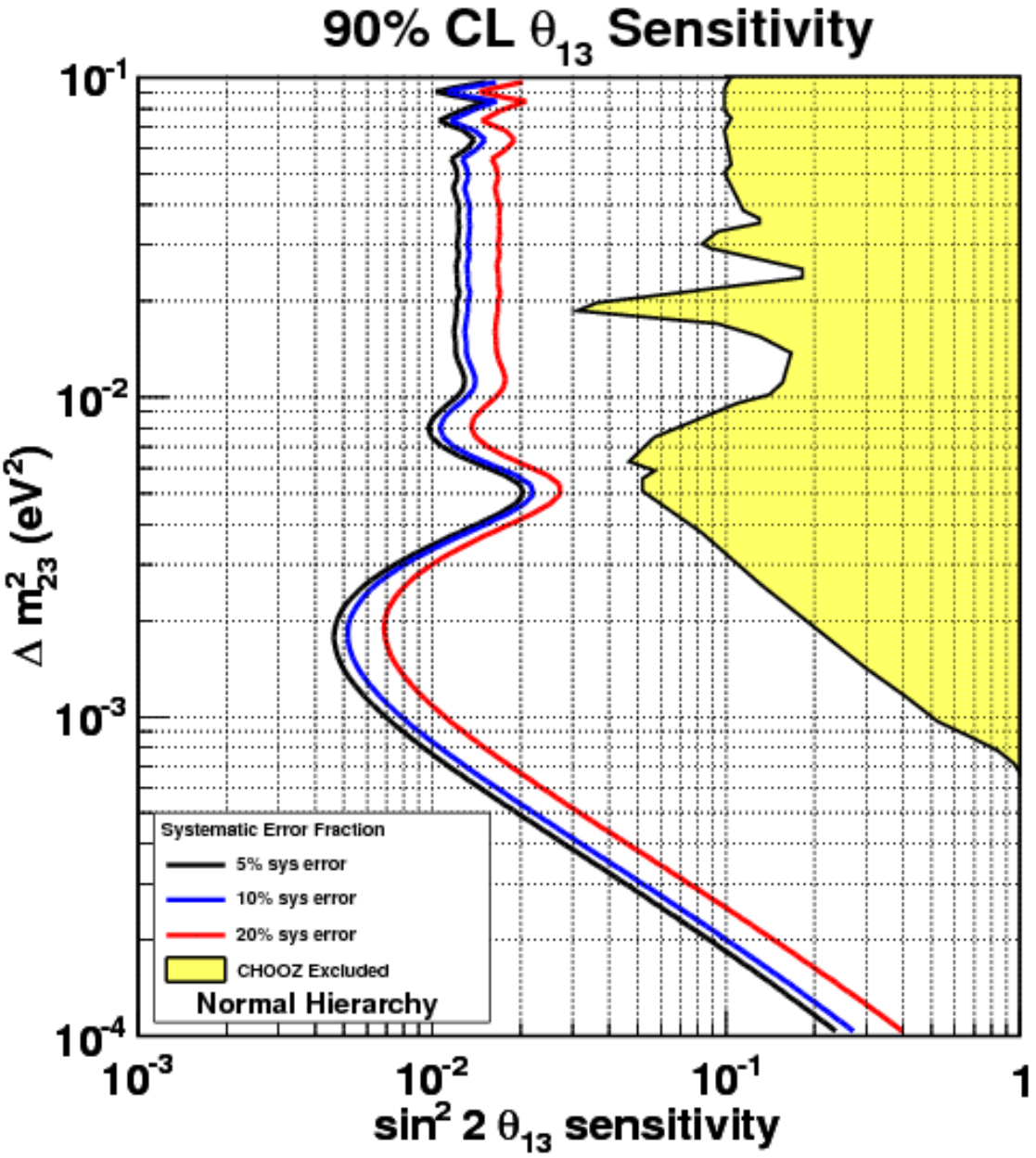

Fig. 3.3. T2K sensitivity to θ_{13} at the 90% confidence level as a function of Δm^2_{23}. Beam is assumed to be running at 750kW for 5 years, using the 22.5 kton fiducial volume Super-K detector. 5%, 10% and 20% systematic error fractions are plotted. The yellow region has already been excluded to 90% confidence level by the Chooz reactor experiment. The following oscillation parameters are assumed: $\sin^2\theta_{12} = 0.8704$, $\sin^2 2\theta_{23} = 1.0$, $\Delta m^2_{12} = 7.6 \times 10^{-5}\text{eV}^2$, $\delta_{CP} = 0$, normal hierarchy [49].

3.1 Beamline

J-PARC is a joint project between the High Energy Accelerator Research Organization in Japan, more commonly known as KEK, and the Japan Atomic Energy Agency (JAEA). The J-PARC accelerator facility is located at the Tokai campus, about 70 km north east of the Tsukuba campus of KEK which was the source of the beam neutrinos in the K2K experiment.

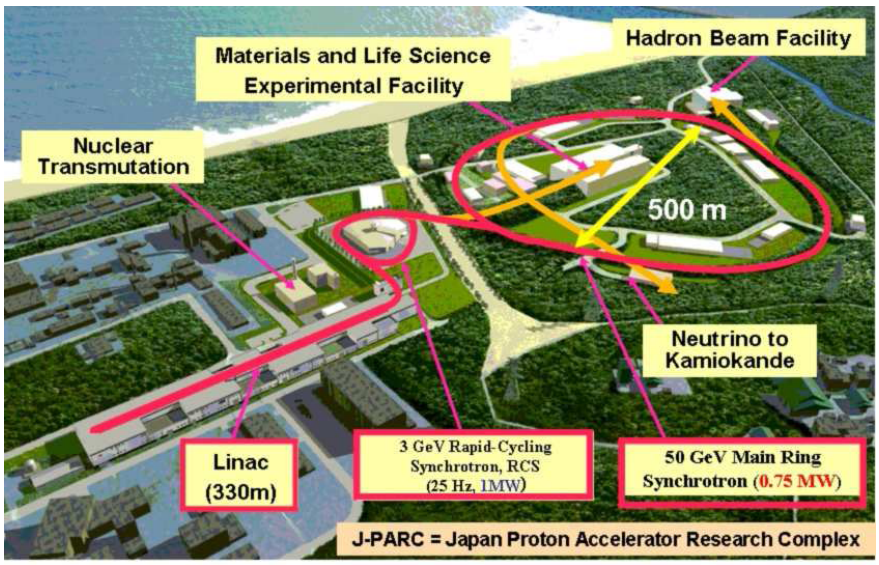

Fig. 3.4. Layout of the J-PARC facility. The J-PARC MR PS ring has been designed to produce a high intensity 50 GeV proton beam, but the experiment has started with an initial energy of 30 GeV. Proton acceleration begins in the LINAC, then progresses through the RCS and into the Main Ring [49].

The T2K neutrino beam is produced by accelerating, and subsequently colliding, protons from the J-PARC Main Ring (MR) Proton Synchrotron (PS) onto the T2K target. The MR PS is designed to accelerate protons up to 50 GeV but the initial proton energy is limited to 30 GeV in the first phase of the experiment. The salient feature of super-beam experiments such as T2K is a high intensity beam.

The protons are produced at J-PARC in a series of accelerators shown in Figure 3.4. The first of the accelerators is the Linear Accelerator (LINAC) which accelerates H^- ions to 400

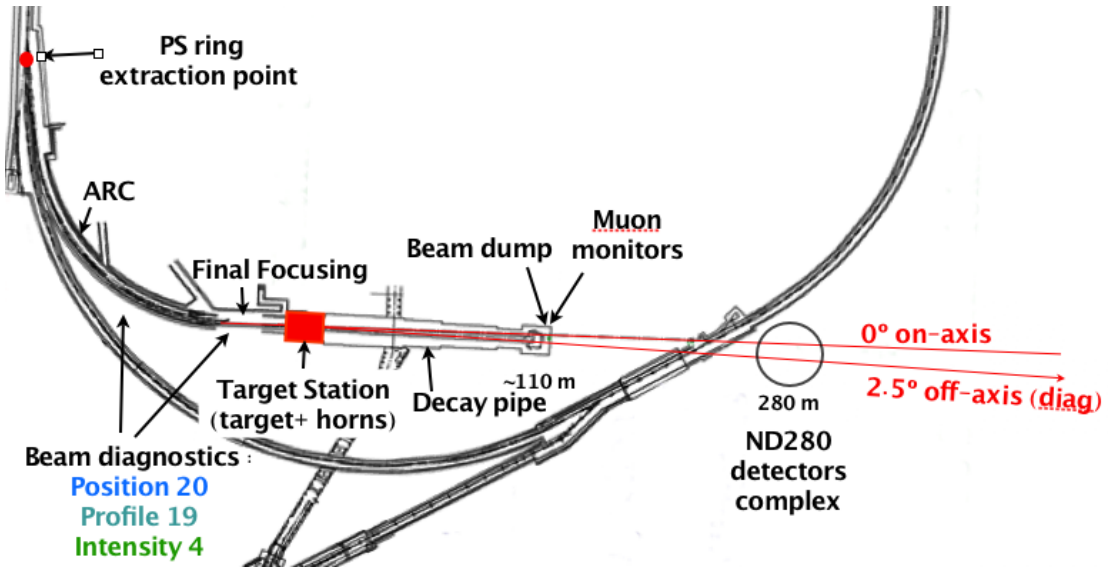

Fig. 3.5. Bird's-eye view of the T2K neutrino beamline at J-PARC [49].

MeV at 50 Hz. The electron content is then removed from the beam by the Carbon Stripper Foil and the remaining proton beam is injected into the 3 GeV Rapid-Cycling Synchrotron (RCS) and finally into the MR PS to produce the 30 GeV proton beam, which has a design intensity of 3.3 x 10^{14} protons per bunch with a repetition rate of 0.3 Hz and with 8 bunches per beam spill.

As shown in Figure 3.5, the proton beam is extracted from the MR PS into the primary proton beamline of the neutrino facility where it is focused and then directed onto T2K's neutrino production target. The T2K beamline consists of 28 combined function super-conducting magnets which produce both dipole (2.59 T/m) and quadrupole (18.6 T/m) fields located in the arc section of the beamline, immediately after the PS ring extraction point. The arc section bends the beam about 80°. In addition, there is a series of normal magnets and collimators located in the preparation and final focusing sections of the beamline to adjust the extracted beam. The final focusing section straightens the beam after the arc section such that it adjusts the direction of the beam to hit the production target. The superconducting magnets run with an operational current of 4.36 kA and a maximum temperature of less than 5 Kelvin. They have a 2-hour recovery time from a normal quench. The normal conducting magnets operate in the 1 - 10 kG

range. The T2K target used to produce mesons (pions with a small kaon content) from the extracted proton beam is a helium-cooled isotropic graphite rod of 26 mm diameter and 900 mm in length giving a beam cross-section size of 4.2 mm^2. Three electromagnetic horns generate a toroidal magnetic field to focus the generated charged pions in the forward direction. The horns are driven by a nominal pulsed current of 320 kA synchronized with the proton beam timing. The target is installed inside the inner conductor of the first horn to effectively collect and focus the pions. There is 2.8 mm thick material between the target and the magnetic field consisting of 2 mm of graphite, 0.3 mm titanium-alloy and 0.5 mm of ceramic. The focused pions decay in flight into ν_μ and muons in a 110 m Decay Volume (DV), which is downstream of the horns and is filled with 1 atm of helium gas in order to reduce pion absorption and tritium production. The DV length is optimised to maximise pion decays and reduce muon decays. This helps to limit the already-small fraction of ν_e content produced by decaying muons and kaons.

At the end of the DV is the water-cooled graphite-block beam dump surrounded by 5 m-thick radiation-shielding concrete walls to control potential irradiation of the surrounding earth. Charged particles, in particular any remaining pions but excluding high-energy muons, are stopped by the beam dump.

Figure 3.6 shows a schematic overview of the T2K beamline. Accelerated protons are extracted from the J-PARC beam and are incident upon the T2K target. The resulting pions are then focused by the horn system. The neutrino beam produced by the decay of these pions then flows through a series of detectors, including a muon monitor (MUMON) which monitors the beam position and direction using muons with energy > 5 GeV that survive beyond the beam dump. Beam monitors are described in Section 3.1.1. Figure 3.6 also depicts the relative position and distances between the near and far detectors along the neutrino beamline.

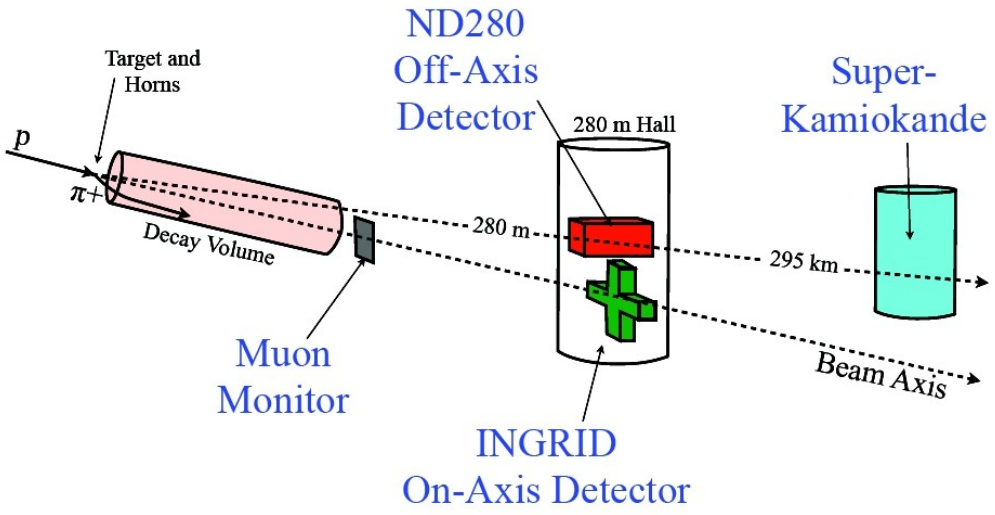

Fig. 3.6. A schematic of the T2K beamline from production at the J-PARC through to the final neutrino beam detected at the far detector. The neutrino beam production components are shown, as are the detector components with respective distances and T2K's off-axis nature [53].

3.1.1 Beamline Monitoring

A shift in the position of the proton beam on the target causes a shift of the ν_μ beam direction which can impact on the measurements of T2K. This means that it is necessary to tune and monitor the beam. Beam monitors measure the position and profile of the p, μ and ν_μ particles. The neutrino beam is carefully studied by a series of monitors at each step of the beam. The position and profile of the beam is monitored by proton beam monitors placed in the beamline and an optical transition radiation monitor (OTR) just before the target. The muon monitor beyond the DV monitors the muons produced by pion decay. The position of the neutrino beam itself is measured by the on-axis neutrino detector (INGRID) at the ND280 site.

The proton beam monitors consist of 5 Current Transformer (CT) Monitors, 50 Intensity Beam Loss (IBL) Monitors, 21 ElectroStatic Beam Position Monitors (ESM) and 19 Segmented Secondary Emission Monitors (SSEM). In combination the beam monitors monitor the beam so that the magnets can be adjusted to acquire a proton beam orbit with a deviation of the orbit from the beamline of less than 1 mm.

The CT Monitors have a linear response up to 90 A and a flat response in the 1kHz - 60 MHz range and measure the beam intensity. The IBL Monitors are gas filled proportional counters that are able to observe a wide range of beam loss. The ESM's, located near the SSEM's, make a non-destructive measurement of the beam field. Each ESM consists of four electrodes that find the beam position by comparing electrode signal sizes. The SSEM's have X- and Y-oriented cathode strips and current is induced by beam incident on the strips. The beam profile is built with the signal from the SSEM's.

The OTR sits immediately upstream of the graphite target. The proton beam crosses a foil which produces optical transition radiation or fluorescent light. The OTR measures the position and width of the proton beam just before it strikes the target.

The MUMON sits downstream of the beam dump and is composed of silicon PIN photo-diodes and an ionisation chamber. It measures the ionisation yield of secondary muons (from pion decays) with energies above 5 GeV in order to reconstruct the muon profile. The muons are produced in conjunction with the neutrinos, hence the MUMON monitors the neutrino beam flux and direction on a spill-by-spill basis and determines the beam position along with the SSEM, ESM and OTR monitors.

3.1.2 Beam Monte Carlo Simulations

A full beamline simulation study of the T2K neutrino beamline was performed using the JNUBEAM (J-PARC neutrino beam flux) simulation that uses GEANT3 [54] simulation and was developed by T2K collaborators. Simulations have also been made using the GEANT version of FLUKA (GFLUKA) and GEANT4 [55] to model hadronic production. The output of these simulations have been compared with data from the NA61 experiment (or SHINE: SPS Heavy Ion and Neutrino Experiment) [56]. NA61 is a wide acceptance spectrometer for the study of hadron production in proton-proton and proton-nucleus collisions at the CERN SPS. The NA61 collaboration inherited the detector components from a predecessor, the NA49

experiment [57], consisting of Time Projection Chambers (TPCs), Time of Flight (ToF) and Projectile Spectator Detectors. These have been upgraded for NA61. In collaboration with T2K, NA61 is measuring the neutrino fluxes, as well as the pion and kaon production cross-sections, from a replica of the T2K graphite beam target with the NA61 detector. In the final T2K beam flux analysis it is likely that a parameterised model for hadron production on the graphite target, based on measurements by the NA61 experiment on a similar target, will be used rather than a Monte Carlo model. This should significantly reduce the main systematic errors on the final neutrino oscillation parameters and cross-sections measured in ND280 and Super-K for the T2K experiment. In October 2007 a pilot run of 30 days was done by the NA61 experiment, during which preliminary physics data was collected for T2K using 30 GeV protons impinging on a 2 cm thin target and also a T2K replica target [56]. The subsequent results are to be made public in the future along with the first T2K publication.

3.2 Near Detectors (ND280)

The near detector suite, which consists of the on-axis INGRID detector and the off-axis ND280, is situated 280 m from the beam target. The ND280 detectors are important for the understanding and measuring the neutrino beam properties before oscillation. In particular the ND280 detectors measure the neutrino beam flux and energy spectrum of ν_μ's and ν_e's for $\nu_\mu \rightarrow \nu_x$ disappearance and $\nu_\mu \rightarrow \nu_e$ appearance, respectively. ND280 also measures background processes that also occur at the Super-K far detector including the measurement of the fraction of ν_e beam contamination in the beam for subtraction from the oscillated $\nu_\mu \rightarrow \nu_e$ appearance measurement. Cross-sections for all ν_μ and ν_e interactions on water as well as carbon are measured by the off-axis ND280 in order to determine the ratio of CCQE, CCnQE and NC interactions. The off-axis near detectors will accurately measure (to a precision of 10%) the NC-π^0 cross-section on water. The NC-π^0 interactions are the main background for $\nu_\mu \rightarrow \nu_e$ appearance in Super-K. Neutral pions readily decay into photons and, if emitted along the axis

of the pion momentum, the result is one hard and one soft photon. The hard photon readily converts in the fiducial volume, producing a cascade of Cerenkov particles. This is indistinguishable from an electron event if the soft photon never converts. Due to the positioning of the detector suite 280 m from the beam source, the near detectors see a much higher event rate than Super-K. Along with the neutrino flux at Super-K, this will provide an estimate of the number of background events, which can be subtracted from the number of ν_e CCQE signal candidates. The near detector suite is separated into two parts; the on-axis INGRID detector and the off-axis ND280 detector. The Interactive Neutrino GRID (INGRID) detector directly measures the neutrino beam flux and profile and is described in more detail in Section 3.2.1. The off-axis ND280 detector is composed of a collection of sub-detectors contained within the T2K magnet. The magnet is discussed in Section 3.2.2. The innermost sub-detectors are assembled inside a steel frame called the "basket", with approximate dimensions of 6.5 x 2.6 x 2.5 m^3 held by an external supporting structure. The direction of the neutrino beam defines the positions of the sub-detectors such that the furthest upstream detector in the basket is the π^0 detector (P0D) followed by three Time Projection Chambers (TPCs) interleaved with two Fine Grained Detectors (FGDs) and finally the DownStream Electromagnetic Calorimeter (DS-ECal) as shown in Figure 3.7. The P0D measures NC-π^0 events, especially those produced in a water target, and is described further in Section 3.2.3. Collectively the FGDs and TPCs are referred to as the Tracker region. The combination of the FGDs and TPCs is primarily intended to measure the fluxes, momentum and energy spectra of the ν_μ beam and ν_e beam contamination. The Tracker region also measures CC cross-sections on carbon and water. The FGD and TPC detectors are discussed further in Sections 3.2.4 and 3.2.5, respectively.

The detectors in the basket are surrounded on all four sides by Electromagnetic Calorimeter (ECal) modules which, except for the DS-ECal mentioned earlier, are fixed to the inner surface of the magnet yokes. The ECals, elaborated upon in Section 3.2.6, measure the energy of particles leaving the P0D and Tracker region and are required for reliable particle identification

(PID) of neutral particles leaving the Tracker region, in particular π^0's. The DS-ECal is the main focus of this thesis and is described in Chapter 4 and then discussed in the remainder of this work. Figure 3.7 shows an exploded image of the off-axis ND280 where the basket containing the sub-detectors can be seen, surrounded by the ECals, all contained within the UA1 magnet. The Side Muon Range Detector (SMRD) is placed in the air gaps between the layers of the magnet return yokes as indicated in Figure 3.7,. The SMRD measures long-range muon trajectories that have vertices in the inner detectors and acts as a veto for particles, particularly muons, entering from outside the detector. The SMRD is described further in Section 3.2.7. The coordinate system of the ND280 is defined such that $+\hat{\mathbf{x}}$ is horizontal to the right of the beam axis when viewed from the beam direction, $+\hat{\mathbf{y}}$ is upward, and the beam is in the $+\hat{\mathbf{z}}$ direction. The origin is at the geometric centre of the off-axis ND280, just upstream of TPC1.

The sections that follow describe the design and physics goals of INGRID and the off-axis ND280 detector. The detectors have been optimised taking into account a number of constraints, including available size for the detector components within the magnet and the need for a magnetic-field-insensitive photosensor for signal readout. The novel Hamamatsu Multi-Pixel Photon Counter (MPPC) photosensor was chosen for signal readout due its small size and because of its ability to operate in a magnetic field. The INGRID detector and all of the ND280 sub-detectors, except the TPCs, are plastic-scintillator-based detectors with WaveLength-Shifting (WLS) fibre and MPPC sensor readout. The scintillator, WLS fibre and MPPC are described in more detail in Section 4.2.

3.2.1 INGRID

The Interactive Neutrino GRID (INGRID) detector is positioned on-axis 280 m from the neutrino production target. Its purpose is to measure directly the neutrino beam flux and profile using muons produced by neutrinos via charged current interactions. It monitors shifts in the beam direction, intensity and mean energy in order to fully understand the neutrino beam profile

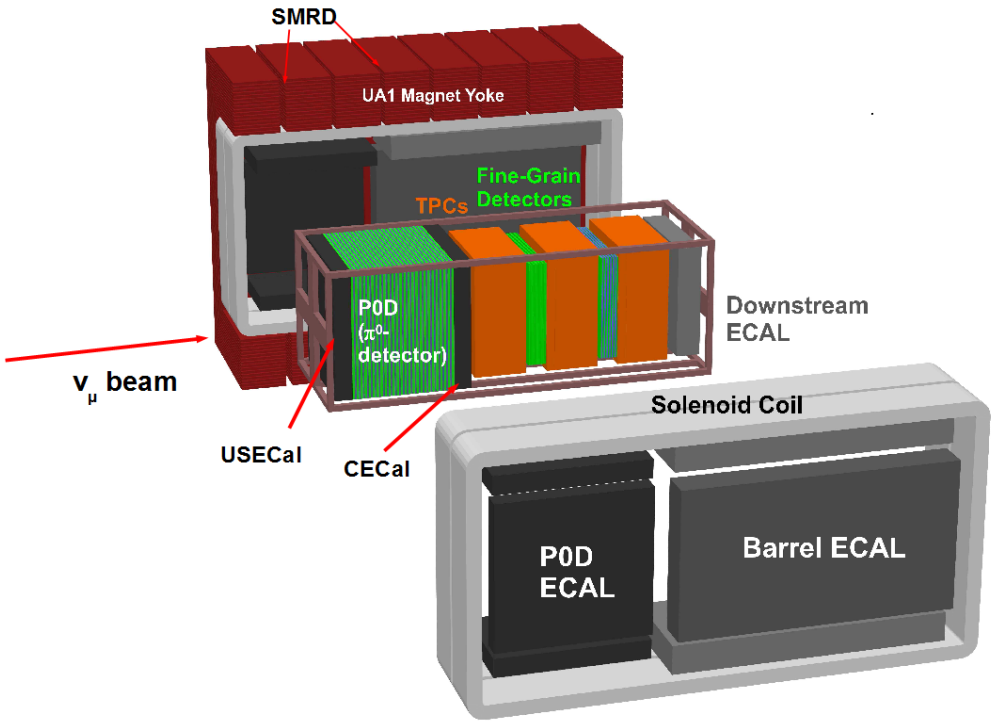

Fig. 3.7. An exploded image of the ND280 off-axis detector. The beam enters from the left of the diagram. The basket region can be seen containing the sub-detectors including the DS-ECal. All other ECal regions surround the basket and the T2K magnet contains all detectors. A Side Muon Range Detector (SMRD) is placed in the gaps of the magnet yoke as indicated [49].

and position. The detector consists of 16 identical iron-scintillator modules. The modules are arranged such that 14 form a cross around the beam centre, 7 in the vertical, 7 in the horizontal direction and 2 are in the off-diagonal directions. This configuration is shown in Figure 3.8. Each module is a sandwich of nine iron target plates, of depth 64 mm and 1.2 x 1.2 m^2 in size, and 11 scintillator tracking planes. A tracking plane consists of one horizontal and one vertical scintillator layer made of 24 scintillator bars. The scintillator bars used for the construction of the INGRID modules are 5 x 1 x 120 cm^3 [58]. Each bar has a central 2 mm hole along its length into which a WLS fibre is inserted. The iron plates act as a target for the neutrinos. Charged particles from the resulting neutrino interactions are detected by the scintillator tracking planes. The scintillation light created in the bars is collected and transported by WLS fibres. The fibres have single-ended readout using the MPPC sensors which will be described in Section 4.2.3.

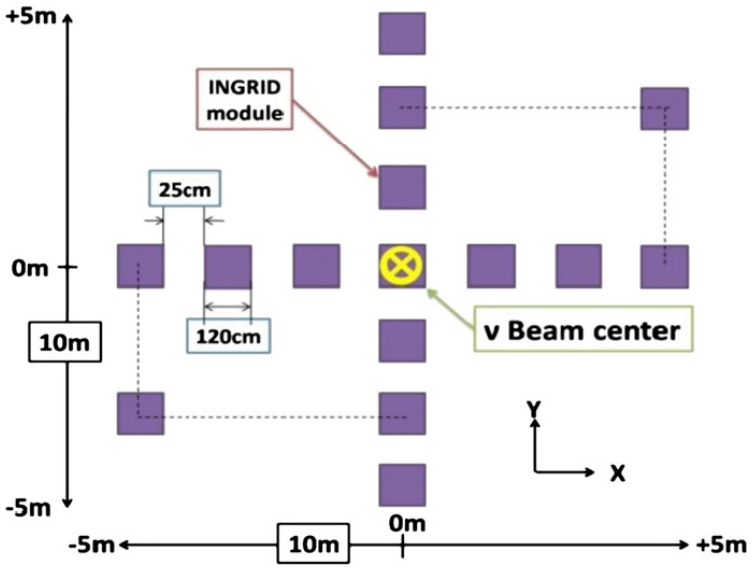

Fig. 3.8. The INGRID detector [49].

INGRID monitors the neutrino beam flux and direction daily by measuring the on-axis neutrino profile. The modules have a low counting rate of 2 - 4 events per beam spill per module, but the combination of all modules allows INGRID to count the CCQE neutrino events and reconstruct the profile and beam centre to a precision of 5 cm. This exceeds the required precision of 28.0 cm which corresponds to a directional shift of 1 mrad.

3.2.2 T2K Magnet

The ND280 off-axis sub-detectors are enclosed inside the refurbished UA1 dipole magnet operating with a horizontal uniform field of 1.8 Tesla, orthogonal to the neutrino beam direction over an inner volume of 88 m^3. The magnet was donated to T2K by CERN and the NOMAD collaboration and consists of two halves which are mirror symmetric about a vertical plane containing the beam axis, as can be seen in Figure 3.7. Each half consists of 8 rectangular C-shaped flux return yokes made of low-carbon steel plates and two coils. The total weight of the yoke is 850 tons. The external dimensions of the magnet, 7.6(L)x 6.1(H)x 5.6(W) m, set a number of constraints on the detector design. The internal volume is 7.0(L) x 3.6(H) x 3.5(W) m,

which determines the available size for the detector components. There are gaps in the magnet yoke, through which the requisite cables and pipes are routed, but there is insufficient space for each channel of the detector to be routed to electronic connections outside the magnet, therefore, each sub-detector within the yoke has its electronics mounted adjacent to the active volume, and the data is carried out by optical Ethernet cables. Normal operation is with the two halves of the magnet in contact. The four coils consist of aluminium conductor bars of square cross-section, 54.5 x 54.5 mm^2, and a central 23 mm diameter bore. Demineralised water is pumped through the inner cavity of the conductor to provide cooling. The coils are composed of individual pancakes which are connected hydraulically in parallel and electrically in series. The total thickness of the coils is 200 mm. The peculiar shape of the coils, forming a hole along the magnet axis, was specifically designed to accommodate the beam pipe in the UA1 experiment.

The 16 C's forming the yoke all have a very similar structure. Each C is segmented in 12 azimuthal sections. Each section is made of 16 iron plates 5 cm thick, with 1.7 cm air gaps between plates. Apart from the corners, the plates at different depth have the same size. Their dimensions are 0.88 x 0.90 m^2 (vertical plates) or 0.88 x 0.70 m^2 (horizontal plates).

3.2.3 The π^0 Detector

The sub-detector furthest upstream in the ND280 basket is the π^0 Detector (P0D) which is designed to measure NC-π^0 interactions, in particular to measure single π^0 production cross-sections on water. It is important that this cross-section be well-understood because it is one of the dominant backgrounds to the ν_e appearance search at the water Cherenkov Super-K detector. The single NC-π^0 interactions on water have only been measured at neutrino energies near 1.3 GeV. This cross-section must be measured at the T2K neutrino energy of approximately 0.7 GeV in order to allow for an accurate background subtraction at Super-K.

The P0D is a sampling tracking calorimeter constructed in three separate regions called Super-P0Dules. A Super-P0Dule consists of active plastic scintillator bar layers called P0Dules

interleaved with an inactive radiator or target. The central Super-PODule has a water target section and sits between upstream and downstream electromagnetic calorimeter Super-P0Dules which have lead targets. The three Super-P0Dules can be seen in Figure 3.9.

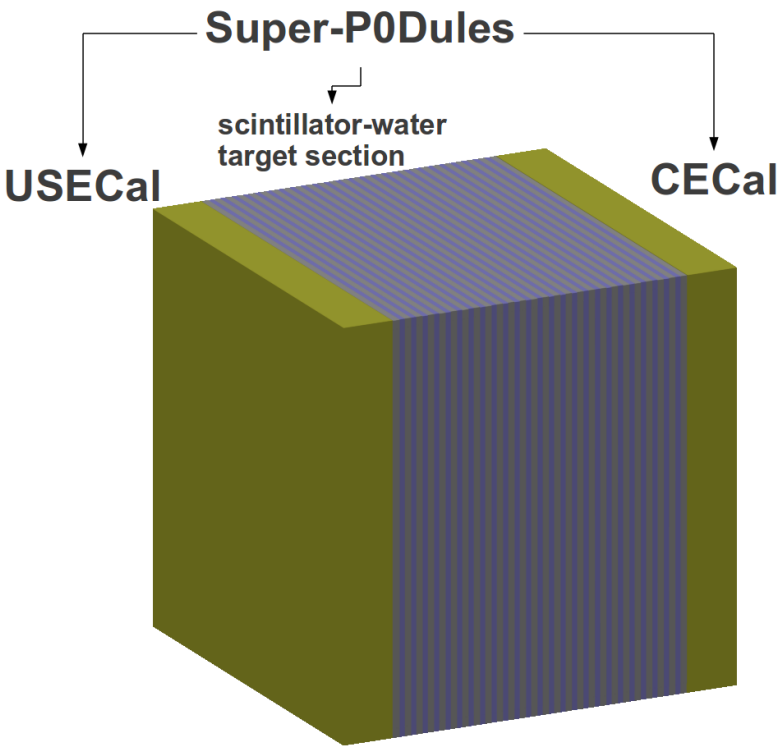

Fig. 3.9. The three Super-P0Dule regions of the P0D. The central Super-P0Dule is made of 26 P0Dules alternating with 25 water target 'layers' and sits between the upstream (upstream ECal - USECal) and downstream (central ECal - CECal) Super-P0Dules. The USECal and CECal are made of 7 alternating scintillator-lead layers [49].

The central Super-P0Dule section, labeled as the scintillator-water target section in Figure 3.9 is made of 26 P0Dules alternating with 25 water target 'layers' and provides the fiducial mass for π^0 measurement. The P0Dules have dimensions of 220 cm ($\hat{\mathbf{x}}$) x 234 cm ($\hat{\mathbf{y}}$)x 3.9 cm ($\hat{\mathbf{z}}$) and consist of two tracking planes made from plastic scintillator bars. The planes are perpendicular to each other to create an alternating $\hat{\mathbf{x}}$-$\hat{\mathbf{y}}$ configuration and are held between two thin sheets of PVC to keep the P0Dule light tight. The scintillator bars are triangular and measure 17 mm in height with a 32.5 mm base, in contrast to the thin rectangular scintillator bars used

in all of the other sub-detectors. The triangular bars increase the spatial resolution and pointing ability of the P0D. The bars also have a central hole holding a WLS fibre which is attached to a MPPC at one end; the opposing end is mirrored. A brass radiator sheet of 1.6 mm thickness is placed between a P0Dule and the water in order to convert photons and enhance electromagnetic (EM) shower production. The water 'layers' are constructed from semi-flexible pillow bladders, with nominal dimensions 2.10 x 1.80 x 0.03 m^3 and hold approximately 100 kg of water each. Measurements of neutrino-induced pion-production cross-sections on oxygen are made with the P0D by comparing the interaction rate of events with the water target filled versus water removed. The energy deposited in the active tracking region can be measured and the invisible energy deposited in the passive water sections can be inferred by an absolute energy calibration constant.

The upstream and downstream EM calorimeter Super-P0Dule's are referred to as the upstream (USECaL) and central (CECal) ECals respectively, providing energy containment of showers as well as active shielding. They are not to be confused with the P0D-ECal which is described in Section 3.2.6. The USECal and CECal are constructed from triangular scintillator bars and occupy a different region of the ND280 (see Figure 3.7). The USECal and CECal consist of seven scintillator-lead layers in alternating $\hat{\mathbf{x}}$-$\hat{\mathbf{y}}$ direction. The scintillator layers are constructed from 128 scintillator bars in the $\hat{\mathbf{x}}$ and 136 bars in the $\hat{\mathbf{y}}$ direction.

All scintillator layers in the Super-P0Dules are made light-tight with end caps that also provide a manifold to bring the WLS fibres out of the bars and into the MPPC housing.

3.2.4 Fine-Grained Detectors

The Fine-Grained Detectors (FGD) provide the target mass for neutrino interactions in the Tracker region of ND280, and identify and measure the trajectories or "tracks" of the charged particles that cross them. The FGDs also measure neutrino interaction vertices and determine if tracks are from the same neutrino interaction vertex. The fine-grained nature of the detectors

is derived from the high position resolution that is obtained from instrumentation with small cross-section, 0.96 cm^2, plastic scintillator bars. There are two FGD modules in ND280 each with 1.0 ton of active target material. The upstream FGD (FGD1) consists entirely of plastic scintillator, while the downstream FGD (FGD2) has plastic scintillator and water layers interspersed. Comparing the interaction rates in the two FGDs permits an independent determination of cross-sections on carbon and water from that obtained in the P0D. Due to the different target masses of the two FGDs, the interaction rate in FGD1 can be subtracted from the interaction rate in FGD2 (with a scaling factor to account for the different masses and detection efficiencies) to determine the neutrino interaction rate on water alone. Since the Super-K detector is composed of pure water, interactions can be compared between the near and far detectors in this way.

The bars are assembled into 'XY Modules' which consist of one layer of 192 bars in the $\hat{\mathbf{x}}$ direction glued to 192 bars in the $\hat{\mathbf{y}}$ direction. Thin 0.25 mm sheets of epoxy fibreglass are glued to the outer surfaces of the XY Modules for added rigidity and ease of handling. FGD1 consists of 15 XY Modules (5760 scintillator bars), while FGD2 consists of seven XY Modules alternating with six 2.5 cm thick layers of segmented polycarbonate panels filled with water (2688 scintillator bars and 15 cm total thickness of water). Each scintillator bar has dimensions of 186.24 cm x 0.96 cm x 0.96 cm with a 1.8 mm hole down its centre for insertion of a mirrored WLS fibre for single-ended readout by MPPCs. The final outer dimensions of each FGD module is 186.24 x 186.24 x 2.04 cm^3 [59]. The XY Modules are suspended inside a light-tight 'Dark Box' in order to be tolerant to damage from earthquake accelerations up to several g's and to have a position resolution of approximately 1 mm. Each module is supported by stainless steel straps which loop around the bottom of the module and attach to anchor points in the aluminium frame of the Dark Box.

3.2.5 Time Projection Chambers

The Time Projection Chambers (TPCs), along with the FGDs, make up the Tracker region of the off-axis ND280 detector, which is optimised for the study of neutrino interactions that produce energetic charged particles. The three TPC modules, one on either side of each FGD, are designed to reconstruct charged particle tracks with excellent 3D granularity. Their location in relation to other detectors in ND280 can be seen in Figure 3.7. The TPCs measure the momentum of the muon produced in the CCQE interactions in order to reconstruct the neutrino energy and energy loss per unit length (dE/dx) for the purpose of particle identification. They have been designed to discriminate electrons from muons in the 0.3 - 1.0 GeV/c momentum range. Three TPCs are required in order to measure the momenta of particles coming from the two FGD targets. The upstream TPC measures the momentum of back-scattered particles from the upstream FGD as well as high momentum muons exiting the P0D in the forward direction, while the other two TPCs measure the momentum of forward-going particles exiting the FGDs. Each TPC module has a double wall structure. The outer wall is 1.0 x 2.5 x 2.5 m^3 and contains a central active volume within the inner wall measuring 0.7 x 1.8 x 2.0 m^3 which is filled with a Ar:iC_4H_{10}:CF_4 (95:3:2) gas mixture. The inner wall makes up the field cage and drift volume while the outer wall forms a CO_2 volume that provides high voltage insulation. The CO_2 also serves to exclude oxygen, nitrogen, or other contaminants from entering the inner volume. The CO_2 gap is 68 mm on the top and sides and 118 mm on the bottom, where extra space is needed for the cathode HV connection [60].

The drift volume is split in half in the $\hat{\mathbf{x}}$ direction by a central cathode plane in $\hat{\mathbf{y}}\hat{\mathbf{z}}$. The two end plates parallel to the central cathode plane are segmented with detector units each of area 360 x 340 mm^2. These readout planes are instrumented with the 'bulk' Micromegas technology, a novel technique for manufacturing an all-in-one detector in a single process that was developed in 2004 by a CERN-Saclay collaboration and is described in detail in [59].

The bulk Micromegas technology is a technical solution to minimise dead zones on the edges of the modules and to improve gas gain uniformity, especially in the corners. The Micromegas module is composed of an anode segmented Printed Circuit Board (PCB) on which an inox[6] micro-mesh is integrated using photo-lithography techniques. Each module is 360 x 340 cm^2 with an array of 6.9 x 9.7 mm^2 pads leading to 1728 channels, arranged in 48 rows of 36 pads each of which is read out by 6 front-end electronic cards (FEC's), each containing 4 AFTER[7] chips designed at Saclay. One corner of the Micromegas module, a two-pads equivalent surface, is reserved for the micro-mesh high voltage supply connection from the backside of the PCB. A total of 72 of these Micromegas modules are used to instrument the 3 TPCs (12 modules per readout plane, 2 planes per TPC) for a total of 124,416 pads. Figure 3.10 shows one such Micromegas module with the high voltage supply connection highlighted.

The electrons produced by an ionising particle crossing the TPC gas drift toward the anodes of the Micromegas modules that are interspersed between the pad arrays. An electron that reaches the micro-mesh, held at 50 - 100 μm above the anode, initiates an avalanche of electrons which amplifies the original ionisation.

Figure 3.11 is a picture of the inside and outside of one completed plane of the TPC module equipped with 12 Micromegas modules and the AFTER electronics.

3.2.6 Electromagnetic Calorimeters

The Electromagnetic Calorimeter includes two distinct sections, a Tracker ECal (TECal) and a π^0-detector ECal (P0D-ECal), and consists of 13 modules in total. The TECal identifies interactions occurring outside the inner tracking detectors which produce event signatures that mimic those of neutrino interactions in the fiducial volumes of the inner detectors. The P0D-ECal identifies photons from NC-π^0 interactions exiting the P0D.

[6] Synonym for stainless steel.

[7] AFTER (ASIC For TPC Electronic Readout) chip is a 72 channel ASIC (Application Specific Integrated Circuit) specifically designed for T2K.

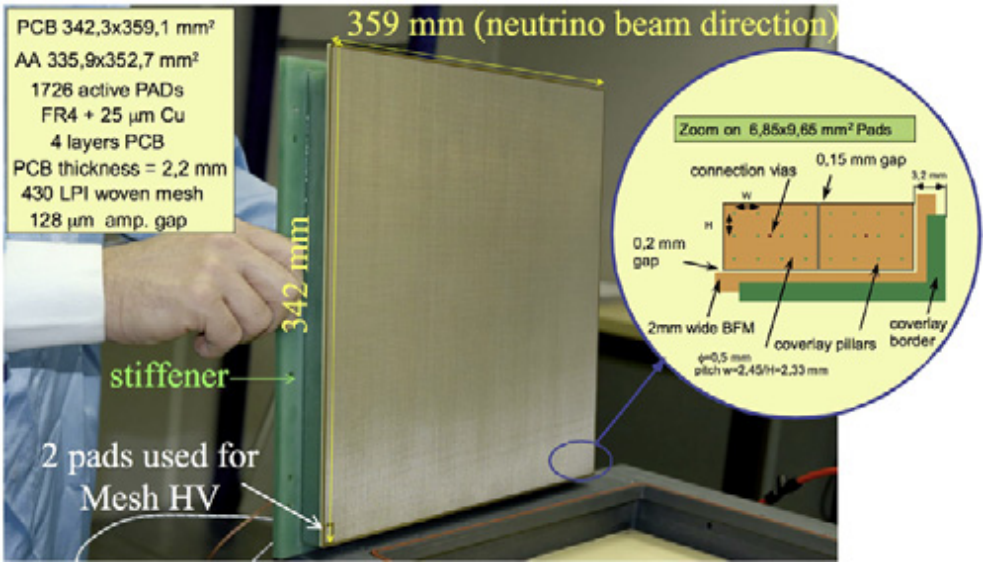

Fig. 3.10. A TPC 'bulk' Micromegas module. The Micromegas is composed of a segmented PCB with an array of pads arranged in 48 rows of 36 pads each apart from a corner where a two pads equivalent surface is reserved for the micro-mesh high voltage supply connection from the backside of the PCB [59].

The TECal section is composed of a Barrel ECal (BrECal) and the Downstream ECal (DS-ECal). The BrECals sit outside the basket and surround the Tracker region of ND280, with the DS-ECal positioned at the downstream end of the Tracker region inside the tracker. There are 6 modules in the Barrel ECal: 2 Top, 2 Bottom and 2 Side. The DS-ECal is a single module. The TECal detects, reconstructs, and identifies particles leaving the tracking volume, with an energy resolution of $\sim 10\%/\sqrt{E}$. The TPCs will already have measured the momentum of many charged particles, but the ECals have a greater coverage of area and have sufficient mass to trigger a shower from neutral particles like photons that are not observed in the TPCs. This further fulfills the main purpose of the TECal as an aid for the Tracker region in fully reconstructing neutrino interactions in the FGDs.

The TECal plays an important role in the energy measurement of electrons from beam ν_e CC interactions, especially for electrons with momenta above 1 GeV/c. The shower reconstruction capabilities of the TECal have been chosen to allow it to correctly reconstruct photons

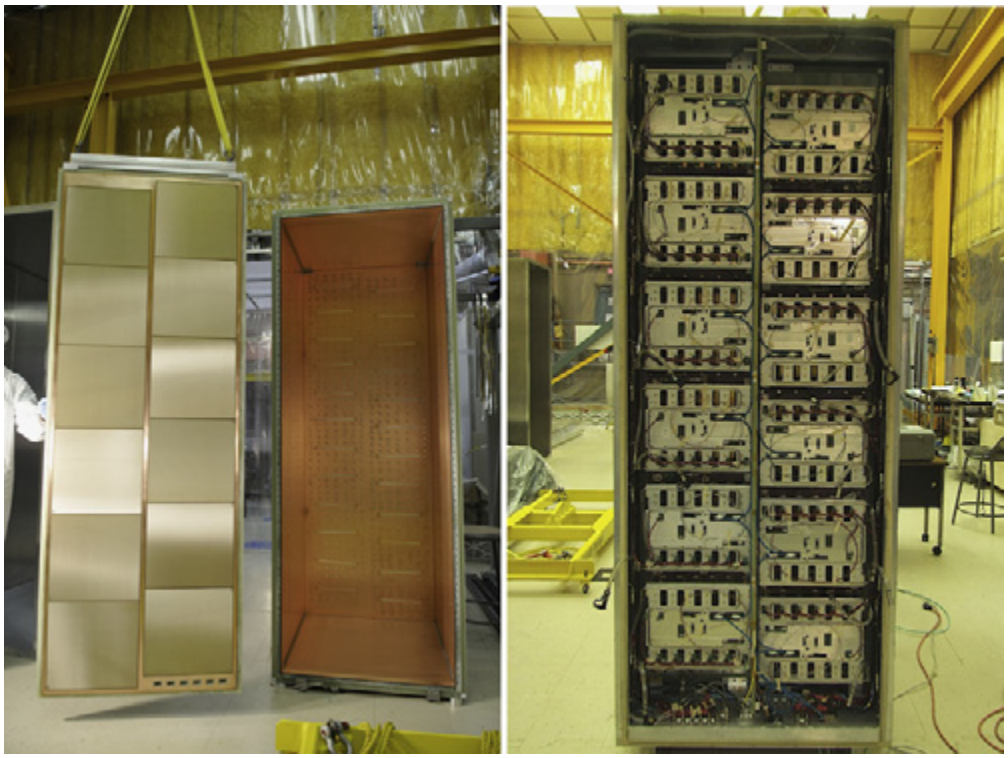

Fig. 3.11. One TPC readout plane equipped with 12 Micromegas modules and front-end AFTER electronics, seen from the inside (left) and outside (right) of a completed TPC module [59].

created from π^0 decays, to measure their invariant mass and determine if they were produced in the FGDs.

Like the P0D, the ECal modules are tracking sampling calorimeters. Each module uses alternating layers of plastic scintillator bars and lead. The lead is especially important for detecting photons, which will not produce a signal in the detector until they have been made to produce an EM shower, creating a cascade of electrons and positrons.

The 6 P0D-ECal modules sit outside the basket upstream of the TECal and surround the P0D detector. The P0D-ECals' primary purpose is to positively identify photons and muons escaping the P0D. It is not intended to have the same tracking capabilities as the TECal. The ECal is discussed in depth in Chapter 4 as its construction and calibration is the subject of this thesis.

3.2.7 Side Muon Range Detector (SMRD)

The SMRD is used to measure the range and estimate the momentum of muons from CCQE interactions, as well as providing a veto of through-going cosmic ray muons. It also is used as part of a cosmic ray trigger which is used for calibration of the ND280 sub-detectors. The SMRD plastic scintillator planes are placed inside the magnet yokes in the gaps between the iron plates of the yoke, using the iron to range out the muons. Each C of the magnet yoke is made of eight segments, referred to as C's because of their shape as described in Section 3.2.2. A single C consists of 16 48mm-thick iron plates, with 17 mm air gaps between them, and is segmented into 12 azimuthal sections. The air gaps are of dimensions 876 x 910 x 17 mm^3 for the horizontal and 876 x 700 x 17 mm^3 for the vertical. [61].

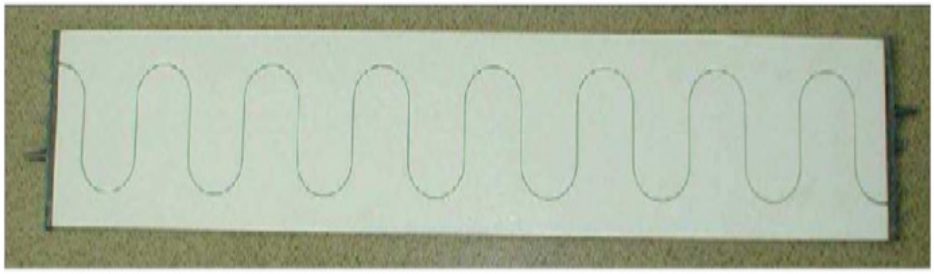

Fig. 3.12. A single SMRD scintillator slab instrumented with the WLS fibre embedded in the S-shape groove [61].

All magnet C's have three modules in both the top and bottom regions, and the side regions vary from two modules for the three most upstream C's to six modules for the two downstream ones. An SMRD module consists of four counters of size 876 x 175 x 7 mm^3 or five counters measuring 876 x 167 x 7 mm^3 for horizontal and vertical gaps, respectively. A single counter is an extruded plastic-scintillator slab with double-ended WLS fibre readout. The WLS fibre is glued into a 4 mm-deep serpentine groove.

Figure 3.12 shows a single SMRD scintillator slab instrumented with the WLS fibre embedded in the groove. A straight fibre would not receive enough light from particles passing through the edges of the scintillator slab. The fibre is read out at each end by MPPCs. The MPPCs from each azimuthal section of a C are connected to the same electronics front-end board, so that "towers" are created which can be used to produce cosmic ray triggers. Each counter is wrapped in an additional reflector layer of 0.1 mm-thick Tyvek paper which increases light yield by approximately 15%. The counters are then wrapped in 0.1 - 0.15 mm-thick stainless steel foils in order to protect the counters from light, humidity and possible mechanical damage during installation.

3.3 Far Detector (Super-Kamiokande)

Super-Kamiokande (Super-K) is the far detector for T2K. Super-K first started taking atmospheric and solar neutrino data in 1996. It was designed to search for proton decay but had the ability to detect solar neutrinos in the hope of solving the solar neutrino problem as described in Section 2.3. As can be seen in Figure 3.13, Super-K is a cylindrical water-Cherenkov detector measuring 39.3 m in diameter and 41.4 m in height, which makes it the world's largest water Cherenkov detector to date.

The Super-K detector is located 1000 m underground in Hida-city, Gifu prefecture, Japan under Mt. Denoyama so that it is shielded from all but the very high energy cosmic ray muons, which have at least 1.3 TeV momentum. It contains 50 kT of pure water and has a 22.5 kT fiducial volume. Super-K is instrumented with Hamamatsu Photo-Multiplier Tubes (PMTs). The PMT support structure divides the water tank into two distinct, optically isolated volumes: the inner detector (ID) and the outer detector (OD). The ID is instrumented at intervals of 70 cm leading to a 40% PMT coverage from a total of 11,129 20-inch PMTs covered with acrylic and fibreglass shields. The rest of the detector wall is covered with black polyethylene terphthalate sheet which optically separates the ID from the OD. The inward-facing photo-sensors of the

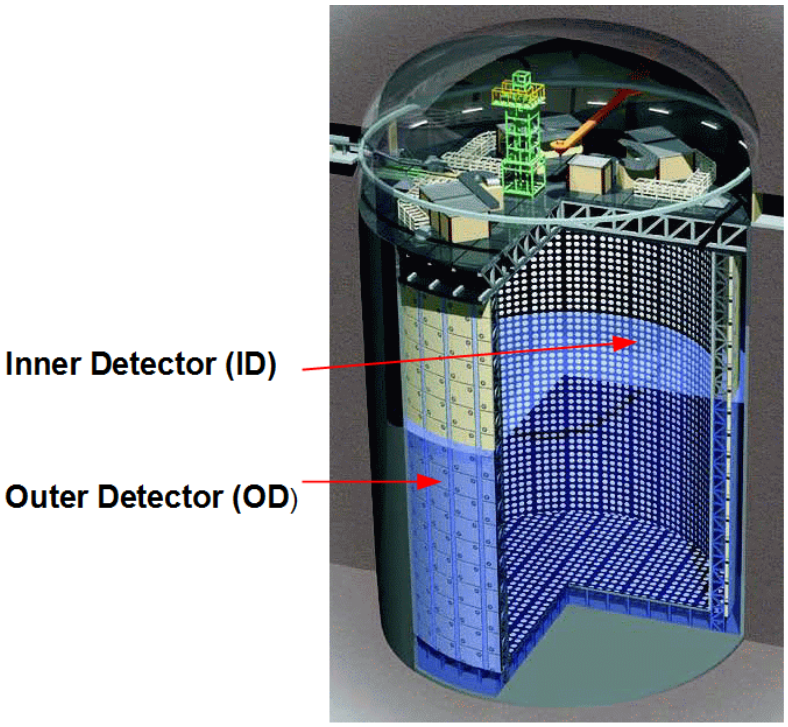

Fig. 3.13. A drawing of T2K's far detector, Super-Kamiokande. The detector is 1000m underground beneath Mt. Denoyama and is a cylindrical tank filled with 50 kT of pure water. The differing number of PMTs lining the ID and OD walls can be seen and the electronics hut above the water tank is shown [49].

ID detect the Cherenkov light emitted by charged particles as they pass through the water. In the OD, 1,885 8-inch outward-facing PMTs are instrumented with the main purpose of distinguishing neutrino events from cosmic ray muon events. The cosmic ray muons are background sources of the neutrino observation.

Chapter 4

Electromagnetic Calorimeter: Design and Construction

The ECals surround the entire basket region and are designed to identify and measure the energy of electrons, positrons, muons and photons produced in the Tracker region, and to identify photons and muons exiting the P0D region. It is important that the ECals convert and measure the energy of photons which would not have been seen by the inner detector TPCs. In the Tracker region, the TECals are required to separate the EM showers of electrons from the hadronic showers from pions in the energy range 500 MeV to 10 GeV and measure events that produce π^0's since these events are largely undetected in the Tracker detectors. Another important task for the ECals will be contributing to the measurement of CCQE muon interactions. The ECals cover the largest active area in ND280, stretching almost twice the width and height of the FGD fiducial volumes. The large mass of the ECals results in a high rate of interactions, and by positively identifying the outgoing muons (and high energy protons) from CCQE interactions the ECALs improve the understanding of the neutrino beam properties.

As mentioned previously in Section 3.2.6, there are 13 ECal modules in total in the ND280 off-axis detector. The modules are constructed with identical materials and similar design, differing only in size.

4.1 DS-ECal

The DownStream Electromagnetic CALorimeter (DS-ECal) is a tracking lead-scintillator sampling calorimeter consisting of 34 layers. It is situated downstream of the Tracker region at the back of the basket within ND280. The scintillator and wavelength-shifting fibre techniques and materials used in the DS-ECal and all other subsequent ECals are well established, and relatively simple. The MPPC sensors are the only novel components that are used and as such a

number of tests to optimise performance and working techniques with these devices were carried out by other institutions.

4.1.1 Detector Design

For each ECal module in the ND280 off-axis detector, the local $\hat{\mathbf{z}}$ direction is oriented to point back into the tracker region so that all particles of interest will cross lead-plastic scintillator layers, instead of running parallel to them. This allows for three dimensional position reconstruction of tracks using the two views, $\hat{\mathbf{x}}\hat{\mathbf{z}}$ and $\hat{\mathbf{y}}\hat{\mathbf{z}}$ due to the alternating $\hat{\mathbf{x}} - \hat{\mathbf{y}}$ orientation of ECal layers. Table 4.1.1 gives a complete breakdown of each of the ECal configurations in the ND280 off-axis detector.

	DS-ECal	Barrel ECal	P0D ECal
Length	2.5m	3.9m	2.4m
Width	2.5m	3.2m	3.2m
Layers	34	32	6
Bar orientation	$\hat{\mathbf{x}}/\hat{\mathbf{y}}$	Longitudinal and Perpendicular	Longitudinal
Bars	1700	2432 Long. top/bottom 1888 Long. sides 6144 Perp. top/bottom 3072 Perp. sides	912 Long. top/bottom 708 Long. sides
Bars per layer	50	38 Long. top/bottom 59 Long. sides 96 Perp. top/bottom/sides	38 Long. top/bottom 59 Long. sides
Bar length	2.0m	3.835m Longitudinal 1.523m Perp. top/bottom 2.35m Perp. sides	2.340m
Pb Thickness	1.75mm	1.75mm	4.0mm

Table 4.1. ECal module design dimensions. "Longitudinal" bars refers to those whose long axis lies parallel to the beam direction, or to $\hat{\mathbf{z}}$ in ND280 off-axis coordinates.

The scintillator bars in all ECals have a cross-section of 4 cm x 1 cm. There are 6 modules in the Barrel ECal (BrECal): 2 Top, 2 Bottom and 2 Side. The same is true for the P0D ECal. The BrECals surround the Tracker region of ND280, with the DS-ECal positioned at the downstream end of the Tracker region. The P0D ECals surround the P0D detector. Referring to

Table 4.1.1, the BrECal modules are the biggest of all ECals, measuring ~ 4.0 x 3.2 m^2. The P0D ECals contain the same number of bars per layer as the Longitudinal Top/Bottom and Side BrECal modules because each P0D ECal module has the same width as the corresponding BrECal module, and all of the layers in the P0D ECal modules have the bars running longitudinally but the bars are shorter, measuring 2.340 m compared to 3.835 m. The P0D ECal also consists of 4.0 mm-thick lead in contrast to the 1.75 mm-thick lead in the DS-ECal and BrECals. The bars in the DS-ECal and the longitudinal bars in the BrECal have double-ended readout. All other bars have single-ended readout.

The completed DS-ECal module measures 2.5 m x 2.5m and is composed of 34 lead-plastic scintillator layers with a total of 3400 MPPC readout channels. The corresponding number of layers in the other ECal modules are listed in Table 4.1.1. Each layer features 50 scintillator bars of dimension 2016(L) x 40(W) x 10(H) mm glued side-by-side. Two lead sheets measuring 2 m x 2m x 1m each are glued on top of the scintillator bars. The lead is of 1.75 mm thickness. The scintillator bars are aligned perpendicular to the previous layer of scintillator in order to construct an alternating $\hat{\mathbf{x}}$-$\hat{\mathbf{y}}$ orientation for three dimensional reconstruction of tracks. The scintillator bars have a 2 mm central hole with a 2m-long 1mm-diameter wavelength shifting fibre (WLS) inserted down the middle through the length of the scintillator bar. Each scintillator bar is coated with TiO_2 to reflect escaping light back inside the scintillator in order to increase the capture efficiency of the WLS fibre. A MPPC sensor is connected to each end of the WLS fibre for bars with double-ended readout. As a result, there are also 50 WLS fibres per layer with double-ended MPPC readout, hence 100 MPPCs per layer. MPPCs were used rather than photomultiplier tubes because they are cheaper, small and, unlike photomultiplier tubes, they are insensitive to magnetic fields. These MPPC sensors are attached via one m-long mini-coaxial cables to a channel on a Trip-t Front end Board (TFB) for electronics readout. The TFBs are described in more detail in Section 4.2.4 and the MPPCs are described further in Section 4.2.3.

The WLS fibres are required as the scintillator bars have a very short attenuation length ($\sim$ 40cm) which would result in large losses of signal over the distance of the bar. These WLS fibres have two attenuation lengths: a long attenuation length which is much larger than the length of the scintillator bar, and a short attenuation length which is due to light becoming trapped in the cladding of the WLS fibre. The WLS fibres, which shift the wavelength of all light to the green region of the spectrum, are used rather than optical fibre because the MPPCs are more sensitive to light of wavelength close to 500 nm. The WLS fibres are detailed further in Section 4.2.2.

4.1.2 Importance within ND280

The DS-ECal will mostly detect particles that have interacted further upstream in the ND280 detector. The primary purpose of the DS-ECal is to help to identify CCQE interactions and will use TPC momentum where possible in order to measure the energy of the muon neutrino. The DS-ECal is also responsible for identifying π^0s through the detection of two photons from the decayed pion.

4.2 Materials

The following sections describe the key construction materials for all sub-detectors in ND280, except the TPC modules. The sub-detectors employ a modular scintillator-lead layer scheme with WLS fibre readout to MPPCs. The MPPC signal is digitised by TFB electronics readout.

4.2.1 Plastic Scintillator and Lead

As mentioned, all sub-detectors (except TPCs) in ND280 use plastic scintillator as their active material. The plastic scintillator bars are extruded from a common material at FNAL as described in more detail in Ref [62]. Briefly, the extrusion process heats pellets of polystyrene,

with the addition of two scintillating dopants which are described below, and then forces the mixture through an extrusion die. The die determines the cross-section of the bars and is varied for the required cross-section of each sub-detector. FNAL use a die that produces a 4 x 1 cm^2 rectangular bar for the ECals, with a central 2 mm hole through which the WLS fibre is threaded. The heated mixture is forced through the die continuously so that it is possible to vary the length of the bars. Dimensions for the scintillator bars used in the construction of the ECals are recorded in Table 4.1.1 in Section 4.1.1.

Polystyrene does not naturally scintillate, so two dopants are added to the polystyrene. The dopants are poly(p-phenylene oxide), or PPO, and 1,4-bis(5-phenyloxazol-2-yl) benzene, or POPOP. PPO is included as a 1% dopant and is an organic scintillator whose purpose is to absorb the ionising energy of traversing particles which excite a π-orbital electron into a higher energy state. The de-excitation of the electron emits a photon which is the signal for the electronics. Maximum fluorescence occurs at short wavelengths of approximately 340-400 nm.

POPOP is included as a 0.03% dopant and as a WLS scintillator. The short-wavelength photons produced by PPO are quickly attenuated in the scintillator, so POPOP is added to absorb this primary scintillation light and to re-emit a photon at a longer wavelength with the spectrum peak at 410 nm.

A quenching effect is observed in scintillators because the ionisation light produced by the traversing particle must interact with a dopant molecule to produce scintillation light. The light produced increases with the energy deposited but this decreases the availability of dopant molecules, limiting the growth. The effect is described by Birks' semi-empirical formula [63]:

$$L(E) \propto \int_{E_{min}}^{E_{max}} \frac{1}{1 + k_B . \frac{dE}{dx}} . dE, \tag{4.1}$$

where k_B is a material-specific parameter and $\frac{dE}{dx}$ is the energy loss. This effect has been studied in detail for plastic scintillators [64], and is especially important for protons which can deposit a large amount of energy in a short track.

4.2.2 Wavelength-Shifting (WLS) Fibres

WLS fibres are threaded through the central hole of the scintillator bars to carry the light signal to the MPPCs for readout. The WLS fibres chosen are Kuraray Y11 (200) S-35 green multi-clad fibres which have an attenuation length of approximately 350 cm. This attenuation length is a large focus of this thesis and is discussed further in Chapter 8. The attenuation length is much longer than the attenuation length of the scintillator which is approximately 40 cm [65]. The short attenuation length of the scintillator bars would result in an unacceptable loss of light in the ECal bars which have lengths up to 4 m.

The WLS fibres are required to match both the peak emission of the scintillator bars which emit in the blue region of the electromagnetic (EM) spectrum, and the sensitivity of the MPPCs which have a peak sensitivity in the green region, i.e. the WLS fibres should have absorption peaking in the blue region and emission peaking in the green region of the EM spectrum. The chosen fibres have an absorption peak of 430 nm and emission peak of 476 nm. The WLS fibres were also chosen because they are robust against mechanical stress and aging effects. The WLS fibres measure 1 mm in diameter and are double-clad. The respective reflective indices within the WLS fibres are 1.59 (core), 1.49 (inner) and 1.42 (outer).

4.2.3 Photosensors

Signal in the ECal modules is produced by particles traversing the plastic scintillator bars, depositing energy and inducing ionisation. The scintillator material absorbs the deposited energy and re-emits it in the form of scintillation light. This light is collected by the WLS fibres and travels via total internal reflection along their length to the ends. At these ends a

photosensor is required which converts the scintillation light collected by the WLS fibre into an electric signal that can be read out electronically. The choice of photosensor is driven by the physics requirements such as gain and photon detection efficiency (PDE), overall detector design, and cost per unit because of the large number of channels in the ECal (~23,000). The first and most important requirement is that the chosen photosensor is able to perform within a magnet as the ND280 detectors are enclosed within the UA1 magnet. The photosensor size is also limited concurrently due to the constraints of limited space within the UA1 magnet. The novel MPPC developed by Hamamatsu photonics fulfill all of these requirements and is the sensor of choice for the T2K near detectors [66]. Each MPPC consists of 667 pixels of width 50 μm, forming a 1.3 x 1.3 mm^2 active area as shown in Figure 4.1.

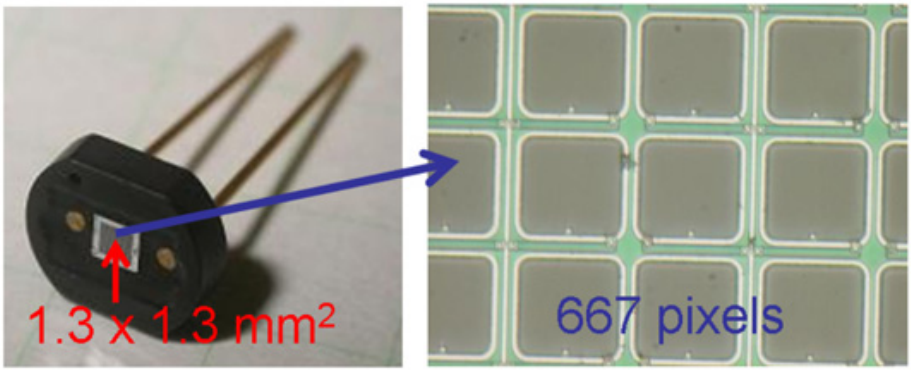

Fig. 4.1. Photographs of a 1.3 x 1.3 mm^2 type MPPC (667 pixels) developed by Hamamatsu photonics for the T2K experiment. Left: entire device. Right: close-up view of APD pixels with 50 μm pitch.

The MPPC, also known as a Geiger Mode Avalanche PhotoDiode (GM-APD) or a Silicon PhotoMulitplier Tube (SiPMT), is an array of avalanche photodiodes (APDs) on a single wafer, with a single pair of electrical contacts. The MPPCs are based on Geiger mode reverse biased P-N junctions which emit a pulse of electrons upon the impact of a photon and are operated above reverse breakdown voltage. A single incoming photon triggers a Geiger avalanche in a pixel and each pixel discharges and resets independently of the rest of the device because

the MPPC is quenched by a built-in resistance in series with the APD junction. Each pixel contributes a fixed amount of charge to the output, thus the total MPPC output charge is generally proportional to the number of pixels fired. The proportionality decreases as the limit of the MPPC's dynamic range is reached, bound by the the number of pixels on the device. The sensors have comparable performance to PMTs such as gain of the order 5 x 10^5 - 1 x 10^6 and a PDE of $\sim$ 30 %. They are capable of photon counting at low light level and have a time resolution of $\sim$ 250 ps which is negligible compared to the WLS fibre decay time. The gain of a single device is defined as

$$G \equiv \frac{Q_{\mathrm{SPE}}}{e}, \tag{4.2}$$

where Q_{SPE} is the output charge corresponding to a single Geiger discharge, often called single photo-electron (SPE) signal, and e is the electron charge. The dark noise rate is the counting rate for a given threshold when no light illuminates a sensor. The PDE is defined as the probability that a signal is observed when a photon hits a MPPC. The cross-talk rate is the probability that a Geiger avalanche is triggered in the neighbouring pixels when a single pixel is fired.

As well as being comparable to PMTs, the MPPCs have some important advantages including low cost, low operating voltage of $\sim$ 70V. Importantly for the T2K experiment, they are insensitive to magnetic fields and are small enough to fit within the space constraints presented by the UA1 magnet.

The long-term behaviour of the MPPCs is not yet well understood so that a MPPC calibration/monitor system is required. A Light Injection (LI) system is employed for calibrating and monitoring the MPPCs in the long-term. First and foremost, the LI system serves the purpose of testing the integrity of each MPPC channel. The system also has the ability to scan the gain of photosensors with a variable intensity light output. The LI system achieves this by flashing the MPPC sensors with a light-emitting diode (LED) signal.

4.2.4 Electronics

The front end electronics readout system for the ND280 detectors, shown in Figure 4.2, is based on the Trip-t chip, originally used at Fermilab for Visible Light Photon Counter readout for the Tevatron D0 experiment [67]. Each Trip-t Front end Board (TFB) is designed to control and read out up to 64 MPPC sensors. The DS-ECal is instrumented with 56 such TFBs (14 each side) to read out 3400 MPPC sensors. Figure 4.3 shows one such TFB attached to the completed DS-ECal module and connected to 64 MPPCs. The data from the TFBs is processed through two Readout Merger Modules (RMM) which provide the communication interface with the off-detector data acquisition system (DAQ). Each RMM processes up to 48 TFBs. Cosmic ray trigger primitives are formed on a TFB from a time coincidence between signals from a number of MPPC channels and transmitted to a Cosmic Trigger Module (CTM) where a global trigger decision is made.

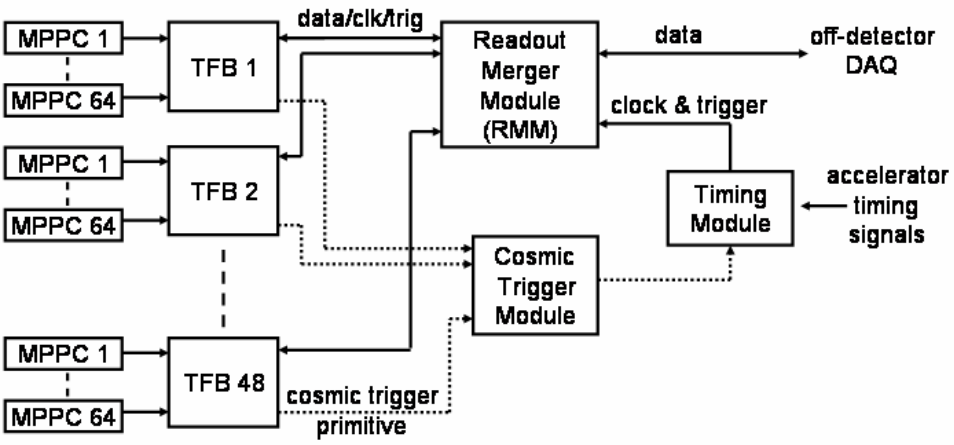

Fig. 4.2. The front end electronics readout system for the ND280 detectors. Data signal enters from the left in the form of an electrical pulse, or charge, from the MPPCs. This is channeled into a specific connection on a TFB, and subsequently fed through to the RMM where it is coupled with a time-stamp.

The input MPPC signal is divided into low and high gain channels, using 2 Trip-t channels per MPPC, in order to accommodate the full range of MPPC signal sizes and to be able to

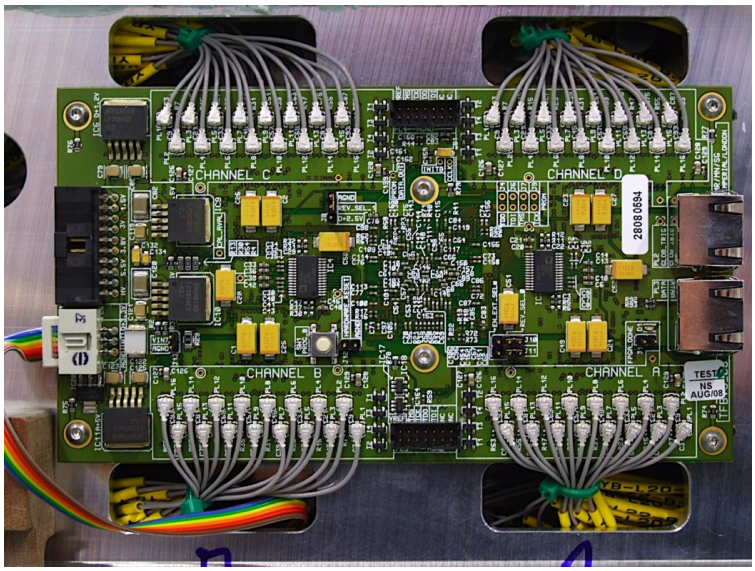

Fig. 4.3. Image of a TFB attached to a cooling plate on the side of the completed DS-ECal module. One can see that it is fully instrumented with 64 mini-coax cables that each are attached to an MPPC on the other side of the cooling plate. Each TFB has 4 “ports” each with 16 connection points for a total of 64 mini-coaxial cables per TFB, or 64 “channels”.

resolve and time-stamp signals at the few photo-electron (PE) level. Figure 4.4 shows schematically how the interface between the MPPC and TFB is achieved. Each TFB has 4 “ports” each with 16 connection points for a total of 64 mini-coaxial cables per TFB, or 64 “channels”. Each miniature coaxial cable connects a MPPC to the TFB. The high voltage (HV) bias is supplied on the core and the sheath carries a low voltage which can be adjusted in the range 0 to 5V, on an individual channel basis, to achieve the HV trim functionality. The MPPC signal is passively split between C_G, C_{HI} and C_{LO}, where a 10 to 1 ratio of C_{HI} to C_{LO} determines the high to low channel gain ratio. The value of C_G can be used to adjust the overall gain. For example, for a full-scale MPPC signal of 500 PE., C_G is chosen such that the low gain channel saturates at 500 PE.

4.3 DS-ECal Construction

The first ECal module constructed and integrated into the ND280 was the DS-ECal. The DS-ECal was a working prototype since the construction of the DS-ECal would serve as

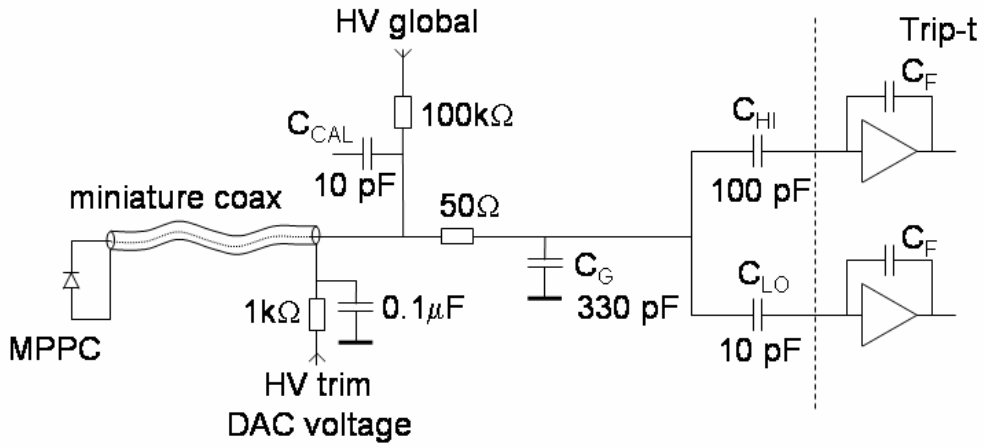

Fig. 4.4. Schematic of the MPPC/Trip-t interface showing the charge splitting between low and high gain channels.

a template for all other ECal modules to follow. The 13 ECal modules now have all been constructed by the T2KUK group utilising the experience acquired by the DS-ECal construction. The DS-ECal was built at Lancaster University as described in the following sections. The author of this work was responsible for carrying out and often supervising several phases of construction of the DS-ECal, the QA of the scintillator bars and the attenuation calibration of the system. The QA of the DS-ECal scintillator bars was also performed at Lancaster University and is addressed in Chapter 5.

4.3.1 Layer Build

Initially, a full-size prototype DS-ECal layer was built. It was discovered that many of the holes in the scintillator bars were blocked by Araldite glue which was used to secure the bars within the layer frame and to attach the lead to the bars. Subsequently, a smaller prototype DS-ECal layer was built which was constructed from shortened scintillator bars measuring 36 cm in length was called the Baby Prototype (BP) since it measured approximately one third of a full-size layer. The BP was built in order to test several methods that would be employed in the full-scale layer-building phase and to perfect the procedure of inserting the WLS fibres down the

central hole of the scintillator. To address the issue of blocked scintillator bar holes, an O-ring and push-bar mechanism was tested on the BP to keep glue out of the holes. It was important that all procedures were perfected in order to maintain the quality of the scintillator bar and WLS fibre.

One of the main issues that became apparent for building the layers was that the central hole of the scintillator bars was not circular as designed but rather was elliptical in shape. This is described in more detail in Section A.1. In short, maintaining a circular central hole was compromised during the extrusion of the scintillator bars due to the physical dimensions of the scintillator bar. As a result, when gluing the bars inside the layer frame araldite glue seeps into the central hole and blocks the hole thus preventing the insertion of a WLS fibre. To overcome this issue a set-up using O-rings was used. An O-ring here is a loop of elastomer with a disc-shaped cross-section. Four 2 m-long aluminium bars with a 1 cm^2 cross-section were positioned to make the square frame of the layer to ensure the layer alignment and rigidity. The machined aluminium bars have 2 mm-diameter holes at positions along their length aligned with the holes in the scintillator bars. A push bar system was employed to aid with securing the layer during the gluing process. This comprised of securing an aluminium 'push bar' along one frame end and screwing tapered locator pins through this, the frame and the scintillator bar holes. Locator pins were then pushed through the frame and the bar holes at the opposite end. The 'push bar' acts as a resistance to maintain the layer alignment and rigidity. The bars were cut to length such that there is a 1 mm gap between each bar end and the aluminium frame. The O-ring is 1.5 mm and placed in the gap and in front of the bar hole, with the locator pin through its central hole. Due to its elasticity the O-ring squashes but retains its circular shape, acting as a seal for the bar hole in order to eliminate araldite glue seeping through the bar hole.

Two lead sheets were glued side-by-side on top of the 50 secured bars, each lead sheet measuring 2 m x 1 m x 1.75 mm. Figure 4.5 shows the production of a layer at the moment that one such lead sheet has been glued to the layer and a second sheet is set to be attached. When

Fig. 4.5. Picture of a partially complete DS-ECal layer. One lead sheet has been glued to the scintillator bars. A second sheet is yet to be attached.

both lead sheets were glued to the bars and layer frame, the complete layer is covered with a sandwich of plastic sheet and fabric that are spread across the layer and secured taut. Vacuum pumps were then attached to evacuate air to minimise gaps and tolerances in the layers that may develop as the glue cures. Figure 4.6 depicts the curing process, where the complete layer is visible underneath the plastic sheets, fabric and vacuum pumps.

4.3.2 Module Build

The first component to be installed in the DS-ECal module was the LI system. The LI system is installed in two sections: Top and Bottom of the DS-ECal module. The bottom half was installed in the 1 cm gap that is between the outer perimeter of the first installed layer and the module bulkhead as shown pictorially in Figure 4.7. There are 4 strips x 10 LEDs along each side of the module for a total of 16 strips and 160 LEDs in each LI section (top and bottom), thus there are 32 strips in total that complete the DS-ECal LI system. There is one signal drive board for every two strips mounted on the inner wall of the bulkhead for the bottom LI strips and on the DS-ECal top plate for the top LI system. The power and signal cables from the drive boards

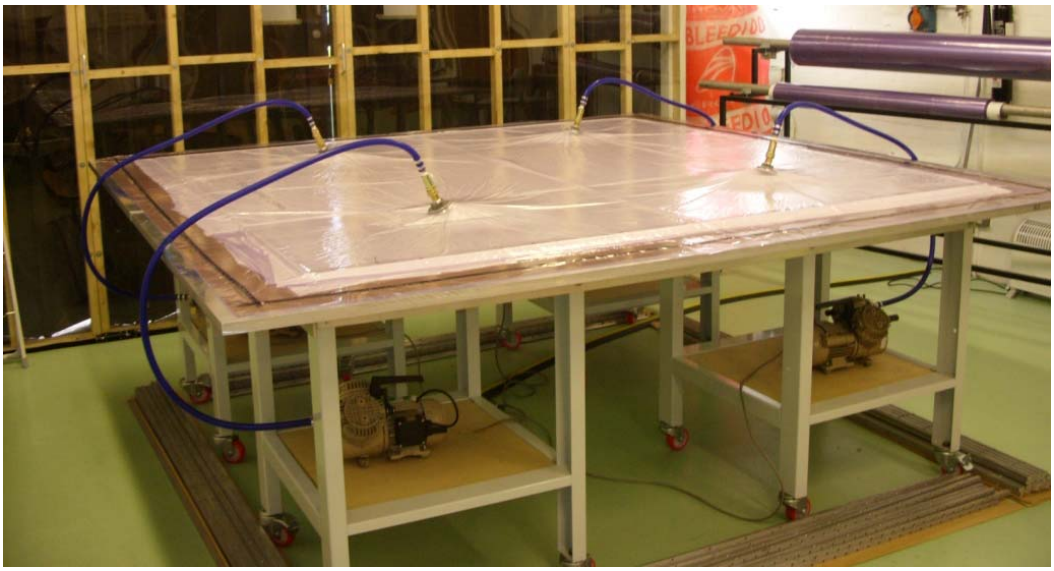

Fig. 4.6. Picture of the glue curing on a single DS-ECal layer. Air is evacuated from the layer with the application of vacuum pumps.

are fed out of the module through gas vents in the bulkhead. The drive boards and power cables are mounted on the bulkhead side, which doubles as a cooling plate due to space restrictions. Figure 4.8 shows the side and top view of one section of the installed LI system on the bottom half of the the DS-ECal module. The space restrictions are quite apparent.

The WLS fibres were inserted by hand through the bulkhead, across the 1 cm gap between the bulkhead and down the scintillator bar length and out again through the same configuration at the opposite end. The 1 cm gap between the layer frame and the bulkhead allows the fibres to be exposed to the LI system at both ends of the fibre. This process was completed with the aid of specially made tools that channeled the fibre from outside the bulkhead into the scintillator bar. This eliminated multiple insertion attempts, thus reducing the risk of damaging the end face of the fibre. It was most critical at this stage to preserve the integrity of the fibres since they had already been tested for quality and any damage could result in poor light transmission to the MPPCs. All measures during assembly were taken with signal quality in mind as the most important factor to maintain. The working environment was kept clean and fibres were handled with Nitrile gloves and wiped with KIMTECH precision wipes as they were inserted in order

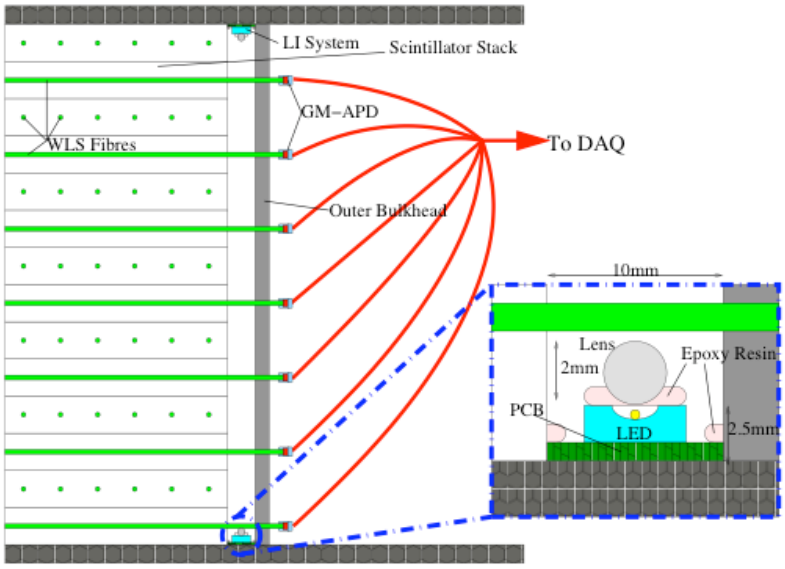

Fig. 4.7. Graphic describing the LI system location in the DS-ECal [68]. A zoomed view of the LI system at the bottom of the DS-ECal is on the right of the image. The LI comprises of a printed circuit board (PCB) strip with evenly spaced LEDs along its length. The solid green horizontal lines represent the WLS fibres along the length of the scintillator bars. A lens with a diameter of 2 mm is placed on the top of the LEDs along the strip, secured with epoxy resin. The lens increases the illumination of the fibres. GM-APD is another name for the MPPC sensors, as mentioned in Section 4.2.3.

to reduce introducing dust or other foreign objects into the scintillator bar cavity which might affect the coupling between the WLS fibres and scintillator.

Fibre Setting

Upon insertion of all 50 fibres for one layer, a small amount of silicon-based optical epoxy resin, which is a Saint-Gobain BC600 glue,

The glue was applied to the fibre in order to secure a ferrule, depicted in Figure 4.9, to the ends of each fibre. The ferrule couples the WLS fibre to the MPPC sensor. The MPPC sensor is housed within the setting tool and cushioned at the end of the setting tool by a foam spring that eases the connection of the MPPC to the ferrule. The MPPC legs that can be seen in Figure 4.9, and more closely in Figure 4.1, form the electrical contact with the PCB behind the setting tool. A mini-coaxial cable attaches to the PCB and takes the MPPC signal to the electronics.

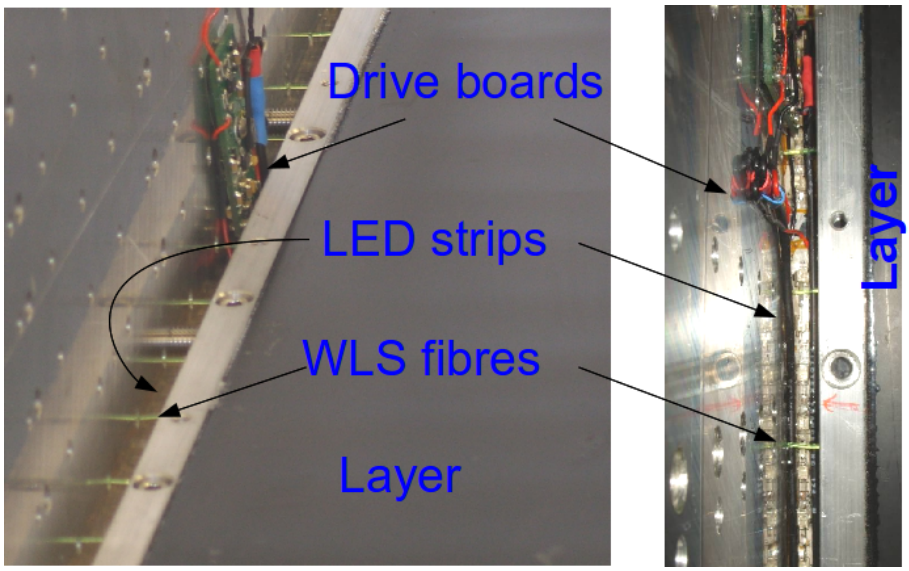

Fig. 4.8. The LI system is installed in the 1 cm gap between the first layer and the module bulkhead as seen from the side (left) and top (right). The WLS fibres pass through the bulkhead, over the LED strips and into the scintillator bar cavity.

The small cut-away seen on the side of the shroud is there to allow space to feed the mini-coaxial cable away from each sensor. The shroud houses all of the components in Figure 4.9 and slides over the ferrule, thus making contact between the fibre and MPPC. The shroud is attached to the module bulkhead by a screw through the hole visible on the left of the shroud in Figure 4.9.

Following the completion of each layer a 2D scan of the layer was performed using a source of ^{137}Cs that scanned along the length of each bar. This process is described in detail in the following Chapter 6. The scanning of the complete layers served as an integrity test of the fibre-to-MPPC coupling that was achieved as prescribed above.

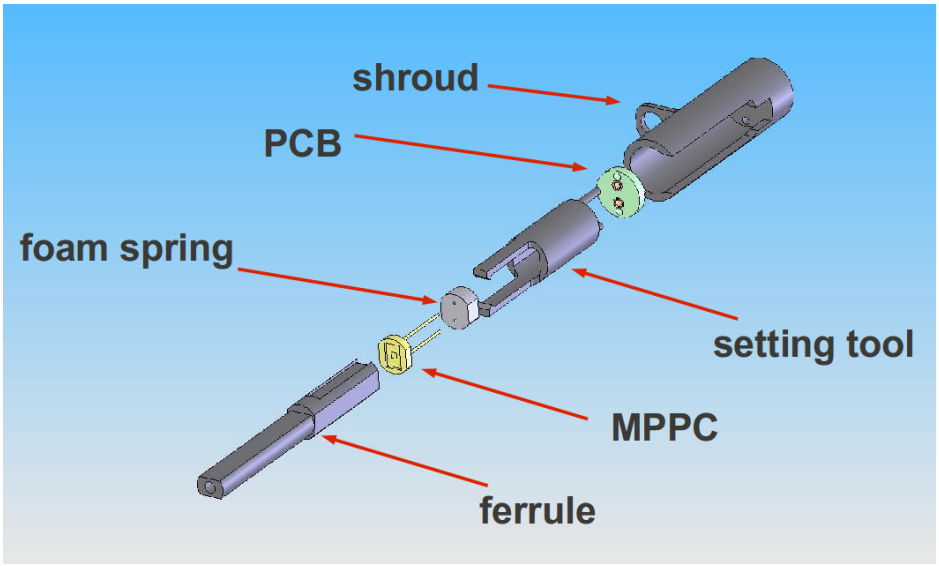

Fig. 4.9. The sensor-fibre connector. From left to right one can see the ferrule, sensor, foam spring, setting tool, printed circuit board (PCB) and shroud.

Chapter 5

Quality Assurance of Scintillator Bars for the DS-ECal

Optical quality assurance (QA) tests of the scintillator bars were needed firstly to ascertain that design specifications were met but also because there were no previous measurements of performance of the scintillator bars with WLS fibre from previous research and development for the combination of bars and fibre used in this case. Optical QA is described in Section 5.1.

After a layer was assembled there was no opportunity to replace any of the scintillators bars. It was therefore important to ensure that the bars were of good quality before they were glued into the DS-ECal layers. Mechanical QA was necessary to check that the required physical parameters of the bars conformed with tolerances. The analysis of the Mechanical QA results is described in detail in Appendix A.

5.1 Optical QA

The purpose of the Optical QA is to ensure consistency of the scintillator bar response to minimum-ionising particles (MIPs) and to ensure that the bars have a light yield greater than a threshold to be defined. In order to do this, a cosmic ray (CR) telescope was constructed. The composition of CRs is understood well. The CR flux inside the Optical QA lab consists almost exclusively of muons with energies of 2 GeV or greater (with a peak in energy of approximately 4 GeV) that interact as MIPs with the test scintillation material.

The QA system at Lancaster is made of three sections: the 2-m scintillator-bar photo-readout (Section 5.1.2), a triple-coincidence trigger for the CR telescope (Section 5.1.1) and the data acquisition (DAQ) system (Section 5.1.3).

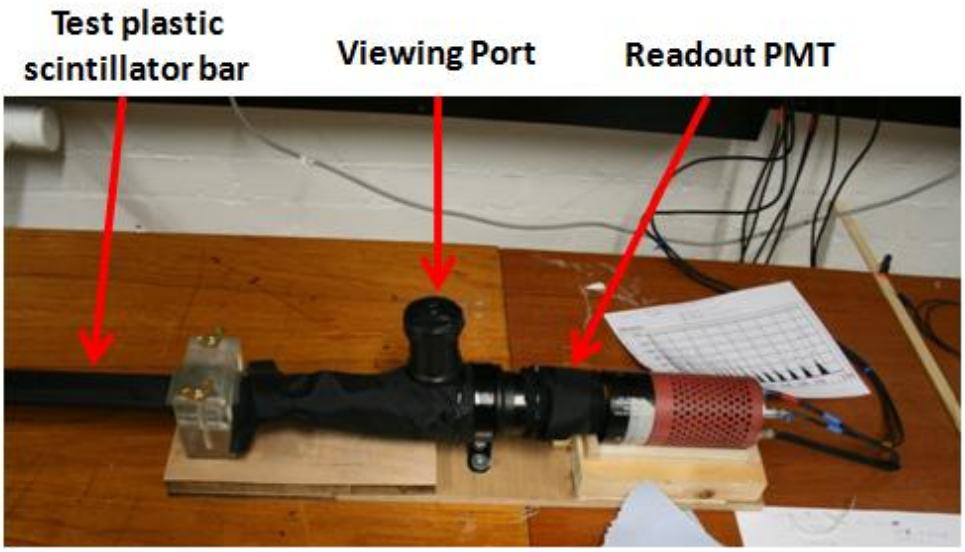

Fig. 5.1. The readout PMT coupled to the scintillator bar in testing within the light-tight setup.

5.1.1 Scintillator bar cosmic telescope

The CR telescope consists of three 4 cm x 6 cm scintillator pads each coupled to a 2-inch RCA8575 PMT biased to approximately 2 kV each. The coincidence trigger is arranged with one scintillator pad (Det. C) 3 cm above the test bar and the other two scintillator pads (Det. A and Det. B) 4 cm below the test bar which can be seen in Figure 5.2. This arrangement excluded showers and random coincidences from the PMTs and reduced the opening angle of CR to almost vertical muons thus eliminating the need for a correction of different path-lengths through the test bar due to different angles of incidence. Only 4 cm x 4 cm of the scintillator pads overlap, not all 4 cm x 6 cm. As a result, the active area of coincidence is 16 cm^2 and the telescope depth is 10 cm. It registered an average of 450 cosmic triggers per hour as expected from calculations. All three pads line up to create the trigger, although Det. C is rotated 45 degrees relative to Det. A and Det. B because the size of the PMT base does not allow it to be directly above the other two pads given the distance between them, but it still provides maximum angular acceptance of cosmic rays in this configuration.

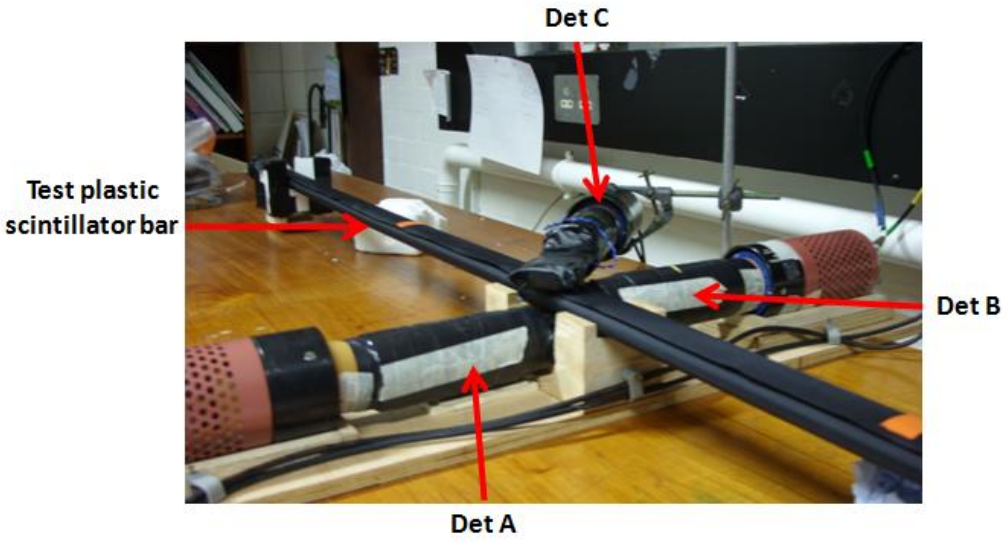

Fig. 5.2. The CR telescope setup showing the 2 m-long scintillator bar in light-tight microfibre sleeve and the triple coincidence trigger. The scintillator pad of Det. B is positioned above the pad of Det. A. Det. C is rotated 45°relative to Det. A and B.

5.1.2 Photo-readout of the Test Bar

Each bar to be tested for light yield first was wrapped in two layers of microfibre blackout-material as a form of a flexible dark box to achieve light-tightness. In order to obtain a robust signal over the background electronics noise, the light signal of the test scintillator was collected by three 1-mm diameter WLS fibres, rather than one, in the central hole of the scintillator bar. The three fibres were coupled to the centre of a 2-inch RCA8575 PMT (Photo-Multiplier Tube), with National Instruments NE586 optical grease. The optical grease is a clear, colourless, silicon-coupling compound to improve light transmission and bridge the gap for light signals between the two media: the WLS fibre and PMT. The PMT was biased at a voltage of 2.55 kV.

This bar readout end was confined in a series of plastic adaptors in order to enable easy replacement of bars for testing, and to ensure a consistent, reproducible optical coupling to the PMT. There was a viewing port to enable verification of the coupling of the WLS fibre to the PMT and to act as input for a LED-based light injection system that was used to calibrate the PMT with its single photo-electron peak. Figure 5.1 shows this arrangement. Optical light

yield tests were performed with the CR telescope positioned at a point approximately 66 cm (1/3 of the length of the bars) from the end of the bar. For the purpose of the QA, the factor measured was consistency of the light yield between bars and this was achieved by measuring the response to CR MIPs of each scintillator bar tested by the CR telescope. Figure 5.3 shows the end of the scintillator bar sticking out of the light-tight casing. The three WLS fibres that are used for readout can also be seen with Teflon tape wrapped as part of their coupling and alignment system to the PMT.

Fig. 5.3. Picture of the scintillator bar end with 3 WLS fibres for readout. Due to the elliptical shape of the hole it was possible to put 3 fibres down the central hole. The fibre ends are polished to an optical finish for coupling to the PMT. The fibres are held together with Teflon tape.

5.1.3 Data Acquisition (DAQ)

Output signals from the trigger detector PMTs were passed into a LeCroy 428F Linear Fan-In/Fan-Out module. Each signal was split into two outputs. One was passed to a Phillips Scientific PS711 Discriminator Unit and the second to the analogue input of a CAEN V695A Charge-to-Digital Converter (QDC) module. See Figure 5.4 for a schematic diagram of the electronics setup. Approximately 80 ns of delay was required on the signal to the QDC module in order to calibrate the timing between the triggers.

Signals from the discriminators were passed to the input of a PS755 Logic Unit acting as a coincidence. The signal from Det. C is passed through a 30 ns gate compared to 100 ns

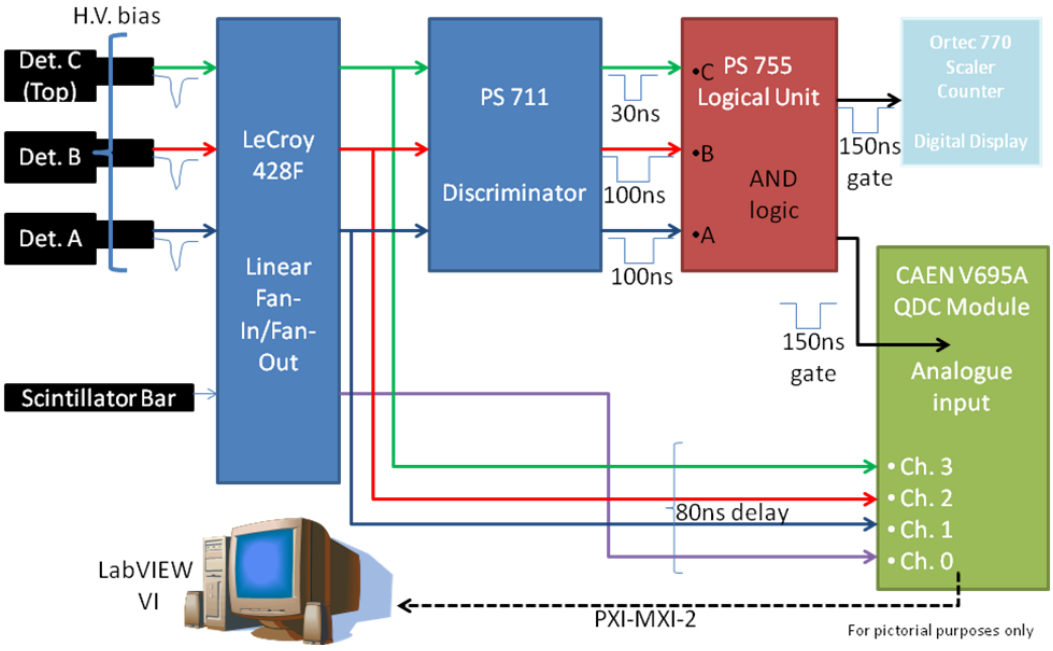

Fig. 5.4. Schematic overview of the electronics setup for data acquisition of the Lancaster QA cosmic telescope. Dets. A, B and C (left) act in coincidence to trigger a cosmic ray event. An electronics window of 150 ns is then opened to obtain data from the test scintillator bar.

gates for Det. A and Det. B so that it is Det. C that defines the timing of the coincidence and therefore the integration gate that is sent to the QDC module. If the coincidence gate for Det. C was large there would be a big overlap with the other two coincidence gates and we would not have sharp timing. The coincidence unit forms the logical AND at its output thereby producing the trigger for each cosmic ray event. Signals are determined coincident if they fall within a preset gate of 150 ns and are also recorded in the QDC module. The energy deposited by the cosmic rays to the trigger detectors is also collected for consistency checks. The QDC module was set in a VME crate controlled by a PXI-MXI-2 in a computer running LabVIEW 8. The DAQ software was built in-house and registers the charge integrals of input signals, places them into histograms and exports the data in a spreadsheet format that is read by the software package ROOT for offline analysis. An Ortec 770 Scalar Counter displayed a running total of coincident cosmic ray events on a digital display.

5.2 Optical Quality Assurance - Tests

After being wrapped as described in Section 5.1.2, a test scintillator bar is placed in the optical QA cosmic telescope. A single photoelectron (SPE) calibration of the readout PMT is performed using a blue LED flasher. The flasher is placed next to the readout PMT face, and was pulsed with very low light at about 1 kHz for approximately 30 seconds to obtain sufficient statistics of the SPE distribution of the PMT. This was measured before each cosmic ray run as it was found that the setup was sensitive to changing between bars as power had to be turned off to the PMTs to do so. The DAQ system gave a histogram of the SPE peak in terms of counts per ADC channel. This was then plotted in ROOT with the use of a script to convert the raw text file output into a .root readable file. A Gaussian distribution was fit to the SPE peak and the mean and error on the mean extracted. The pedestal mean was also measured so that it could be subtracted later. An example of the SPE peak with Gaussian fit is shown in Figure 5.5. The setup recorded 1000 cosmic ray events through a bar, which took approximately 2 hours.

In the same way, the cosmic ray signal distribution is recorded in terms of counts per ADC channel by the DAQ. A Gaussian fit is again applied and the cosmic ray mean and error were recorded as well as the pedestal mean. An example of the raw data from cosmic rays with a Gaussian fit is shown in Figure 5.6. With the determination of the SPE mean from a Gaussian fit, one can then determine a value for photoelectrons/MIP (PE/MIP) from a fit of the cosmic ray signal mean.

The SPE calibration is applied to the cosmic ray peak in the following way:

$$\text{PE/MIP} = \frac{\text{C}_{mean} - \text{C}_{ped}}{\text{SPE}_{mean} - \text{SPE}_{ped}}, \tag{5.1}$$

where

C_{mean} = mean of cosmic ray peak,

C_{ped} = mean of cosmic ray pedestal,

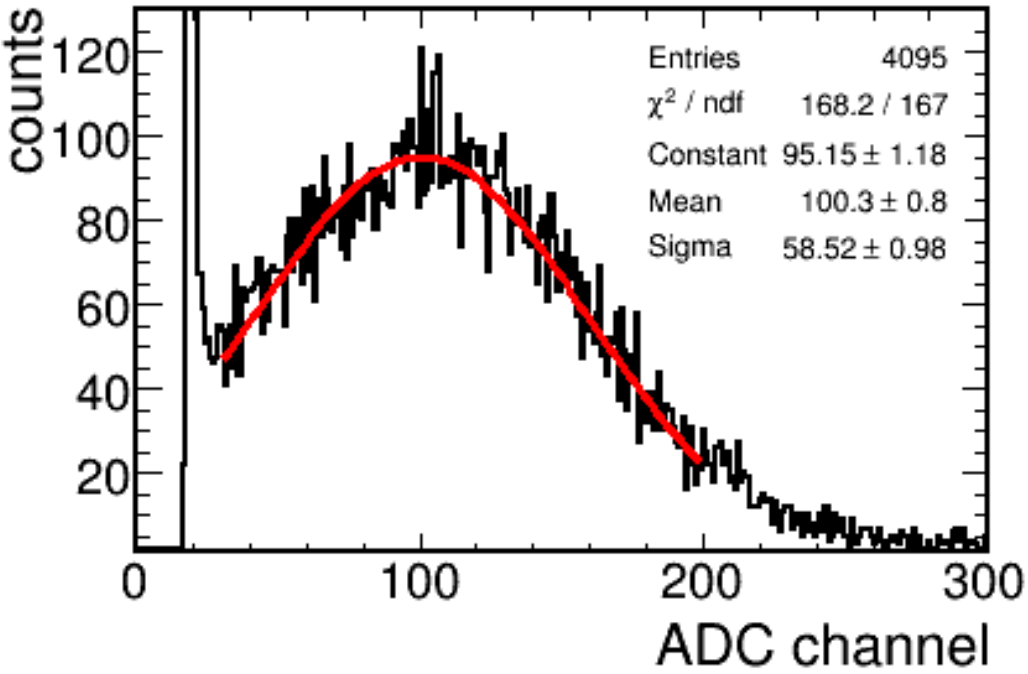

Fig. 5.5. Example distribution of the single photoelectron (SPE) calibration using a 1 kHz blue LED flasher, with counts versus ADC channel. The flasher is placed next to the readout PMT face, and flashed for 30 seconds to obtain an accurate measure of the SPE distribution. The pedestal can be seen on the left of the plot: here ADC channel 18.95 ± 0.05. The histogram is fit with a Gaussian distribution and obtains a typical SPE mean of 100.30 ± 0.80 ADC channels.

$\mathrm{SPE}_{\mathrm{mean}}$ = mean of single photoelectron peak,

$\mathrm{SPE}_{\mathrm{ped}}$ = mean of single photoelectron pedestal peak.

The pedestal mean is rebased to zero in the numerator of Eqn. 5.1. The uncertainty on the PE/MIP measurement is given by the expression

$$\sigma_{\mathrm{PE/MIP}} = \sqrt{\left(\frac{\sigma_{C_{mean}} + \sigma_{C_{ped}}}{C_{mean} - C_{ped}}\right)^2 + \left(\frac{\sigma_{\mathrm{chn/PE}}}{\mathrm{chn/PE}}\right)^2} * \mathrm{PE/MIP}, \tag{5.2}$$

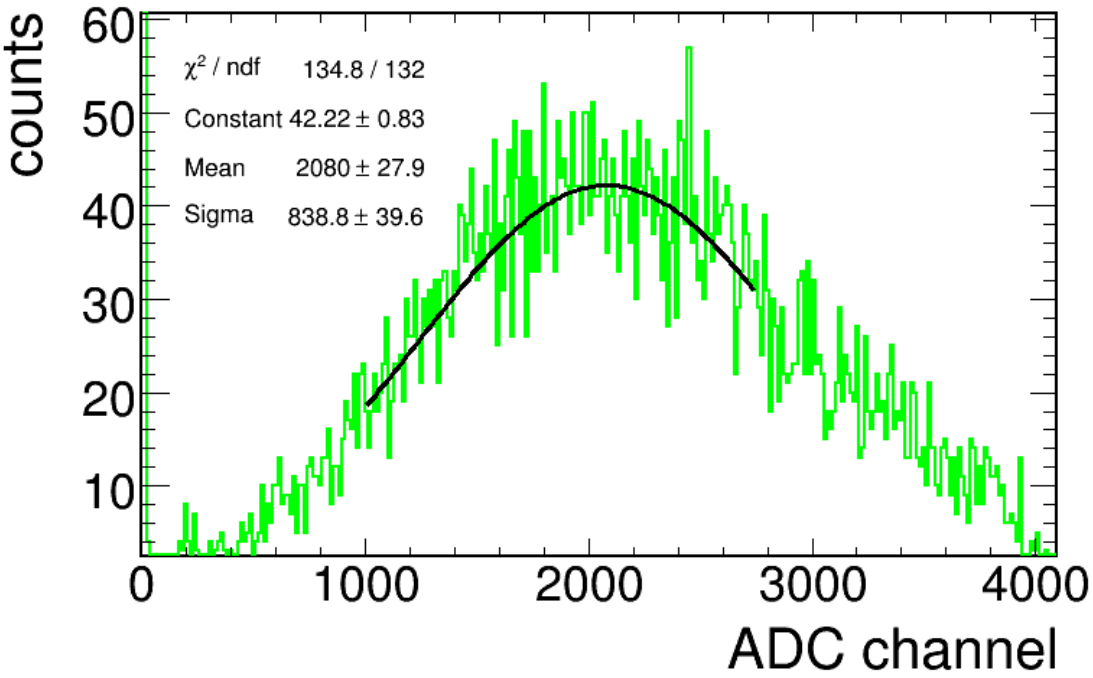

Fig. 5.6. A raw cosmic ray distribution with counts versus ADC channel. The pedestal can be seen on the far left of the plot. The histogram is fit with a Gaussian distribution which calculates a typical cosmic ray peak of 2080 ± 27.9 ADC channels. The fit range is chosen to minimise the chi-squared/ndf value.

where,

$\sigma_{\text{PE/MIP}}$ = error on calibrated PE/MIP value,

$\sigma_{C_{mean}}$ = error on mean of cosmic ray peak,

$\sigma_{C_{ped}}$ = ±2.00 ADC channels = error on mean of cosmic ray pedestal,

chn/PE = number of ADC channels per PE value,

$\sigma_{\text{chn/PE}}$ = error on ADC channels per PE value.

For this analysis, the pedestal position fluctuated with a spread of approximately ±2.00 ADC channels from run to run so a fixed error on the mean pedestal for SPE and cosmic ray runs of $\sigma_{C_{ped}} = \sigma_{\text{SPE}_{ped}}$ = ±2.00 ADC channels was used. The uncertainty on the number of

channels per PE value is given by the following expression to be used in Equation 5.2:

$$\frac{\sigma_{\text{chn/PE}}}{\text{chn/PE}} = \frac{\sqrt{\sigma^2_{\text{SPE}_{mean}} + \sigma^2_{\text{SPE}_{ped}}}}{\text{SPE}_{mean} - \text{SPE}_{ped}}, \tag{5.3}$$

and of course,

$\sigma_{\text{SPE}_{mean}}$ = error on mean of single photoelectron peak

$\sigma_{\text{SPE}_{ped}}$ = 2.00 ADC channels= error on mean of single photoelectron pedestal peak.

Figure 5.7 is an example distribution of a cosmic ray run after the SPE calibration has been applied to the data. The data has been rebinned and then fit with a Gaussian distribution in order to obtain a mean calibrated light yield in terms of PE/MIP.

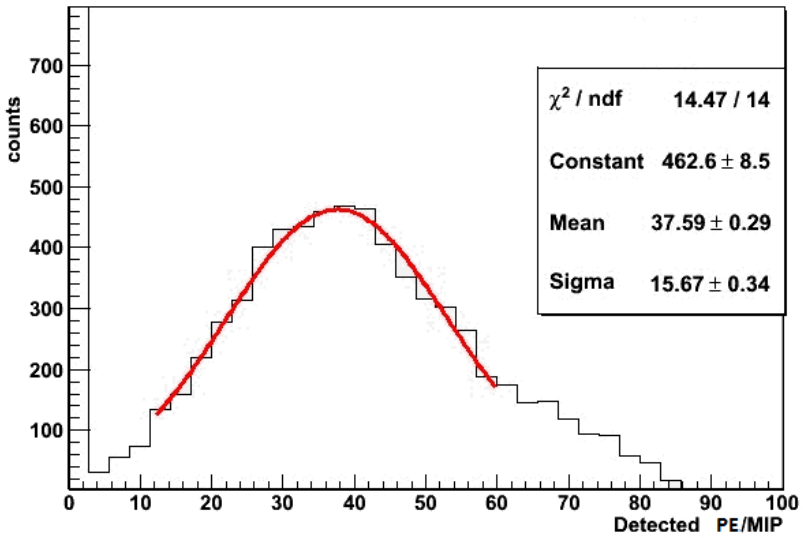

Fig. 5.7. A calibrated cosmic ray run distribution with calibrated energy in units of PE/MIP. This data has been rebinned and fit with a Gaussian distribution to obtain a mean calibrated light yield of 37.59 ± 0.29PE/MIP. Note that this is for a single bar with three-fibre readout onto the centre of a 2-inch PMT.

As a baseline we used a histogrammed distribution of the frequency of the detected PE/MIP values for 12 bars from the first batch of scintillator bars delivered, which we shall call Crate 1. The initial acceptance criteria was that the PE/MIP peak with this setup must fall within 2 standard deviations of the mean of the baseline from the Gaussian distribution fit. The baseline distribution is shown in Figure 5.8.

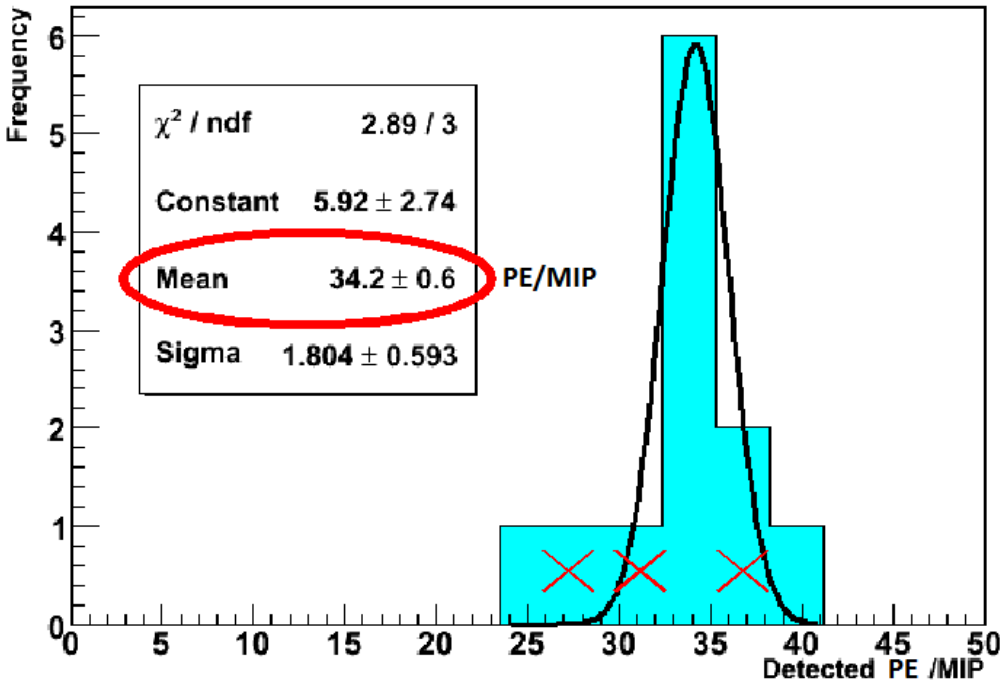

Fig. 5.8. Baseline frequency distribution of PE/MIP for 12 scintillator bars from Crate 1. This baseline has a mean, from a Gaussian fit, of 34.2 ± 0.6 PE/MIP. The minimum recorded value is 25.0 PE/MIP. This was decided to be used as a threshold value for subsequent Optical QA tests. Red crosses show PE/MIP values for 'yellow' bars.

Lancaster received an advance sample of four 1m length scintillator bars from the next production batch. The scintillator appeared unexpectedly yellow so there was a request to test these bars to compare with the baseline. The red crosses (-X-) on the histogram indicate these 'yellow' bars. They fall within the baseline, and within 2 standard deviations of the mean, thus any concerns about the optical properties of these bars were calmed. Subsequent bars that were

tested were checked with this baseline in the same way. The baseline distribution has a mean of 34.2 ± 0.6 PE/MIP for the 12 bars sampled and a standard deviation, σ, of 1.80 ± 0.59 PE/MIP. A 2σ acceptance would set a lower limit of 30 PE/MIP; however, it was agreed that the lowest recorded PE/MIP (25) from the 12 tested bars was acceptable and would be a threshold. A caveat was that if anything was recorded lower than this value we would halt production and sample more bars, especially those that were made in the same production run of any bar below the threshold PE/MIP set by the baseline, and we would reassess the baseline method.

In total 73 out of 1700 bars were optically QA'd, of which three were placed into the first layer built, corresponding to Layer 34 of the DS-ECal, and 2 in all subsequent layers. Figure 5.9 shows the distribution of detected PE/MIP for all optically QA'd scintillator bars versus bar ID. It can clearly be seen that all bars detected a PE/MIP value above the set threshold of 25.00 PE/MIP. The average is 36.57 ± 3.71 PE/MIP where the error is an average of all errors.

Figure 5.10 has a more accurate measure of the mean detected PE/MIP. It displays the frequency distribution of the calibrated detected PE/MIPs for all optically QA'd bars with a Gaussian fit of the data. The fit measures a mean PE/MIP of 35.9 ± 4.9 PE/MIP, remembering that this is not an absolute measure of the PE/MIP of the bars since it was measured with three-fibre readout. It can be seen that all results fall within $\sim 2\sigma$ of this value, which is acceptable for passing the optical QA. The mean of 35.9 ± 4.9 PE/MIP from the Gaussian fit is consistent with the value of 36.6 ± 3.7 PE/MIP taken simply from the average values.

Subsequently, all bars that were selected for optical QA tests were accepted for use in the DS-ECal construction. As these were randomly chosen from the total set of bars, it was assumed that all bars had acceptable optical properties for the DS-ECal and no bars were rejected due to the optical QA. This gave us the confidence to recommend the reduction of the percentage of optically QA'd bars for the subsequent ECal modules constructed in the UK. By reducing the procedures and freeing up manpower we increased the construction speeds.

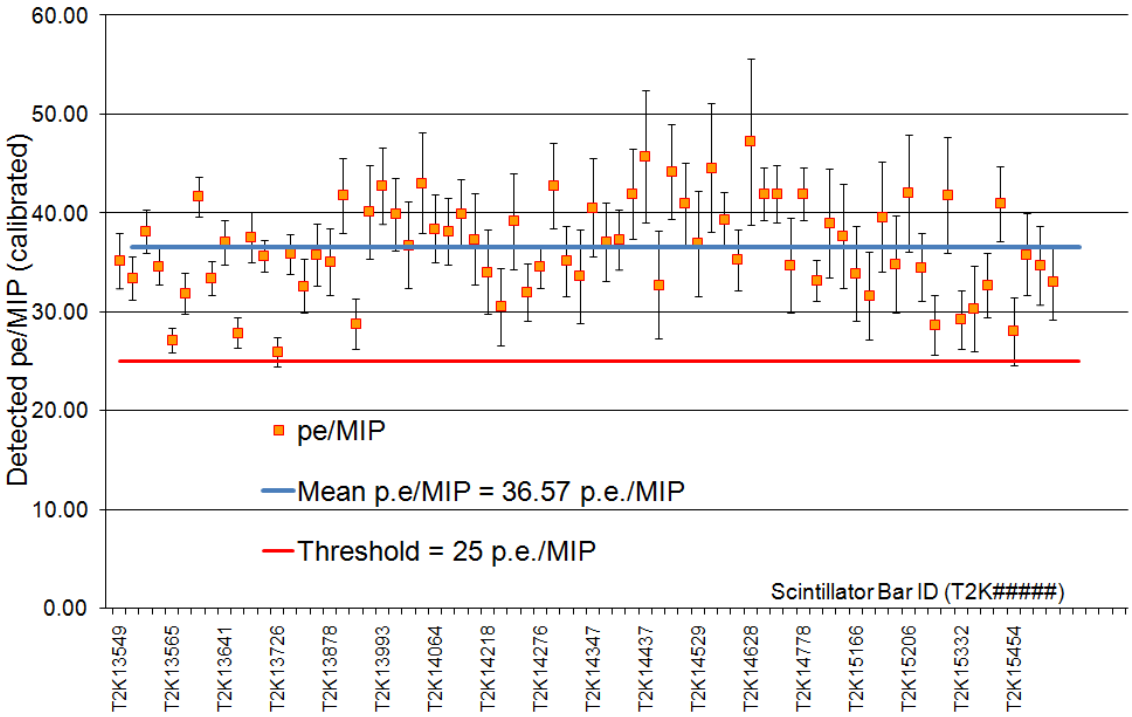

Fig. 5.9. Detected PE/MIP for all optically QA'd scintillator bars versus scintillator bar ID. The red line shows the threshold decided from the baseline studies. The blue line is the mean light yield of 36.57 ± 3.71 PE/MIP from a total of 73 out of 1700 bars, with three-WLS fibre readout.

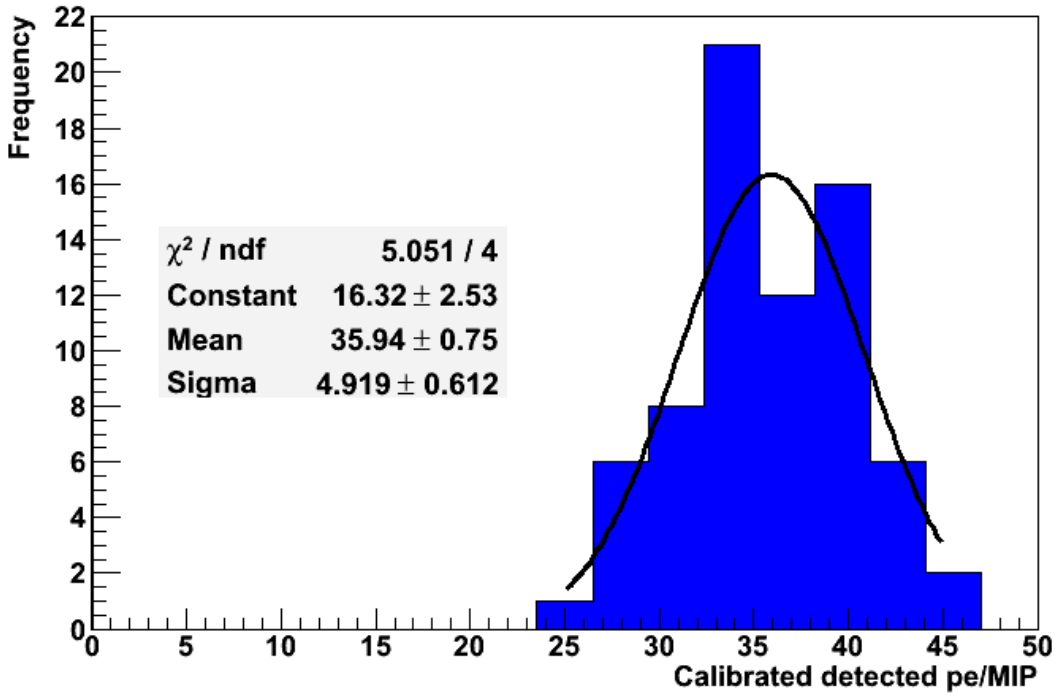

Fig. 5.10. Frequency distribution of the calibrated light yield PE/MIP for all optically QA'd scintillator bars. The distribution has been fit with a Gaussian to obtain a mean light yield of 35.94 ± 4.92 PE/MIP. Note that this uses three-fibre readout at 66 cm along the bar.

Chapter 6

The 2D Scanner

During the DS-ECal module construction, a 2-dimensional (2D) scan with a radiation source was performed on each bar of a layer as soon as the layer was inserted into the module and instrumented with WLS fibres. The radiation source was a ^{137}Cs 3 mCi (111 MBq) source in a quasi-insoluble and non-leachable anti-abrasive form, sealed inside a stainless steel capsule with a 0.8 mm window thickness. The source was acquired from Canberra.

The 2D scanning of the assembled layers required 100 MPPCs, 2 sides of 50 sensors each, for readout of the double-ended bars of a single layer. The primary scope of the scans was the integrity of the channels once a layer was secured inside the DS-ECal module. We used the same MPPCs to scan each layer, one layer per day. This required the connecting and reconnecting of the sensors on a regular basis which is in contrast to the one-time connection of production sensors that remain on the module for its lifetime.

The integrity of each of the completed layers of the DS-ECal was monitored using a 2D scanner designed at Queen Mary University of London. The 2D scanner was used to characterise the attenuation of light along each bar of each layer during construction of the DS-ECal module. This allowed us to find any structural defects on the bars or fibres so that they could be replaced or repaired before continuing with the module construction. The scans were the first quantitative check of the entire bar-fibre-ferrule assembly. The same specification MPPC sensors and TFBs were used as for the full deployment of the DS-ECal, so it also served as the first field test of the complete sensor-electronics readout system.

For the 2D scans, each sensor was attached to the WLS fibre and connected to the TFB for electronics readout. On the completion of the scan the sensors were disconnected and put aside ready to repeat the process for the next layer. There are many points throughout this process that

are sources of possible damage to the sensors and the mini-coaxial cables that attach them to the TFB. This could lead to an impractical level of sensor failure rates and, more importantly, could limit the reproducibility of the 2D scans, preventing useful comparisons between the output from different layers. A safe handling of the sensors and mini-coax cables was paramount to the quality of the 2D scans and something we successfully achieved with the development of a mounting bracket.

6.1 Readout and Data Acquisition

The data acquisition (DAQ) system employed for the 2D scans acted as a 'Vertical Slice' of the DAQ for the entire ECal subsystem because its requirements were scaled down to only read out 100 channels per scan as opposed to the full scale 3400 channel capacity of the DS-ECal or the 22366 channels of the complete ECal subsystem.

Each layer of the DS-ECal has double-ended readout; hence, to scan one layer required photo-readout of the WLS fibres at each end of the scintillator bars which meant that two TFBs, one each readout side of the layer, were mounted on the MPPC mounting brackets and 1 m-long mini-coax cables from each of the 50 MPPC sensors were attached to 50 of the 64 channels of the TFB on each side of the layer.

We refer to the TFBs on the opposing sides as TFB0 and TFB1 for reference. Figure 6.1 shows the described setup, on one side of the DS-ECal module, with the sensors attached to the TFB via the 1 m-long mini-coax cables and the TFB mounted on the MPPC mounting bracket. To the left in the picture is the power cable and to the right is the communication cable that takes the electronics signal to the RMM via an Optical Gigabit Ethernet cable.

The RMM data flow was controlled by a desktop PC via an Intel PRO/1000MF Server Adapter and MIDAS backend DAQ software. We refer to this as the DAQ-PC. The MIDAS DAQ read the high and low gain channel output and provided slow control of the individual

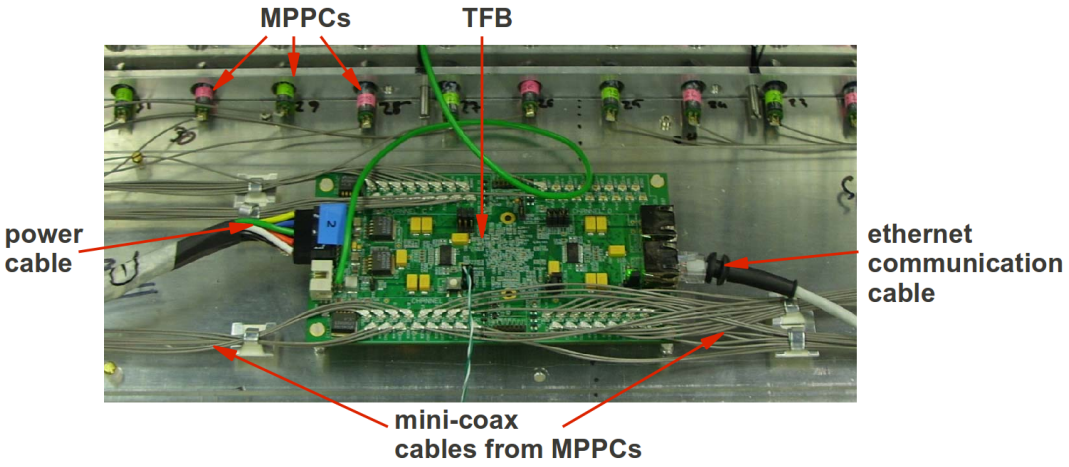

Fig. 6.1. The MPPC mounting bracket. The MPPCs (top of picture) are attached to the WLS fibres and mounted on the bracket. The signal from the MPPCs is carried along a 1 m-long mini-coax cable to the TFB (centre of picture). The TFB power cable goes off to the left and the ethernet communication cable, to the right, takes the electronics signal to an RMM. The entire mounting bracket is 2 m long and holds 50 MPPCs, of which 10 are visible in the picture.

MPPC voltage. *In – situ*, the MPPC voltages can be adjusted by the MIDAS DAQ. All of the 2D scanner data was exported from MIDAS file types to ROOT format for data analysis.

Another feature of the 2D scanner setup was that the complete DS-ECal module was made to be light-tight with a combination of custom-made blackout material sheets covering the module, in particular the sensor readout regions. This was needed to effectively eliminate external light that would illuminate the exposed section of fibres in the 1 cm gap between the first layer and the module bulkhead as shown in Figure 4.8 in Section 4.3.2 and give a varying background contribution. Any potential light leaks appeared in the analysis of the background scan (see Section 6.1.1). Light leaks were addressed prior to the 2D scan of a layer. Figure 6.2 is a picture of the DS-ECal module draped in the blackout material to achieve the required light-tight condition. The horizontal arm above the centre of the layer is the scanner arm. The vertical arm attached to it holds the source, visible just above the surface of the layer.

The 2D scanner's movable arms that carried the radiation source were controlled by a LabVIEW control program on the Scanner Control desktop PC (SC-PC). When the SC-PC

Fig. 6.2. The DS-ECal module is being scanned. The DS-ECal is made light-tight by a complete blackout material coverage. The horizontal arm above the centre of the layer is the scanner arm. The vertical arm attached to it holds the source, visible just above the surface of the layer. One can clearly see where tape is deployed to secure the blackout material.

activated the scanner, the scanner arm lifted the radiation source out of the source holder and located a zero position that was common for every scan. It then found the top of the layer using proximity sensors, lifted up 14 mm above the layer and moved to the first scan location along the first scintillator bar. The SC-PC opened a TCP/IP [8] connection to the DAQ-PC and sent a "GO" command which sent the position of the source and requested an event from the RMM. The RMM then triggered the TFBs with 5000 triggers at a rate of 90 Hz. The TFBs take care of the individual Trip-t operation such as sequencing the Trip-t analogue pipeline readout and digitisation of the signal, as well as formatting and transmitting data back to the RMM. The RMM then transmits the data back to the PC. There are a total of 23 x 250 ns integration cycles per event which results in 23 histograms storing the signal spectra for each channel. A single

[8]TCP: Transmission Control Protocol, IP: Internet Protocol. There are two original components of the Internet Protocol Suite referred to together as TCP/IP

channel refers to one MPPC attached to a TFB so for complete readout of one layer there are 100 (channels) x 23 (integration cycles) = 2300 signal spectra. The 2D scanner data was collected using only the information stored in the high gain ADC channel readout of the MPPC as this was deemed sufficient without needing to use the low gain channel ADC information. At the time, no range switching was present which is required in order to correlate the relation between the high and low gain channels and it was difficult to distinguish the SPE peak from the pedestal in the low gain range. The PE peaks were sufficiently separated in the high gain range in order to define the MPPC gain.

The 2D Scanner collected data at 20 points along each bar (30 points in the case of layer 34). Data points are closer together at the ends of the bars in order to accurately measure the distance at which the light signal drops significantly as a result of light escaping the bar ends. The first data point was 2 cm from the end of the bar which was determined by the size of the source holder. Five points were then scanned, 5 cm apart, and then the scanner moved 14 cm consecutively to measure 5 further points, moving 15 cm to the next point and then a further 5 points 14 cm apart before finally measuring the last 4 points 5 cm apart for a complete scan schedule of 20 points at 2, 7, 12, 17, 22, 36, 50, 64, 78, 92, 107, 121, 135, 149, 163, 178, 183, 188, 193 and 198 cm from the end of the bar.

The analysing software ran parallel to data-taking when the scanner was scanning each bar. This occurred overnight to produce attenuation plots of each bar in order that we could make a decision on the QA of each bar and complete the layer in the morning before the insertion of the next layer of the module. A complete layer was analysed by sending 50 jobs (scan data for each bar in a single layer) distributed on 13 nodes of the Lancaster network, taking approximately 3 hours to complete.

6.1.1 Background (B) Scans

Before running the 2D scan schedule, a background scan of the MPPCs was recorded. The background scan was taken without the presence of the source over any of the scintillator bars and was a measure of the noise of the MPPCs, which is the dark current, and the electronic pedestal. The dark noise is defined as the rate that electrons accumulate in each pixel of the MPPC due to thermal action. This rate depends directly on temperature and the impurities in each pixel. Figure 4.1 previously showed a close-up of the pixels of the MPPC in Section 4.2.3.

Figure 6.3 is an example of the background (noise) spectrum for one MPPC, recorded in one of the 23 integration cycles during the scanning of one point along a bar, the first integration cycle in this case. The high gain channel ADC values are shown on the abscissa. The pedestal peak at approximately ADC channel = 155 and the first three PE peaks are well defined. Each peak corresponds to a number of photons, for example the second peak corresponds to 1 photon, termed the single photo-electron peak (SPE), the third peak corresponds to 2 photons, etc. The triangles are markers of peaks found using a standard peak-fitter algorithm. The position of the peaks are used as seed values for the parameters to make the global fit which is shown as the solid line on the plot. The global fit is only set to fit for the first four peaks because the value of interest here is the gain which is given by the separation between the pedestal peak and the SPE peak. The pedestal is assumed to be the highest peak in the noise spectrum. We take the root mean square (RMS) of the pedestal ADC value and fit to a Gaussian the peak in the range ±3 x RMS of peak in order to find the pedestal mean ADC value. The gain and pedestal mean are used later on to calibrate the spectra as described in Equation 6.2. Figure 6.4 shows a 2D histogram mapping of the pedestal mean ADC value for each integration cycle across all channels read out by TFB0. There is a similar map for channels read out of TFB1. Three distinct regions can be seen in Figure 6.4. This is because the TFB has 4 separate “ports” each reading out 16 channels which was illustrated earier in Figure 4.3. The first port read out the first 16 channels, the second port read out channels 16-31, the third port read out channels 32-47. The final two channels were

read out by the fourth port. The pedestal mean varies by approximately 10-15 ADC port-to-port but is consistent channel-to-channel within a TFB port.

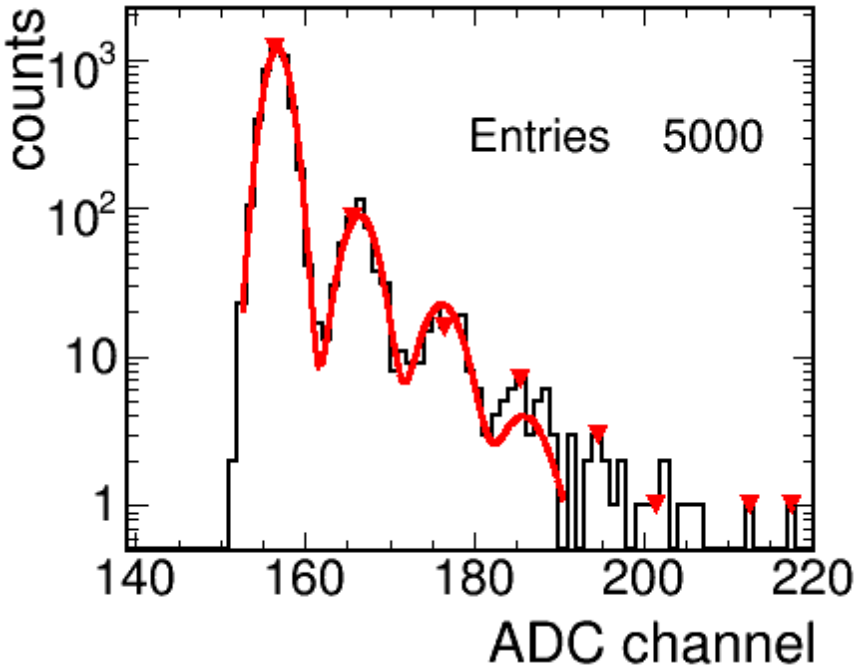

Fig. 6.3. Typical background signal from 2D scanner data. In particular this is taken from TFB0, Layer 22, Bar 35 (MPPC channels are labeled in the software from 0 - 49, corresponding to Bars 1 - 50 respectively). This is the integrated background signal recorded in the first integration gate (labeled 0). The fit comes from the TSpectrum method in ROOT and the triangle markers attempt to find peaks. Only the first four peaks are included in the fit range.

Figure 6.5 shows the total charge from the background data summed over the 23 integration cycles for one MPPC. This is a typical summed spectrum of the background across all MPPCs. The pedestal peak value of the summed background spectrum from the 23 integration cycles is normalised. This normalisation is performed for each cycle added to the sum by setting an offset in the following way:

$$\text{offset} = \text{pedestal peak mean } (ADC) - 100\text{ADC} \tag{6.1}$$

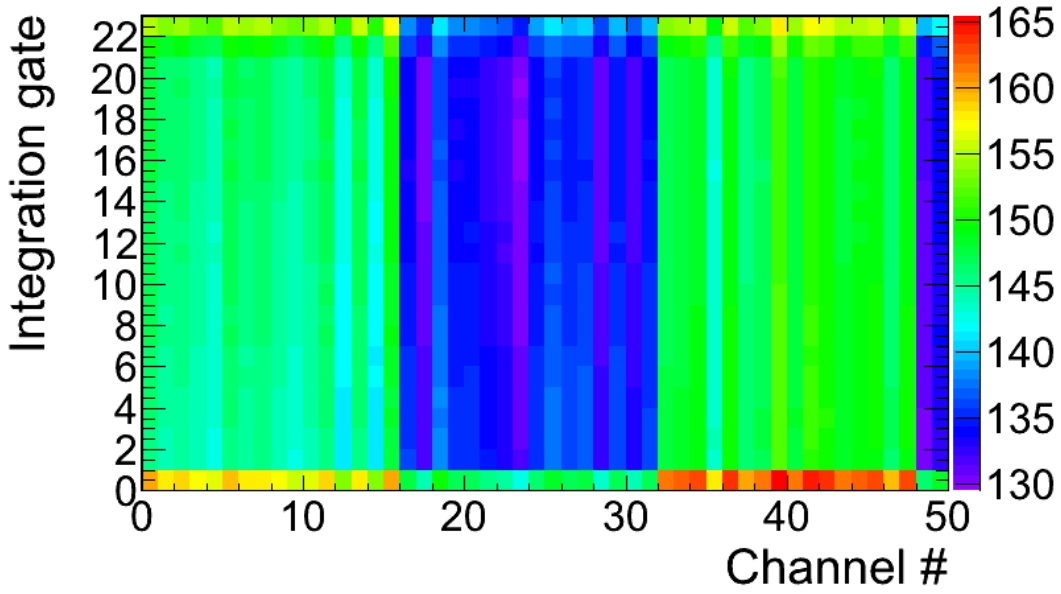

Fig. 6.4. Typical 2D histogram map of pedestal mean ADC values of each integration cycle across all readout channels of a TFB mounted on one side of a layer that is being scanned.

The next step was to calibrate the background spectra for the summed high gain channel charge signal for each MPPC sensor. Figure 6.6 shows the calibrated background spectrum for the signal in Figure 6.5. The calibration of the arbitrary ADC values into PE values is done so that the background spectrum for each channel relates to the next. In order to calibrate the spectrum we use the conversion

$$\mathrm{N}_{PE} = \frac{\text{ADC value} - \text{pedestal mean}}{\text{gain}} \tag{6.2}$$

where $\mathrm{N_{PE}}$ is the number of photoelectrons. This results in the calibrated spectrum correctly beginning at 0 pe, corresponding to the pedestal, and subsequent peaks being equivalent to increasing integer PE values as shown in Figure 6.6. The global fit and peak finders are also calculated and shown for the users' benefit for online monitoring. Once the background scan

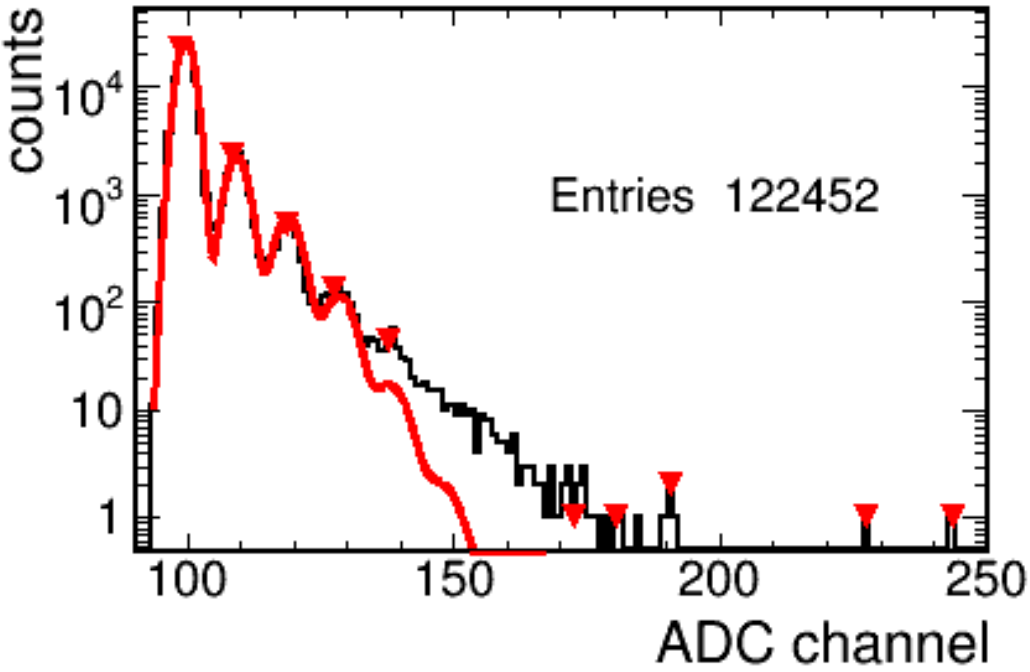

Fig. 6.5. Typical MPPC noise spectrum from 2D scanner data. This is the total background signal summed across all 23 integration cycles in the Trip-t readout pipeline, plotted on a log scale. The fit comes from the TSpectrum method in ROOT and the triangle markers attempt to find peaks; successful only for the first few peaks that are prominent.

was complete a check was performed to verify the status of each channel. These plots served as a means to identify and debug any sensors not responding, and we could also identify any light leaks in the system from these histograms.

6.1.2 Source (S) Scans

Once a successful background scan of all 100 channels of a single layer was collected, the 2D scanner was instructed to start a scan with the ^{137}Cs source. The scanner arm moved across the layer, stopping at the predetermined 20 points along each scintillator bar. For each point at which the scanner stopped, the same data acquisition process that collected the background signal was repeated. The TFBs received 5000 triggers at a rate of 90 Hz for each point and the signal collected by the MPPCs was read out to produce equivalent ADC value charge spectra

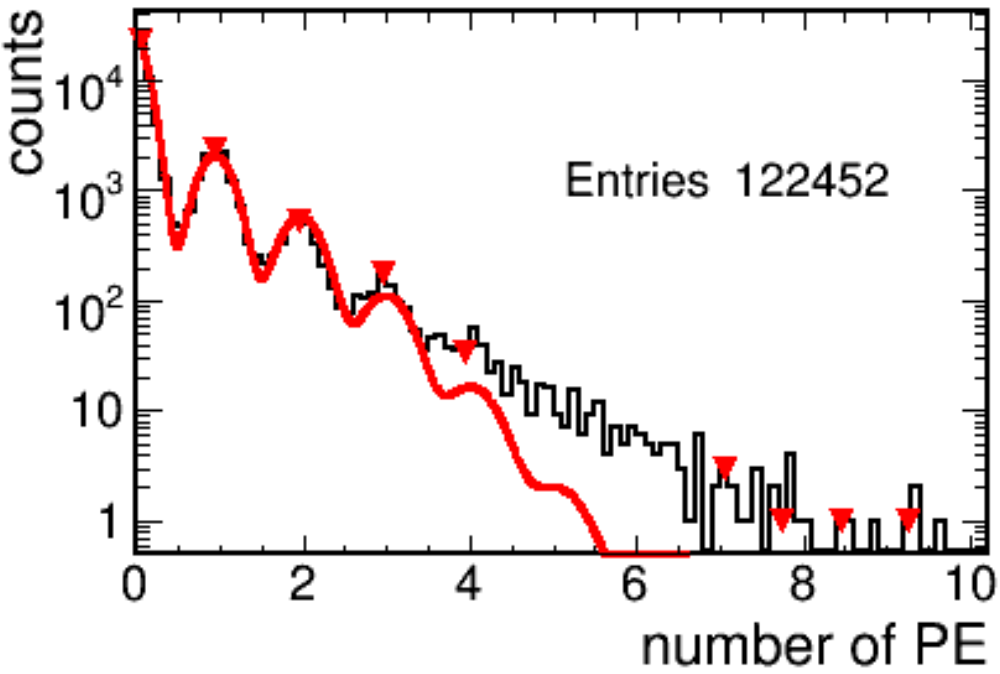

Fig. 6.6. Typical calibrated background signal from 2D scanner data. In particular this is taken from TFB0, Layer 22, Bar 35. This is the calibrated, total background signal for the MPPC sensor on one end of the bar, plotted on a log scale.

for each of the 23 integration cycles. The source spectra from one integration cycle is shown in Figure 6.7. The background signal from Figure 6.3 is also shown in Figure 6.7 for comparison. The summed source spectra, normalised to ADC channel 100, from one MPPC readout is shown in Figure 6.8. The corresponding summed background signal from Figure 6.5 is also shown. One can see a slight offset between the source and background signals in Figure 6.7 and when looking at the signals from one integration cycle it is difficult to resolve the source signal from the background. Once one looks at the source signal summed across all integration cycles the source and background signals can be distinguished beyond the second PE peak.

As expected, the single cycle and summed source spectra in Figures 6.7 and 6.8 are populated with greater charge in the tails of the distributions than the corresponding background spectra. More peaks could be found in the source spectra by the peak finder. This relates to

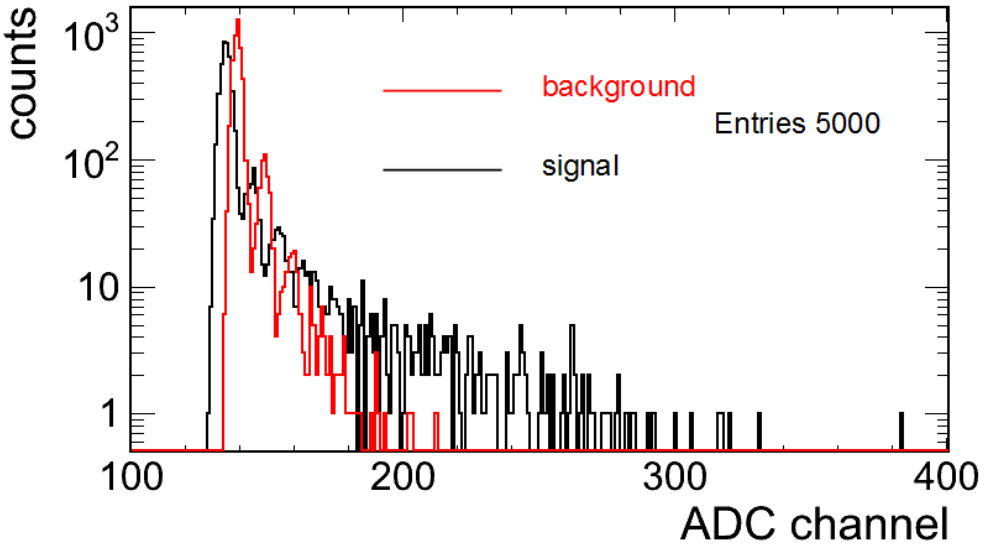

Fig. 6.7. Typical source signal (black) from 2D scanner data plotted versus the background (red) signal. The background signal is the same that was shown in Figure 6.3. In particular this was recorded by TFB0, Layer 22 and Bar 35. This is the integrated source signal recorded in the first integration gate (labeled 0), plotted on a log scale.

the fact that the MPPC sensors are firing more pixels as they are receiving more light from the WLS fibre. The radiation source emits a collimated beam of approximately 667 keV photons. The scintillator bar absorbs the energy of the traversing photons via ionisation and re-emits this absorbed energy in the form of photons. The WLS fibre collects the photons produced by the scintillator bar and transports them to the MPPCs which produce the source signal. The pedestal and gain of the spectra are calculated in the same manner as for the background spectra to produce an equivalent calibrated source signal spectrum for each channel summed over the integration cycles, as shown in Figure 6.9.

Figure 6.10 is the typical source signal from two MPPCs in the presence of the ^{137}Cs radiation source. The MPPC signals are from opposing ends of one bar and the histograms are from each scanning point along the bar. The source is closest to TFB0 (blue) in the top left histogram, moving along the bar (reading histograms from left-to-right) until it is closest to signal from TFB1 (red) in the bottom right histogram. One can see the point at which the source

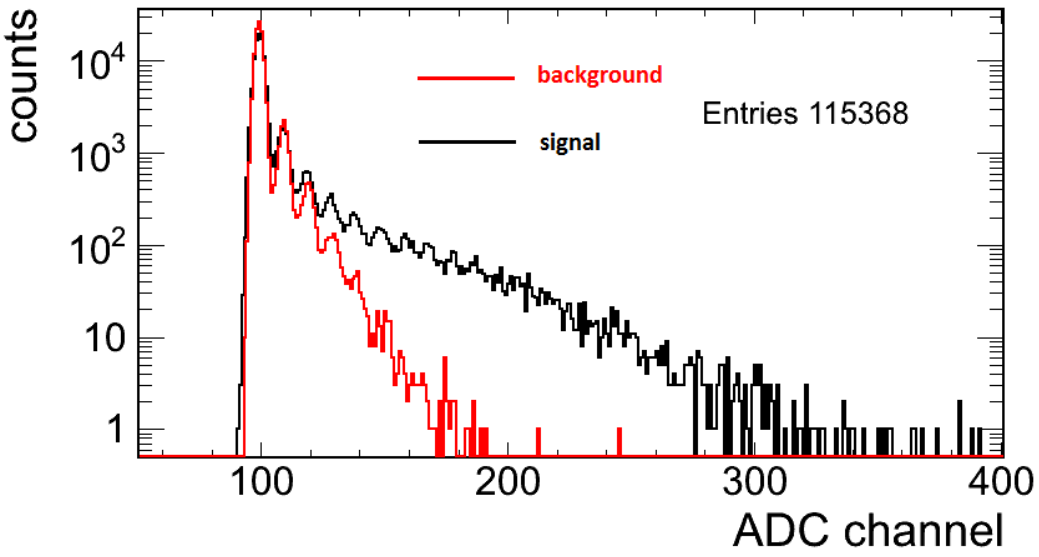

Fig. 6.8. Typical summed source signal (black) from 2D scanner data versus the summed background (red) signal. The summed background signal is the same that was shown in Figure 6.5. In particular this was recorded by TFB0, Layer 22 and Bar 35. This is the integrated source signal summed across all 23 integration cycles in the Trip-t readout pipeline for a single sensor, plotted on a logarithmic scale and normalised to ADC channel 100.

is above the middle of the bar because the signals from the two MPPCs are indistinguishable at that point.

6.1.3 2D Scanner Attenuation Profiles

Attenuation is a measure of the reduction of light as it travels along the WLS fibre. The data collected from the background readings and the scans of the bars with a source, combined with the position of each source signal data point, result in the ability to produce attenuation profiles for each bar in each layer of the DS-ECal. For simplicity we refer to the source data as S. It is in truth, the source signal + background since the background signal is ever present. The background data is referred to as B. The attenuation profiles depict the frequency of S/B as a function of position of the source along the bar, as measured from the MPPC sensor. The S/B amplitude ($A_{S/B}$) is calculated by integrating the calibrated S and B data over the range 5.5 pe to 30 pe and dividing as in Equation 6.3.

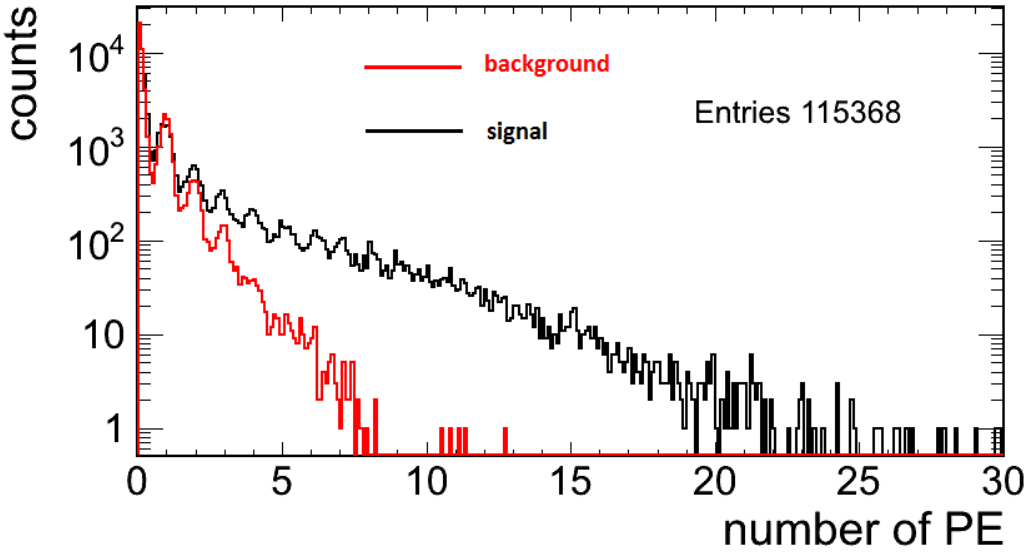

Fig. 6.9. Typical calibrated source (black) versus background (red)signal from 2D scanner data. In particular this is taken from TFB0, Layer 22, Bar 35. This is the calibrated, integrated source signal for the MPPC sensor on one end of the bar, plotted on a log scale. The calibrated background signal is the same distribution that was shown previously in Figure 6.6.

$$A_{S/B} = \frac{\int_{5.5}^{30.0} S}{\int_{5.5}^{30.0} B} \tag{6.3}$$

$$\sigma_{A_{S/B}} = A_{S/B} \sqrt{\left(\frac{\sigma_{\int_{5.5}^{30.0} S}}{\int_{5.5}^{30.0} S}\right)^2 + \left(\frac{\sigma_{\int_{5.5}^{30.0} B}}{\int_{5.5}^{30.0} B}\right)^2}. \tag{6.4}$$

The error on the resultant attenuation amplitude is calculated using Equation 6.4. Figure 6.9 shows the typical calibrated B and S dataset distributions. The data is integrated above 5.5 PE because the source signal is dominated by background data below this region. One can see that the background is reduced significantly at 5.5 PE. The corresponding amplitude of the S/B is plotted as a function of distance along the 2 m bar to produce attenuation profiles from the signal of the MPPCs at either end of the bar typical of the profiles shown in Figure 6.11.

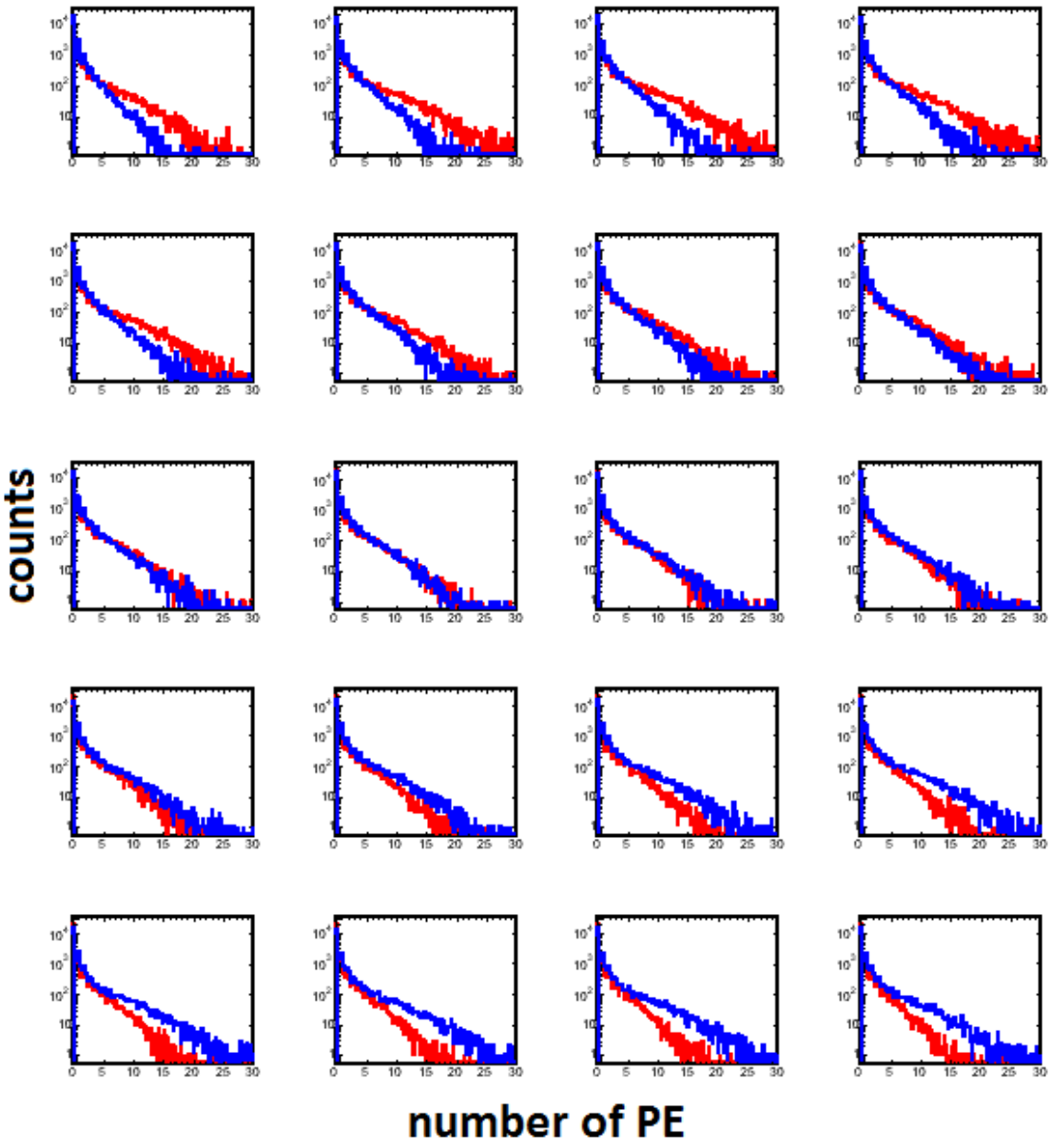

Fig. 6.10. Typical signal from two MPPCs in the presence of the ^{137}Cs radiation source. The MPPCs signal are from opposing ends of one bar and the histograms are from each scanning point along the bar. Blue signal is TFB0 signal and red is TFB1 signal readout of the same bar. The source is closest to TFB0 in the top left histogram, moving along the bar (reading histograms from left-to-right) until it is closest to signal from TFB1 in the bottom right histogram.

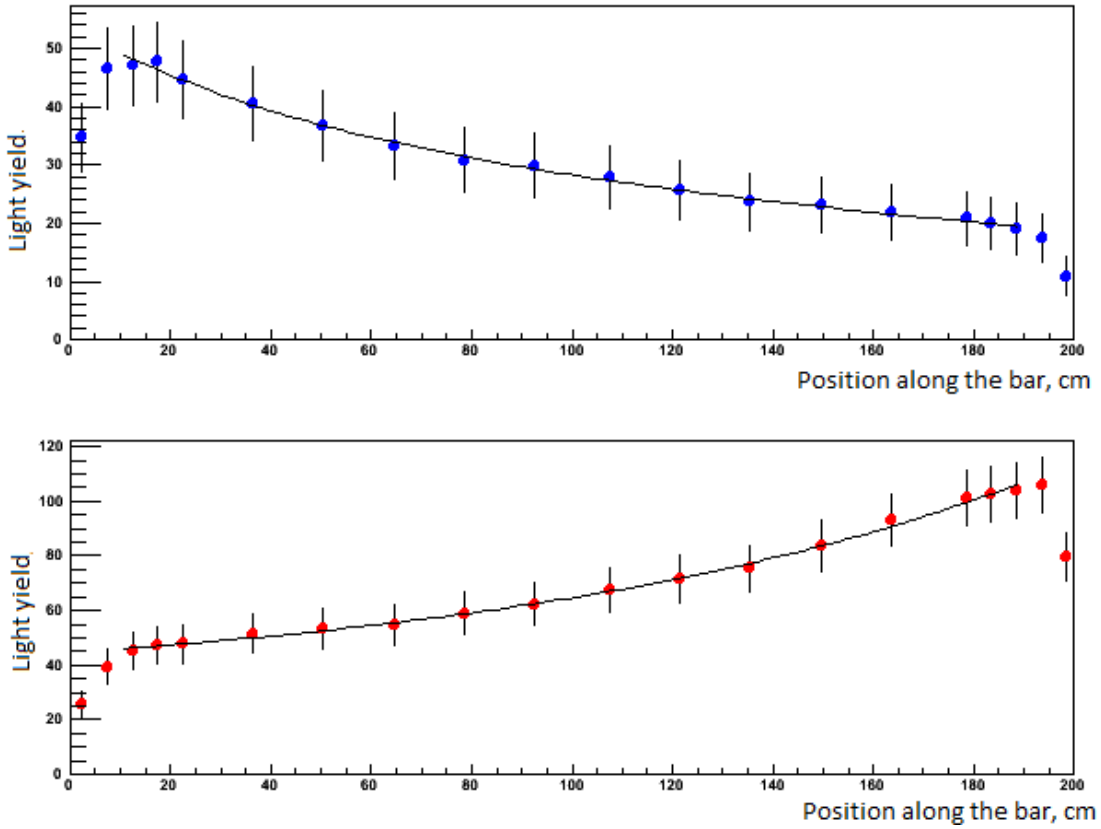

Fig. 6.11. Attenuation profile of Bar 35 in Layer 22, produced with signal from the ^{137}Cs source with the 2D scanner with readout from an MPPC on TFB0 (top, blue) and TFB1 (bottom, red). The attenuation amplitude is a reference value in pe since it is calculated as a ratio of the integrals of S/B.

These profiles have a clean, well-defined shape and no discernible features and hence pass the integrity test. The attenuation can be expressed as a sum of two exponential distributions (a double exponential function) with a coupling constant. According to [69], the two exponential distributions represent the self-absorption that is exhibited by all compounds that have wavelength-shifting fluors (the WLS fibre), and the bulk attenuation processes due to geometrical optical factors. The self-absorption in the WLS fibres accounts for fluctuations in light intensity at fibre ends so this is referred to as the short attenuation length component. The bulk processes are referred to as the long attenuation length component. The double exponential function described by Equation 6.5 is fit to the data.

$$A(x) = P_0 \left[exp\left(\frac{x}{P_1}\right) + P_2 * exp\left(\frac{x}{P_3}\right)\right], \tag{6.5}$$

where x is the distance between the radiation source and the MPPC readout, and the function parameters P_i (i = 0,1,2,3) are defined as

- A(x) = attenuation at distance x
- P_0 = constant
- P_1 = short attenuation length (cm) = pS
- P_2 = coupling constant (ratio) between the long and short attenuation lengths.
- P_3 = long attenuation length (cm) = pL

Examining the profiles in Figure 6.11 more closely, you can see how the light drops off at the fibre ends furthest from the source for each profile. This can be attributed to light escaping the fibre ends. The light also drops off at the ends where the MPPC is closest to the source and this is a combination of light escaping the fibre ends without registering signal on the MPPC and also due to the self-absorption effect of the WLS fibres leading to the short attenuation length component. I refer to these near and far effects at the scintillator bar ends as '*end effects*'.

Figure 6.12 is an example of one channel that failed the integrity test and shows the power of producing the attenuation profiles. The profile for TFB0 shows a very low attenuation amplitude that implies that the source signal is not larger than the background and also does not have the characteristic double exponential shape as the data points fluctuate randomly along the length of the bar. This is a feature that results from either a poor MPPC connection to the WLS

or a damaged fibre. In this case, the fibre was replaced, the MPPC was re-connected and the scan repeated for that particular bar.

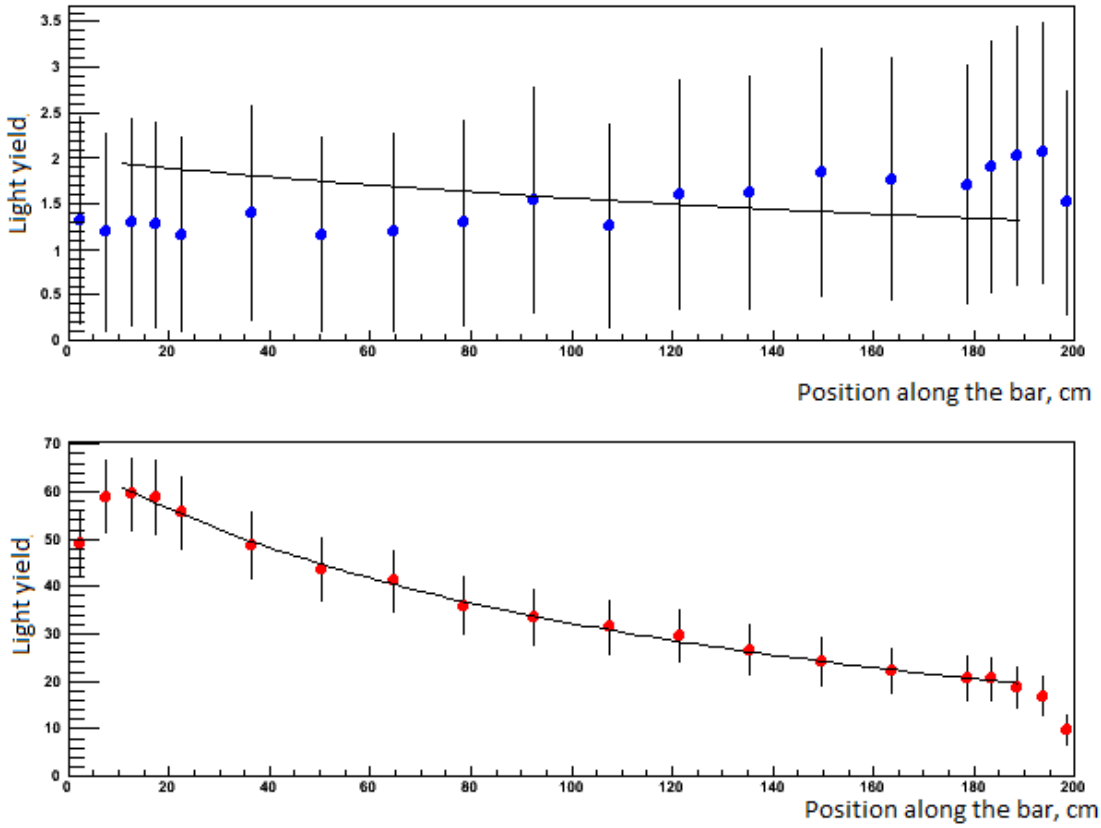

Fig. 6.12. Attenuation profile from an MPPC that fails the integrity test, produced with signal from the ^{137}Cs source with the 2D scanner. Profiles are from an MPPC on TFB0 (top, blue) and TFB1 (bottom, red). The TFB0 profile highlights a potentially damaged channel that needs to be replaced.

The primary purpose of the 2D scanner was to monitor the integrity of each completed layer of the DS-ECal during the construction of the complete module. The scans were done daily therefore a fast analysis was required in order to verify that a layer was successfully installed without any damage caused to the WLS fibres inserted in the bars of the layer. An attenuation profile was measured using the ratio of the signal and background (noise) spectra recorded by the MPPC sensors. Only high gain charge information was required in order to produce an attenuation profile from a sensor at each end of a bar. The profiles allowed for fast scanning of

the data to find damaged fibres or poor fibre installations so that fibres could be replaced before installing a new layer. Since the attenuation profiles measured a relative light yield we looked for self-consistency of the scans for each layer. We replaced the most fibres during the installation of the first 6 layers as we were still improving our installation techniques. We replaced 12 fibres during the installation of the first 6 layers and only 7 fibres from the final 29 layers for a combined total of 19 replaced fibres. We did not have to replace any fibres that were themselves replacements. A further highlight of the success of the 2D scanning procedure was that only 11 channels out of 3400 were deemed 'dead' for the complete DS-ECal upon installation in the ND280 pit in Tokai. This setup successfully instrumented the detector and proved to be an invaluable experience because it was also the first vertical slice of the complete DS-ECal readout chain.

Chapter 7

CERN Test-beam

The calorimeter uses MPPCs, a relatively new type of photosensor as mentioned in Section 4.2.3. Due to their novel nature they require different calibration techniques than those commonly used in detectors using PMTs. A testbeam run was crucial to the understanding of the calibration procedure for this readout before the detector was positioned within the basket of the ND280 detector suite in Tokai and, more importantly, offered the only opportunity before installation to measure the absolute electromagnetic and hadronic energy scale.

Once the DS-ECal module was completed it spent a period of 3 months at Rutherford Appleton Laboratory collecting limited cosmic ray data as it underwent initial commissioning and electronics integration tests. The DS-ECal was then transported to the East Hall area at CERN to undergo beam tests. Importantly for the work in this thesis, here the DS-ECal collected cosmic ray data which provided a sample of muons for commissioning and calibration of the final DS-ECal module system before proceeding to Tokai for integration into the ND280. The attenuation correction study in Chapter 8 made use of the large CR data-set collected with the DS-ECal during time at CERN.

In addition to calibration work, the testbeam provided a library of data on hadronic and electromagnetic shower profiles at energies below 1 GeV, the peak energy region for neutrino interactions due to the off-axis configuration of the experiment as described in Section 3. It is well known that Monte Carlo models do not model neutrino interactions well in this energy region, therefore testbeam data is useful in tuning the understanding of these interactions and also in testing software reconstruction and particle identification techniques using real rather than

simulated data. The testbeam provided a final and only chance to test, debug and operate the entire DS-ECal system, including the hardware, data acquisition and detector control subsystems, under standard operating conditions before installation in the ND280 detector in Japan.

7.1 DS-ECal Setup at CERN

The completed DS-ECal detector was commissioned for the first time in CERNs East Experimental Area, specifically in the T9 beamline. The 24 GeV PS proton source at CERN collided protons with a solid target which produced showers of secondary particles. The secondary particles with momenta from 300 MeV up to 5 GeV were guided along the T9 beamline to the experimental area where the DS-ECal was situated. The momentum of the particles at the focal point in the beam area was determined by the electrical currents passed through the guiding magnets in the beamline, as stipulated in [70]. I participated both in the data-taking and data analysis at CERN.

The process of adjusting the currents on the guiding magnets was one aspect of shift work during commissioning at CERN in order to acquire the desired momenta of particles. The intensity of the beam was controlled by adjusting the current through the focusing magnets. By switching the direction of current through the bending magnets, the polarity of the particles guided along T9 could be reversed. Consequently the DS-ECal collected data in both positive and negative polarity modes thus providing a library of data consisting primarily of electrons and pions in negative mode and positrons, protons and pions, and a small contribution of kaons and deuterons, in positive mode. Reference [70] predicts the composition of the beam. Further to this, a study was completed that measured the beam composition for the opposing polarity beam configurations shown in Figure 7.1 [71].

Figure 7.2 shows the DS-ECal and its positioning in the testbeam environment at CERN. A pair of Cherenkov counters were provided by CERN as part of the setup and they were useful for particle identification (PID), notably for electrons. Two scintillator paddles, approximately 8

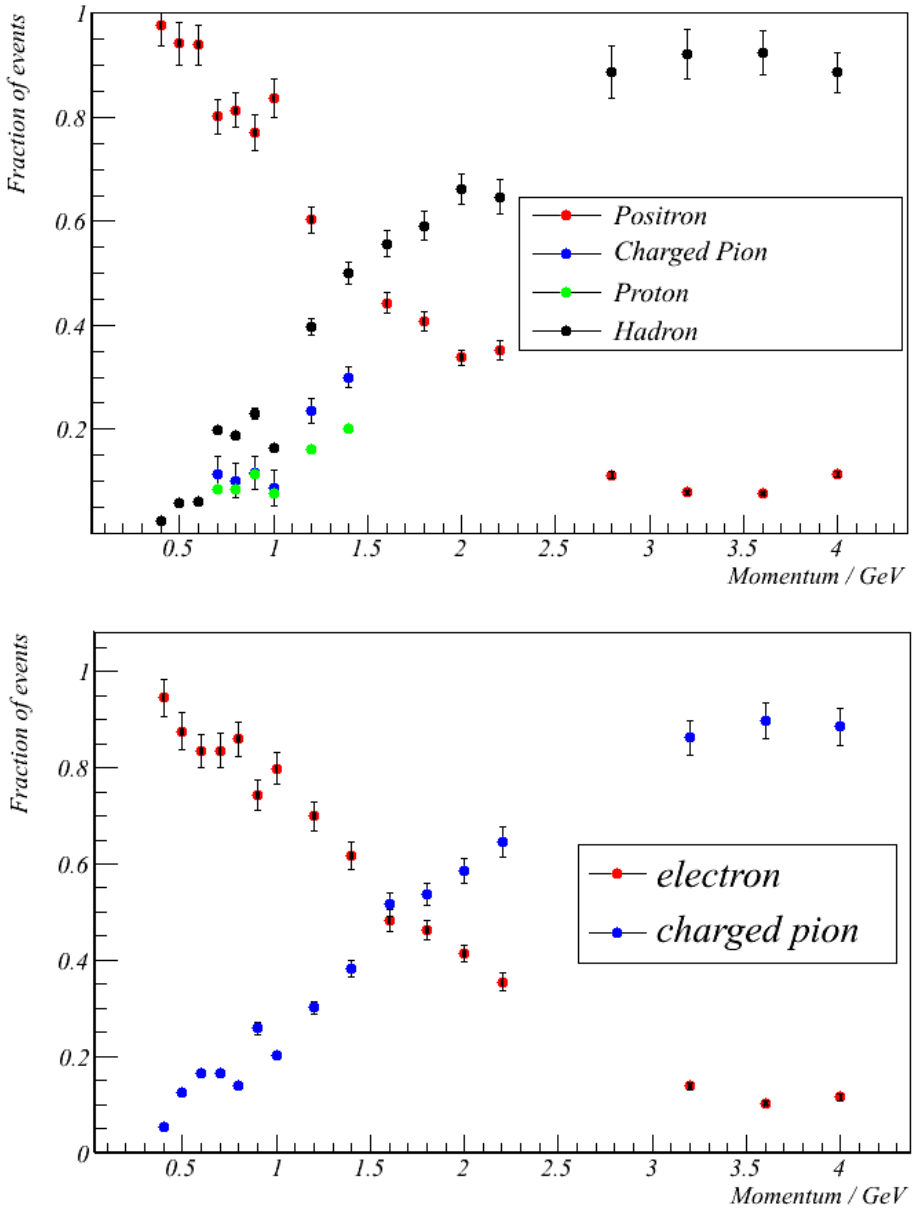

Fig. 7.1. Measured beam composition in the CERN T9 testbeam in positive (top) and negative (bottom) polarity modes. Error bars include systematic and statistical error estimates [71].

cm x 12 cm, formed a Time-Of-Flight (TOF) detector that could identify heavier particles below the Cherenkov threshold. When the DS-ECal was at normal incidence to the beam, as in Figure 7.2, the downstream TOF paddle was a few centimetres from the DS-ECal, separated by 14 m from the upstream TOF which was situated in a 4 cm gap in the beamline. The module also was rotated about the vertical axis to provide data-taking opportunities when the beam was not

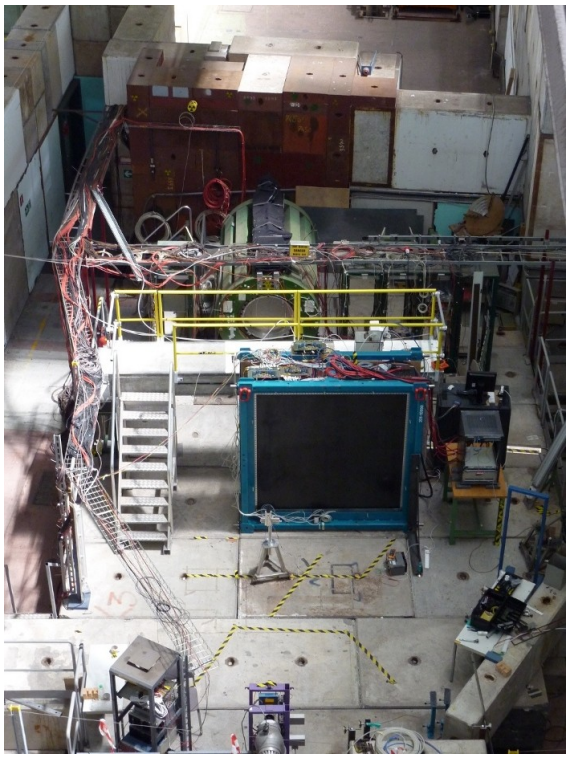

Fig. 7.2. A picture of the DS-ECal at normal incidence to the T9 beam. The downstream TOF paddle can also be seen.

normal to the detector. It was also translated along the horizontal axis to provide off-centre data. The separation of the TOFs was reduced when the DS-ECal was rotated as the downstream TOF was moved further upstream.

During six weeks of running the DS-ECal registered approximately $2x10^6$ triggers (cosmic ray and beam) between 300 MeV and 4 GeV, collecting data at varying angles to the beam. Table 7.1 records the different testbeam configurations.

After the completion of data taking in the CERN T9 testbeam, the detector was laid down so that it faced downwards (layer 34 was on top). I shall refer to this orientation as the DS-ECal being in the '*flat*' position. During the testbeam the DS-ECal was upright in the position that it sits in the ND280 basket. Figure 7.3 shows the orientation of the DS-ECal in the '*flat*' position in relation to the upright position and the test beam direction. Cosmic muon data was collected whilst the DS-ECal was '*flat*'.

Position	Angle (degrees)	Triggers
central	0	620 000
off-centre	0	150 000
centre	15	50 000
centre	30	720 000
centre	60	510 000
centre	75	80 000

Table 7.1. Approximate number of triggers achieved in the T9 testbeam in six weeks.

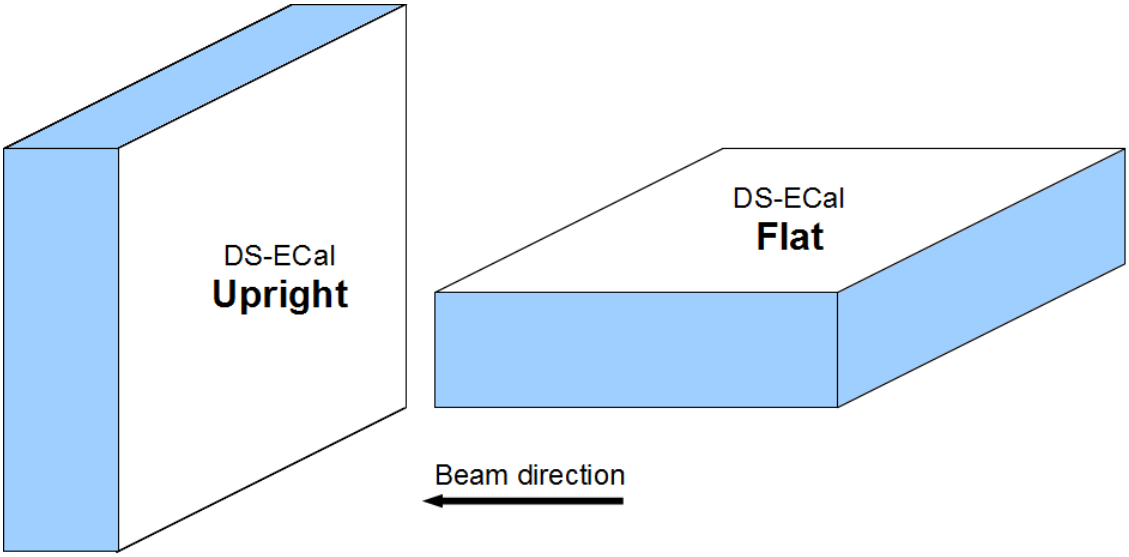

Fig. 7.3. Pictorial representation of the DS-ECal position configurations during the CERN T9 testbeam. The DS-ECal is shown in the upright postion (left) for which the testbeam data was collected. The DS-ECal sits upright in the ND280 basket. Also shown is the DS-ECal laid '*flat*'. Cosmic muon data was collected in the '*flat*' position.

7.2 Commissioning Work

7.2.1 Hit Maps

Cosmic ray hit density distributions, referred to as "hit maps", were produced in order to identify, in the first instance, the extent of the DS-ECal's functionality. A "hit" is a measured energy deposit in the detector. The hit maps can identify quickly any channels that are not operating optimally. The hit maps were produced from cosmic ray data. These data were

collected during beam downtime and the extended run after testbeam. The cosmic data files are first converted from raw MIDAS data format to ROOT-readable "unpacked" data files by the ND280 software and then analysed within the ECal reconstruction package. Figure 7.4 shows an event display of a typical cosmic ray event as reconstructed with the *eventDisplay* program. The *eventDisplay* program utilises the Event Visualisation Environment (EVE) [72] of the ROOT framework. The purple planes represent the outer edge of the DS-ECal. The vertical and horizontal strips correspond to the scintillator bars that register a charge signal from the cosmic ray while the colour is a sliding scale of the charge. This particular MIP traverses the entire detector.

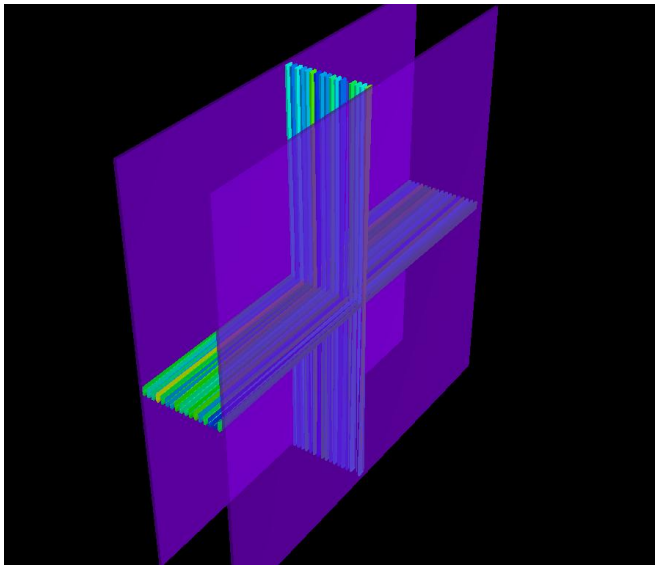

Fig. 7.4. Event display of a straight through-going cosmic ray muon traversing the DS-ECal.

The hit maps were produced using the hit information of events collected in a cosmic data file. The information carried by the hits includes the particular layer, bar and sensor that recorded the hit, and the charge detected by the MPPC sensor for that hit. The measured charge value is the basic quantity measured by the MPPCs and electronics chain. The electronics digitises the charge in units of ADC channels. The reconstruction software uses MEUs (MIP Equivalent Units) which is a calculated value proportional to the energy of the particle. The MIP energy

is defined as the energy deposited by a muon crossing at normal incidence through 1 cm of scintillator. This provides a reference point from which path length corrections can be made for particles crossing at an angle to the normal incidence. The calibration is executed in two stages. Firstly the measured charge (in femto-coulombs) is converted to the number of photons on the face of the MPPC. Stage two uses the reconstructed position of the hit to calculate the number of photons created by the original energy deposit. It is stage two that is of most interest to the content of this thesis since the reconstructed position is required in order to perform an attenuation correction. The attenuation correction directly addresses stage two of the calibration by correcting the energy that we measure at the end of a bar, to the energy that was actually deposited by a particle in the bulk of the detector. The attenuation of light in the WLS fibre affects the calculation of the number of photons created by the original energy deposit. This is explored further in Chapter 8.

A 2D map can be constructed from the layer and bar information and the number of photons detected. Figures 7.5 and 7.6 show the reconstructed hit maps for the X- and Y-views respectively when the detector is oriented in the normal position as shown in Figure 7.2. The number of hits detected is represented by a colour gradient. A total of approximately 40 k cosmic triggers were collected for this particular dataset. The first thing to point out in Figure 7.5 is that the empty region in the top-right of the figure is due to a 'dead' region of the DS-ECal. Two TFBs failed to output any signal during the testbeam phase. Their known positions combined with the hit maps contributed to the verification of the channel mapping.

The cosmic ray trigger uses the downstream trigger towers in the DS-ECal (upstream in terms of the orientation setup at CERN). Some regions of the DS-ECal are shadowed, i.e. they have lower geometrical detection efficiencies, by the manner in which the module is triggered for cosmic rays at CERN. Particularly 'hot' channels could also be identified with this technique and some hot channels are visible in each of X- and Y-view hit maps, highlighted by the yellow-red squares that have a total number of hits detected twice the average rate across the detector.

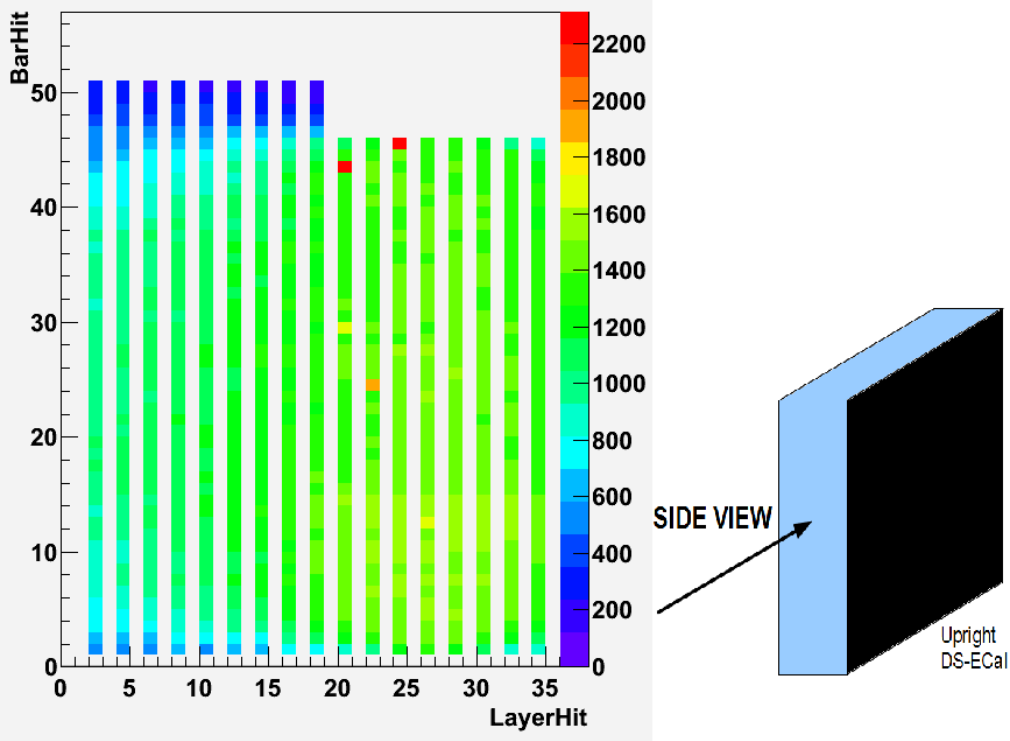

Fig. 7.5. X-View hit map. This view is looking down on the top of the upright DS-ECal and displays the hit distribution recorded by the scintillator bars that are oriented perpendicular to the ground. Approximately 40000 cosmic ray events populate this hit map. The total number of hits detected by the sensors at both ends is represented by the colour gradient. The 'dead' TFB region is visible in the top right of the histogram.

The testbeam experience was invaluable for providing the T2K experiment a headstart on producing calibration techniques. Further work is required to calibrate the data collected during the beam tests more accurately. The hit maps provide a useful tool for looking at cell to cell variations and for highlighting missing or under-performing channels. This is most evident in Figure 7.5 where the 'dead' TFB region is observed in the top right of the detectors for bars 46 through 50 of even layers between layers 20 and 35 of the DS-ECal. The low level calibration of the MPPC sensors needs to be refined further and in particular the range switching between low and high gain channels. The testbeam data will be analysed further in the future for the testing of sophisticated algorithms including an ECal particle identification (PID) algorithm. A number of analyses are planned for understanding the library of hadronic and electromagnetic shower profiles that were measured during the test-beam at energies below 1 GeV. Testbeam data will

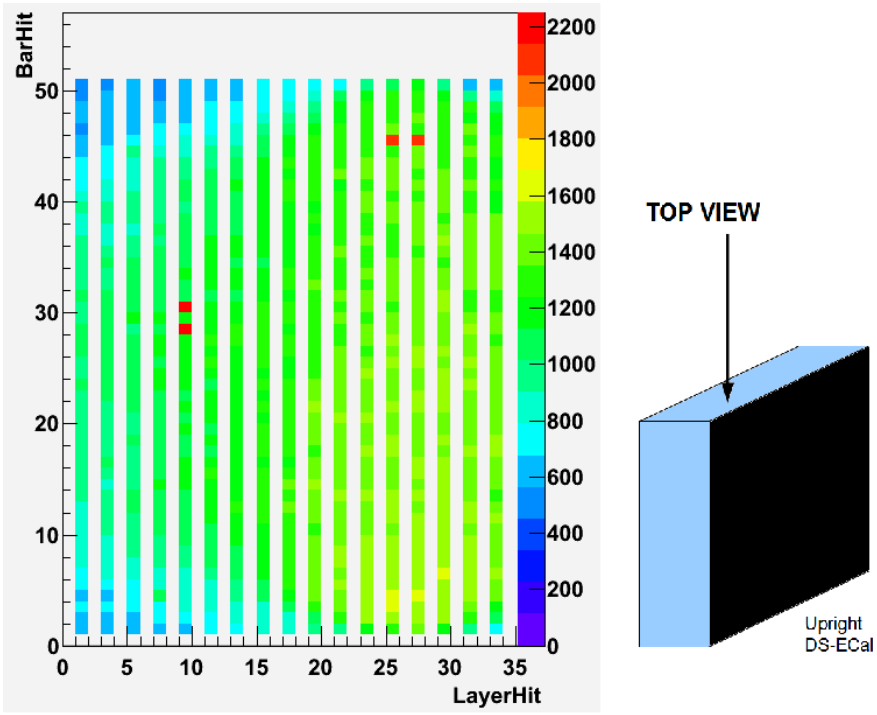

Fig. 7.6. Y-View hit map. This view is looking at the side of the upright DS-ECal, where the testbeam would be directed from right to left. It displays the hit distribution recorded by the scintillator bars that are oriented parallel to the ground. Approximately 40000 cosmic ray events populate this hit map. The total number of hits detected by the sensors at both ends is represented by the colour gradient.

be used to compare simulation to actual detector behaviour for electrons since electrons made up a large fraction of the particles in the testbeam. The electrons can be used to test the ability of the simulation software to predict the behaviour of electromagnetic showers. The testbeam time provided valuable experience for the commissioning of future ECal modules in a beam environment before the DS-ECal detector embarked on its journey to be the first ECal installed in ND280.

Chapter 8

Calibration

Cosmic ray (CR) muons are often used for energy calibration of detectors. CR muons are MIPs, which means that the energy losses along their path lengths are almost constant and independent of their initial energy. This source is used for calibrating by requiring that the mean energy deposit per unit path length for all detector channels is the same. One of the components that goes into the energy calibration and needs to be corrected for is attenuation. We know that light attenuates along the length of the WLS fibre and, remembering that they are 2 m long in the DS-ECal, we need to measure the extent of this attenuation by comparing the energy deposits at different distances from the photosensor.

However, before one can measure and correct the attenuation effects, some of the lower-level calibration must be done. In this chapter, these primitive calibrations are described briefly before the discussion of the attenuation measurement.

8.1 ECal Calibration

The calibration chain for the ECal can be separated into three distinct stages. A TFB electronics calibration is the first step, followed by a MPPC calibration and completed by a calibration of the scintillator bars. The scintillator bar calibration requires some reconstruction information, such as the position of hits, before an attenuation correction can be determined.

8.1.1 TFB Calibration

The TFB calibration is required to address changes in the ambient conditions, such as temperature, that cause the number of ADC counts per MIP to drift. The Trip-t charge signal, in terms of ADC counts, was found by combining the integrated charges of the high and low gain

channels as described in Section 4.2.4. The drift of the electronics pedestal value was recorded on the order of once every hour. The pedestal value was subsequently subtracted from each gain channel. The drift in the pedestal over time was comparatively low, varying by approximately 0.5 ADC counts during a 10 hour period. A linearity correction was applied, following the pedestal subtraction, in order to produce a linearised ADC charge value. The TFB has a Digital-to-Analog Converter (DAC) setting that controls the charge injection (CI) capacitor. The result of the CI was previously given in terms of anode charge in femto-coulombs (fC) but is now in ADC-like units (DAC or ADC-lin) since only a linearised value needs to be given to the MPPC calibration stage for further corrections. Several non-linear effects are present when looking at raw ADC values, including saturation of both high and low gain channels and a second order effect whereby saturation of the high gain affects the low gain. This is evident in Figure 8.1 which shows how the linearised ADC charge (or reconstructed, Reco, DAC as it is labeled) is achieved by switching the charge range on Reco DAC between the low and high gain channels in order to avoid the saturation points. If the reconstructed DAC from both high and low gain channels is below 300 DAC, the high gain channel is used for the calibrated charge, otherwise the low gain channel is used as reflected in Figure 8.1. The low gain channel saturates at low DAC values as shown from its extent into negative DAC values, therefore the high gain channel is used. The high gain channel saturates above 300 DAC so the range switch is made to the low gain channel so that the charge range used gradually falls beyond 300 DAC.

During dedicated CI runs known charges were injected into each ADC channel in order to be able to map the response of each of the channels. The applied charge was plotted as a function of ADC count for each channel and the distribution curves were fitted with a third order polynomial. The fit parameters were stored as the TFB calibration constants to correct the data. A total of 99.7% of the channels had a charge calibrated to within 5% [73].

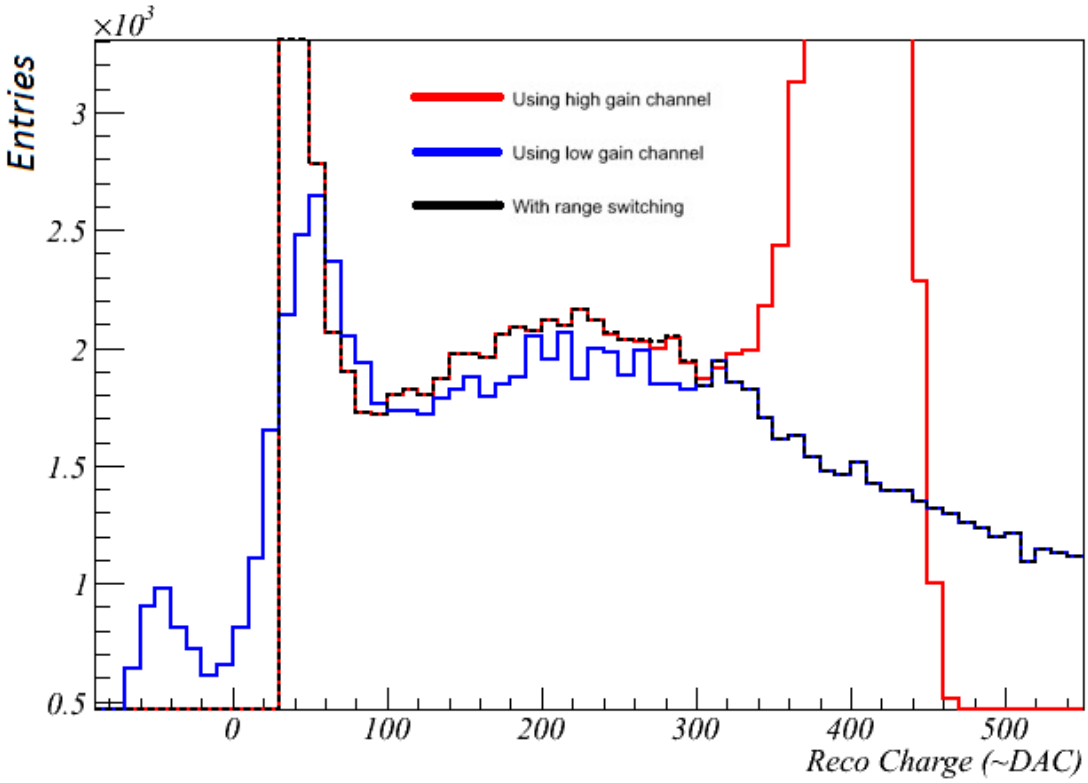

Fig. 8.1. Charge range switching on reconstructed DAC values from cosmic ray data. Above 300 DAC, the red high gain channel histogram saturates so the low gain channel is used for the charge range. Below 300 DAC the high gain channel is used. The low gain channel saturates at low DAC values shown by the blue histogram with negative DAC values. The charge range used is represented by the black histogram that gradually falls beyond 300 Reco DAC [73][74].

8.1.2 MPPC Calibration

In order to calibrate the MPPCs, the sensor gain, noise and PDE are calculated. These quantities were introduced earlier in Section 4.2.3 so I will not re-address them here. Each of the MPPC characteristics need to be characterised when accounting for the response of the individual MPPCs. As a reminder, there are a total of 3400 MPPCs read out of the DS-ECal and 22336 total MPPC sensors in the entire ECal subsystem. The charge of each of the sensors is converted into a number of pixels fired in the MPPC, a pixel-equivalent unit (PEU) and then to a number of photon equivalents(PE) which is a second-order correction accounting for the (intensity dependent) efficiency to amplify a PE. A MPPC does not produce photo-electrons like

a PMT does. The concept of a photon equivalent is that it is the charge produced (on average) by a single photon, which is slightly higher than the avalanche on a single pixel, because of cross-talk and after-pulsing. The number of pixels fired in the MPPC is proportional to the number of photoelectrons detected.

8.1.3 Scintillator Calibration

The DS-ECal is a sampling detector as it does not measure all of the energy losses by a charged particle, but only a fraction of the energy deposited on active scintillator planes. When a charged particle traverses the detector, it continuously loses energy through excitation or ionisation of atomic electrons. Energy loss is a stochastic process, i.e. particles with the same initial conditions lose different amounts of energy when passing through the same scintillator layer. Therefore, the distribution of energy deposits on a scintillator layer by a number of particles does not form a discrete function or a delta function, but a Gaussian-like distribution. This distribution is more skewed (Landau-like) for very thin scintillator layers or gas detectors. The scintillator planes of the DS-ECal are 1 cm-thick so we can describe the energy deposition in the planes with a Landau distribution. The mean energy loss of heavy charged particles, in particular muons, in a medium is given by the Bethe-Bloch formula [7]:

$$-\frac{dE}{dx} = Kz^2\frac{Z}{A}\frac{1}{\beta^2}\left[\frac{1}{2}ln\frac{2m_ec^2\beta^2\gamma^2T_{max}}{I^2} - \beta^2 - \frac{\delta(\beta\gamma)}{2}\right], \tag{8.1}$$

where

- $T_{max} \simeq 2m_ec^2\beta^2\gamma^2$ is the maximum energy transfer to an e^- in a collision
- $K = 4\pi N_A r_e^2 m_e c^2$
- N_A is Avogadro's number

- r_e is the classical electron radius
- I is the mean excitation energy
- $\delta(\beta\gamma)$ is the density effect correction to the ionisation energy loss

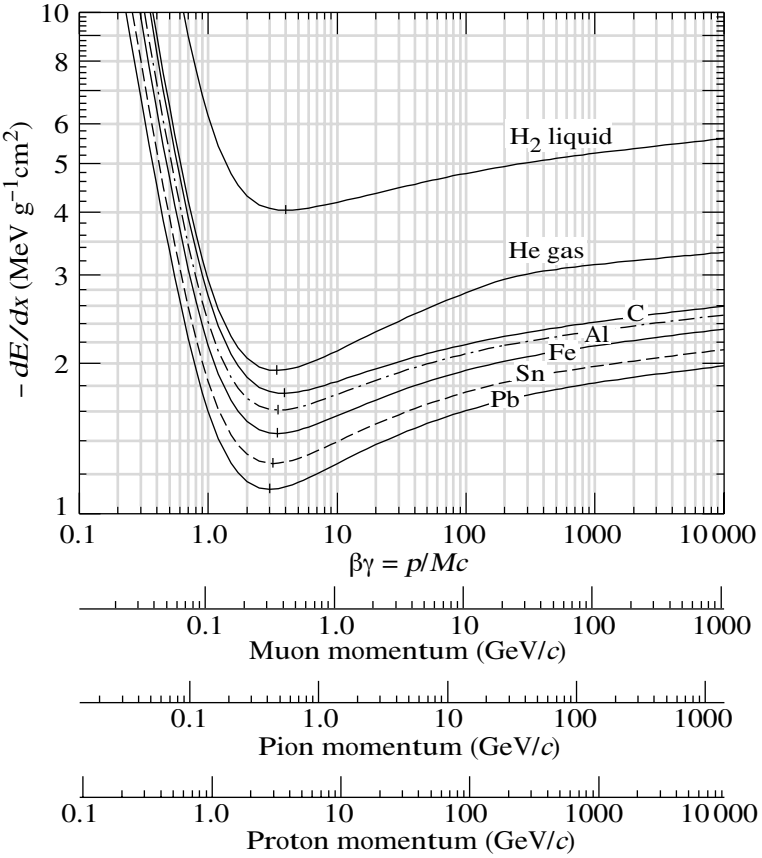

Fig. 8.2. Mean energy loss rates in liquid hydrogen, gaseous helium, carbon, aluminum, iron, tin, and lead, as described by the Bethe-Bloch formula. The energy loss rates are compared as a function of momentum for muons, pions and protons [7].

A muon with $\beta\gamma \simeq 3$ has the smallest ionising power and is thus called a Minimum-Ionising Particle (MIP) as can be seen in Figure 8.2. For low-energy charged particles, the mean energy loss is proportional to $1/\beta^2$, i.e. inversely proportional to the particle velocity squared, and does not depend on the particle mass. The region around 0.1 to 1 GeV/c is of the greatest interest for T2K. This is around the MIP region for muons.

Energy deposited in a scintillator generates scintillation light and is measured in terms of the number of photoelectrons detected or light yield. There are corrections that must be made to this light yield. The first correction is to account for the path-length difference in a scintillator layer as particles with longer path lengths deposit more energy in the same layer,

$$Q \rightarrow Q_0 * \cos\theta \,, \tag{8.2}$$

where θ is the angle between the particle direction and the azimuth when considering cosmic ray muons. Q_0 is the charge recorded by the detector as a result of the particles energy deposit. The second correction is for the light attenuation along the WLS fibres. An attenuation correction factor for the energy deposit at distance x from the readout MPPC, $A(x)$, is applied to Equation 8.2 such that the corrected charge, Q_{corr}, is of the form

$$Q \rightarrow Q_{corr} = \frac{Q_0 * \cos\theta}{A(x)}. \tag{8.3}$$

It is this correction factor, $A(x)$, that is the focus of the remainder of this thesis.

8.2 Attenuation Correction

Muon energy loss is described in electromagnetic interactions via ionisation, $e^+ - e^-$ pair production, bremsstrahlung and photo-nuclear interactions. Below approximately 200 GeV, and hence for the interactions in the DS-ECal, muon energy losses are predominantly due to ionisation. There is a steady flux of cosmic ray muons everywhere on the Earth's surface, with an average energy of approximately 4 GeV. The overall angular distribution of muons at the

ground is $\propto \cos^2\theta$, where θ is measured with respect to the azimuth [7]. The rate of external muons through the ECal is of the order of 100 Hz. The high-energy muons pass right through the plastic scintillator in the DS-ECal and in doing so deposit energy through electromagnetic interactions with the scintillator material or with the lead which produces particles which scatter into the scintillator. The rate of energy loss is determined by the initial energy and the atomic number (Z) of the material. Some fraction of the deposited energy gets converted to photons by the scintillator material. The muons ionise atoms in the Pb which means there are electrons getting knocked out into the scintillator that will undergo bremsstrahlung, producing photons that will deposit their energy in the scintillator volume, or ionisation of the scintillator atoms. The scintillator re-emits blue light in the neighbourhood of the interaction. Some of the light crosses the central hole of the bar and some of this crosses into the WLS fibre. A proportion of this light is trapped in the fibre and carried along the length of the fibre and is wavelength-shifted by dopants into green light so that it can not be absorbed by the fibre material. The light is transmitted by total internal reflection along the fibre and is attenuated only by geometric factors such as reflection at the cladding. Approximately one hundred thousand photons per deposited MeV energy loss are created by the initial interactions with the scintillator whereas just a handful are detected as the number of PE show in the calibrated charge spectra.

The light attenuation is caused by several factors including self-absorption and reflection losses in the WLS fibre as noted in Section 6.1.3. By definition, light attenuation is the reduction in intensity of the light signal with respect to the distance the light has traveled between the point of generation and the point it is converted into an electric signal. Consequently, the position dependence in the calorimeter response arises from light attenuation effects. It should also be noted that the light attenuation characteristics of scintillators change with time, particularly when the scintillator is operated in a high radiation field [14][75], though on the time-scale of the T2K experiment this is expected to be a negligible effect. Nevertheless, this effect can be monitored periodically throughout the lifetime of the DS-ECal.

The attenuation correction method described here was devised to produce attenuation profiles for each channel and, subsequently, attenuation constants that could be applied in the calibration scheme to correct for the attenuation of light along the WLS fibres of each ECal channel. The data sample used was cosmic ray data taken by the DS-ECal module during data-taking at CERN and on the surface at Tokai, with the DS-ECal in the '*flat*' configuration, as described in Section 7.2.1 and shown in Figure 7.3. As a result, the cosmic ray data consists of primarily straight, MIP-like muon particle tracks that pass through the entire detector and are the simplest tracks to reconstruct.

8.2.1 Simple Track-Reconstruction Algorithm

A simple track-reconstruction algorithm was devised for the purpose of reconstructing the hit information recorded by the MPPC sensors for straight muon tracks crossing the DS-ECal. A hit was defined as a measured energy deposit in the detector in Section 7.2.1. The algorithm works with raw data that has not been passed through any previous software reconstruction steps. The position of each hit on a given bar is estimated using the $\hat{\mathbf{x}}$-$\hat{\mathbf{y}}$ layer orientation of the DS-ECal. In order to do this, it is a fair assumption that, for each event, the highest charge depositions recorded are a result of CR activity. Therefore, the underlying principle for this tracking algorithm is to find the highest charge hit in each layer for each event.

The $\hat{\mathbf{x}}$-$\hat{\mathbf{y}}$ orientation of the DS-ECal layers leads to two views of the module; a $\hat{\mathbf{x}}\hat{\mathbf{z}}$ view and a $\hat{\mathbf{y}}\hat{\mathbf{z}}$ view. The $\hat{\mathbf{z}}$ direction is parallel to the beam direction. Therefore, when the module is in the '*flat*' position, the $\hat{\mathbf{z}}$ direction is in the azimuth direction. The basis for the hit position reconstruction is to utilise the known hit bar position in the alternate view. When looking in the $\hat{\mathbf{x}}\hat{\mathbf{z}}$-view, the bars associated with track hits are known in the $\hat{\mathbf{y}}\hat{\mathbf{z}}$-view. The position of the track hit along the bars in the $\hat{\mathbf{x}}\hat{\mathbf{z}}$-view is unknown as depicted by Figure 8.3.

Figure 8.3 demonstrates the orientation of the bars and their readout WLS fibres - which go to the MPPC sensors - within three successive layers. The position of the hit along the bar in

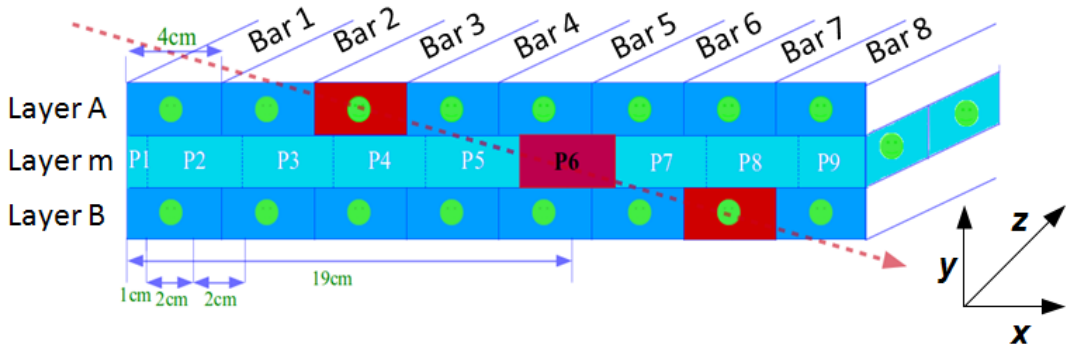

Fig. 8.3. A muon traversing the detector is shown by a red dashed line (top left to bottom right). Also the brick-like structure of the ECal is shown. The circles represent the position of the MPPCs. The middle layer (Layer m) has no circles on the front face because due to the $\hat{\mathbf{x}}\hat{\mathbf{y}}$ structure of the ECal, its MPPCs are along the side of the module (shown at the right). We are interested in the bar of Layer m. For that bar, the *pixel* through which the track crosses is determined from the bar of the layer above (Layer A) and the bar of the layer below (Layer B), shown in red, that records a hit. In this case the hit in the bar in question occurs in *pixel* 6. This is determined by extrapolation knowing that Bar 3 in Layer A and Bar 7 in Layer B have hits.

the middle layer (Layer m) is unknown but can be inferred from the bar that is hit in the layer above ($B_A \equiv B_{m+1}$) and the bar hit in the layer below ($B_B \equiv B_{m-1}$). Along the length of each bar, we consider 50 subsections, 4 cm wide, that will be referred to from now on as *pixels*. We localise the hit to be in the centre of the pixel in order to give a hit position in reference to the length of the bar in the middle layer. The error on the position is defined by the width of the bars since the pixels have the same dimensions as the bars. The bars are 4 cm in width so the error on position is defined as ± 2 cm. The pixel subsections give rise to a brick-like, '*pixelated*' view of the DS-ECal. The position of the particle track hit in the middle layer (Layer m) can now be deduced by the following:

$$\text{Pixel in Layer } m = \left(\frac{Bar_{m+1} + Bar_{m-1}}{2}\right) + 1. \tag{8.4}$$

For the track in Figure 8.3, this results in a hit along the middle bar corresponding to a hit in pixel 6 (according to Equation 8.4). This is equivalent to a position of 19 ± 2 cm from the MPPC at the left end. The position is equivalent to 200 - 19 = 181 ± 2 cm for the opposing sensor. The pixel definition has an offset of 1 cm from the left end in both views due to the consideration of muons crossing the detector at an angle to the $\hat{\mathbf{z}}$ direction. Without the offset, multiple hits would be reconstructed to cross two pixels in one layer. The offset allows the algorithm to favour one of the two pixels in order to define position. This has a negligible effect on the position estimation since the error on the position, ± 2 cm, is larger than the 1 cm offset.

This method works for all but the first and last layers of the DS-ECal since there is no layer above or layer below for the first and last layers respectively. They are treated with the same pixel reference scheme but in the case of the uppermost layer, the pixel number is defined to be the same as B_{m-1}. The pixel number is defined to be B_{m+1} for the last layer.

It is necessary to ensure that all hits of a given track are associated with the track and not, for example, a high charge noise hit. This is done by considering each hit in turn and then checking that the hit in the layers 2 and 4 above and below the layer of the hit in question fall within ± 5 bars of the bar in question. If any hit should fail this condition then the hit in the same layer with the next highest charge is selected and required to meet the same condition. Should this condition still not be met, then no hits are associated with the track on this layer of the detector. This selection criterion is best demonstrated in Figure 8.4, where the initially selected hit in red is later rejected for not being within ± 5 bars of the bar that is under examination. In this case, the next highest charge hit selection (yellow) is within the ± 5 requirement and is associated with the track.

Due to an event being defined as occurring within a 540 ns DAQ integration window, it is possible that an event may have more than one CR muon. Hence, the algorithm requires that one (and only one) through-going muon track is reconstructed for each cosmic event in order to reduce the problem to the simplest case. This is accomplished by scanning the charge

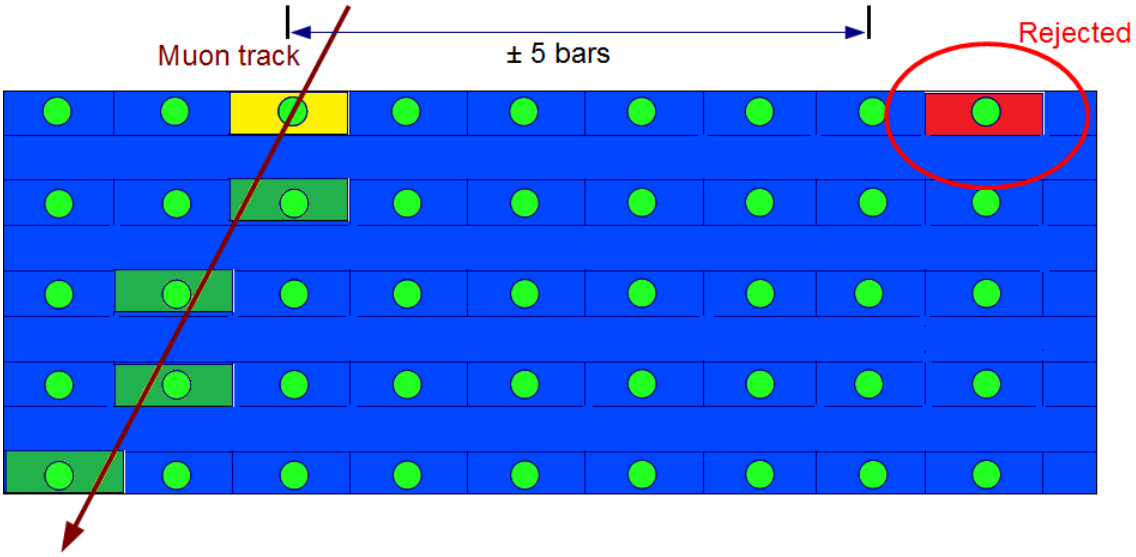

Fig. 8.4. A 2D schematic of a track-finding hit selection in the DS-ECal. It shows 4 hits that are selected belonging to the track (green) and one hit that is initially selected as part of the track but then rejected for being too far away from the other hits, in red. The next highest charge hit-selection (yellow) is within the ± 5 bar requirement and is consequently associated with the track.

recorded by each bar of a layer and reconstructing tracks using the highest charge hits in each layer coupled with selecting associated hits in subsequent layers as described above.

8.2.2 Track-Reconstruction Algorithm Validation

The track-reconstruction algorithm has been validated by comparison with the same events recorded in the dedicated ND280 Event Display. The easiest method to achieve this is by simply printing the layer, bar and pixel number of hits selected by the algorithm for one muon event and matching the hits to the equivalent muon track in the EventDisplay package. Figure 8.5 shows a single CR muon event that was selected by the algorithm and verified by checking the corresponding geometry outputs. The DS-ECal was in the '*flat*' position as defined in Figure 7.3 which infers that the CR particle track, from the vertical direction, is from right to left in the Top and Side views (not as obvious at first in the 3D view). Each strip of colour represents

a single bar that has recorded a hit while the colour is a sliding scale of charge deposition with blue being low charge and yellow being high charge. The top and side views are also shown.

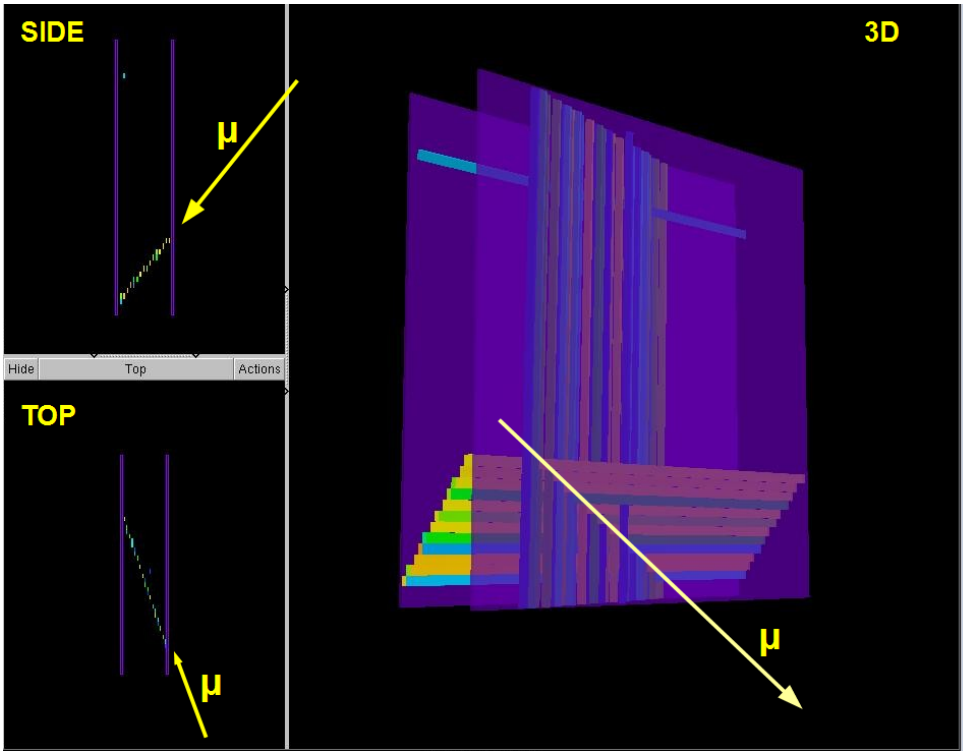

Fig. 8.5. Event display showing a single CR muon crossing the detector. The DS-ECal is in the 'flat' configuration so the vertical direction is from the right of the image. Each strip of colour represents a single bar that has recorded a hit while the colour is a sliding scale of charge deposition with blue being low charge and yellow being high charge. A 3D, top and side view are all shown. The muon track enters the front face of the DS-ECal in the 3D view and from the right of the top and side views.

8.2.3 Charge Spectra

The attenuation correction study was first performed on the CERN cosmic ray dataset with the DS-ECal in the '*flat*' upside-down configuration, such that vertical CR's enter the detector through Layer 34 and exit Layer 1. The CERN CR dataset that is used in this thesis comprises 227 data files, each recording approximately 15 k CR trigger events for a total dataset of $\sim$ 3.4 M events, though not all of these events are due to cosmic activity. Initially, the study

looked at charge information from the high gain channel output of the sensors to mirror the method in the previous work with the 2D scanner described in Chapter 6 for comparison. At the time, the data calibration chain was not complete. In particular, the calibration constants for electronic pedestals and linearity, as described in Section 8.1.3, were not in place so a simple calibration of the high gain channel was used to read out charge in terms of PE as opposed to arbitrary ADC counts. The high gain channel value was calculated in PE by a simple subtraction of 150 ADC for the pedestal from the raw ADC count and then divided by a gain value of 12 ADC/PE. These values were obtained from a preliminary study [74] and apply to a single sensor, though are applied to all readout channels for this initial work. They allowed work to continue whilst calibration constants were being generated for each particular sensor. With this in mind, the charge spectrum of the high gain channel is shown in Figure 8.6, represented by the red, dashed upper histogram. The extent of the electronics noise below 15 PE is cut-off in order to compare the charge before applying the track reconstruction algorithm to the charge distribution reconstructed by the algorithm. The pre-algorithm noise is 4 orders of magnitude greater than that shown for post-algorithm (represented by the black, solid lower histogram). In both cases, the high gain charge saturates above approximately 63 PE. A series of cuts, or criteria, are applied to the reconstructed charge distribution before populating charge spectra for each pixel position along a bar. The first of those cuts is to eliminate as many noise hits as possible so only charge hits in the range 11 PE < Q < 63PE are selected.

The total high-gain charge information that was reconstructed by the algorithm was then histogrammed in terms of the reconstructed pixel positions. This produced a charge spectrum for all bars at 50 points along each bar for each MPPC. A convoluted Landau-Gaussian distribution was fitted to the distribution of charge for each pixel. As mentioned in Section 8.1.3, the distribution of energy deposited by a charged particle crossing a thin layer of material is described well by a Landau distribution. This is convolved with a Gaussian distribution to account for the signal-induced noise. Figure 8.7 shows the distribution of charge deposited at three positions

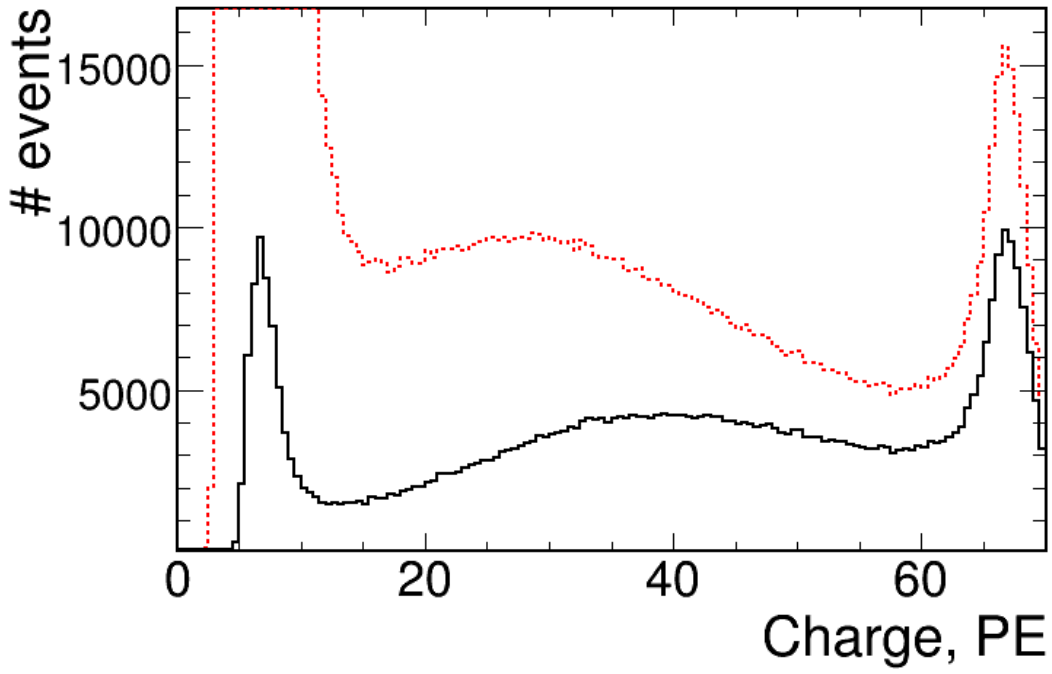

Fig. 8.6. Charge distribution of the high gain channel shown in units of PE, for pre- (red, dashed upper histogram) and post- track-selection algorithm (black, solid lower histogram).

along a given bar and the convoluted function can be seen to fit each distribution around the peak. The convoluted function calculates a Most Probable Value (MPV) for the charge distribution.

The pixel referencing for this particular sensor is such that the distance from the sensor decreases the higher the pixel number. It is the opposite for the sensor on the opposing end of the bar. The signal decreases as you move away from the sensor readout which determines that the MPV value should increase as the distance of the pixel from the sensor decreases. This is reflected in Figure 8.7. The MPV value increases from 20.82 ± 1.06 PE at a distance of 153 cm from the sensor for pixel 12 to 43.9 ± 1.9 PE at a distance of 49 cm from the sensor for pixel 38. The width parameter represents the width of the Landau distribution component of the convolution, likewise the GSigma parameter for the Gaussian component. The area parameter is the area under the Landau-Gaussian curve.

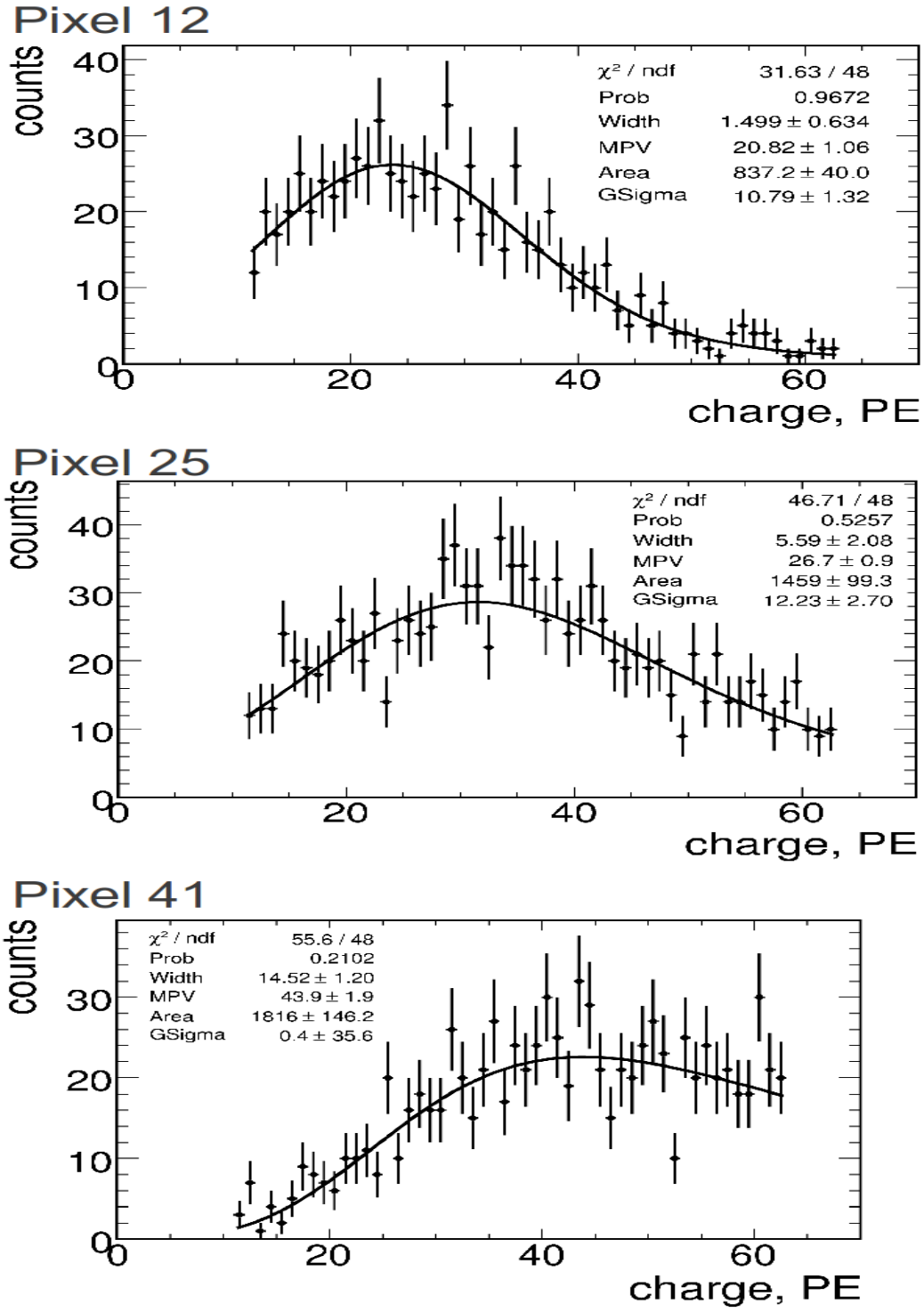

Fig. 8.7. Three example charge spectra for individual pixel numbers for CERN CR data. The charge spectra are from Layer 22, Bar 23 and one sensor end. In this case they are from pixels 12, 25 and 38 which are positions 47, 99 and 151 cm along the bar as for this sensor end. This equates to distances 153, 101 and 49 cm from the sensor readout end. The pixel referencing for this particular sensor is such that the distance from the sensor decreases the higher the pixel number. It is the opposite for the sensor on the opposing end of the bar.

The MPV values found for each pixel position along the scintillator bars is plotted as a function of distance from sensor readout and this represents the attenuation profile of the particular WLS fibre in the bar. Two typical attenuation profiles, one from each sensor of a particular WLS fibre and bar, are shown in Figure 8.8. The parameterisation of these profiles provides the attenuation correction required to apply to the signal from each MPPC in order to account for channel-to-channel differences arising from attenuation of the light along the WLS fibre. The differences in photosensor-fibre coupling, scintillator bar response and other variables make the response of each bar, and hence each channel on a bar end, different for the same energy deposition in the scintillator.

The first observation to make is that the double-exponential fit does not extend to the ends of the bars. Energy deposited near the end of the scintillator bar is lost due to absorption of light at the very end of the bar that is not painted but glued to the layer frame. Light created by the energy deposition "falls off the end" of the bar. The second observation to make from the typical attenuation profiles in Figure 8.8 is that the attenuation values, 153.7 ± 1.9 and 201.4 ± 22.6 cm, given by parameter P3 in the top right of the histograms, for the long attenuation lengths are much lower than the expected long attenuation values of approximately 350 cm. This is shown to be the case across all channels of the DS-ECal in Figure 8.9 which shows a distribution of long attenuation lengths from a double exponential fit to attenuation profiles for each DS-ECal channel. Values are not included if the double exponential fit has a chi-square per number of degrees of freedom > 10. Figure 8.9 does, however, show a level of consistency across the channels such that the long attenuation length is in the range 200 - 250 cm for the majority of channels.

The track-selection algorithm does not include a path length correction for these results. The algorithm does however reconstruct tracks with angles to the vertical, not just the vertically straight muon tracks. It is the angular tracks that need to be path-length corrected since the charge deposited from these particle tracks would register a higher charge deposit in the pixel

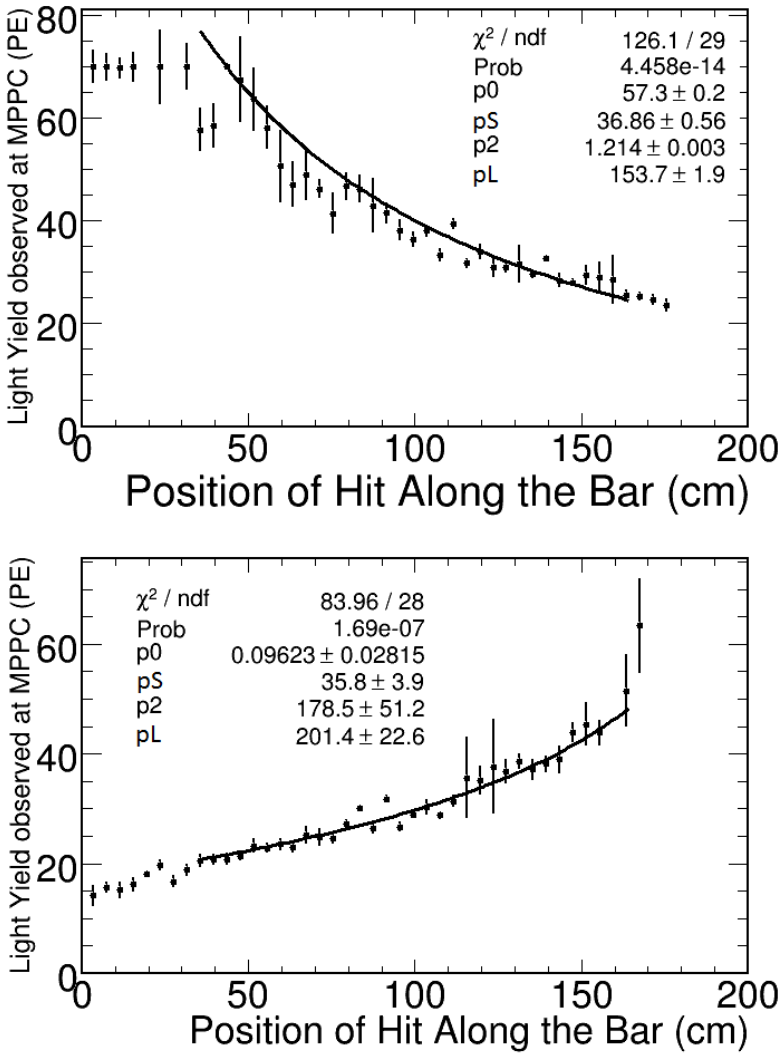

Fig. 8.8. Example attenuation profiles for CERN CR data. The high-gain charge information was used in the tracking algorithm. Each data point represents the MPV of the charge spectra at the particular distance from the sensor. A double exponential function is fit to the central region of the data. For the top histogram, the sensor is at position 0 cm and for the bottom histogram the sensor is at position 200 cm along the bar.

than a vertically-traveling particle of the same energy. Also, since the track algorithm requires that a particle deposits its energy in each layer, the most affected regions of the DS-ECal are those in the centre of the detector, which is the region in which the double exponential fit is applied. The hits in the pixels closer to the ends are less affected since only vertical tracks would record a hit in these regions due to the orientation of the DS-ECal. This is shown by the

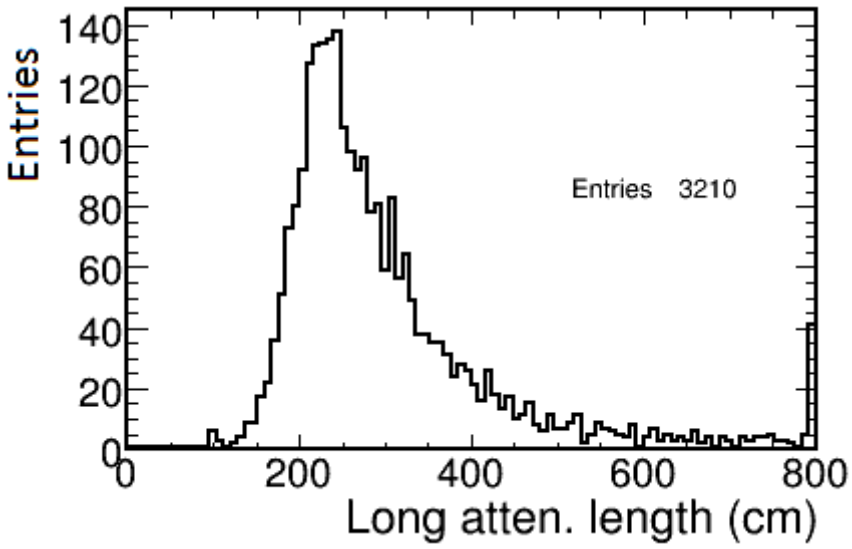

Fig. 8.9. Distribution of long attenuation lengths from the double exponential fit to the central region of the attenuation curve of all channels. The high gain charge is the input charge to reconstruct tracks from CERN CR data to subsequently produce this attenuation distribution.

following hit maps in Figure 8.10 which shows where the hits are recorded in the DS-ECal after being filtered by the track algorithm.

One can see that there is a reduction of selected hits at the far ends of bars. This is also, in part, an effect of the angular acceptance of the DS-ECal and also of the track-selection algorithm. The maximum angular acceptance of the DS-ECal, if tracks are required to cross each layer, is $\sim 79°$. Requiring a hit in each layer reduces the number of hits at the far ends of bars, notably for the lower half of the DS-ECal, because tracks that enter from the side are rejected. The additional requirement that hit selections be within $\pm$ 5 bars in up to 4 layers above or below reduces the maximum angular acceptance to $\sim 73°$. This effect indicates the need for a path-length correction of charge deposits in order to calibrate the charge as well as using the complete charge calibration chain.

8.2.4 Path-length Corrected Attenuation

As the electronic calibrations matured, it became possible to test our attenuation algorithms using data upon which the latest calibrations had been performed. At this stage of the

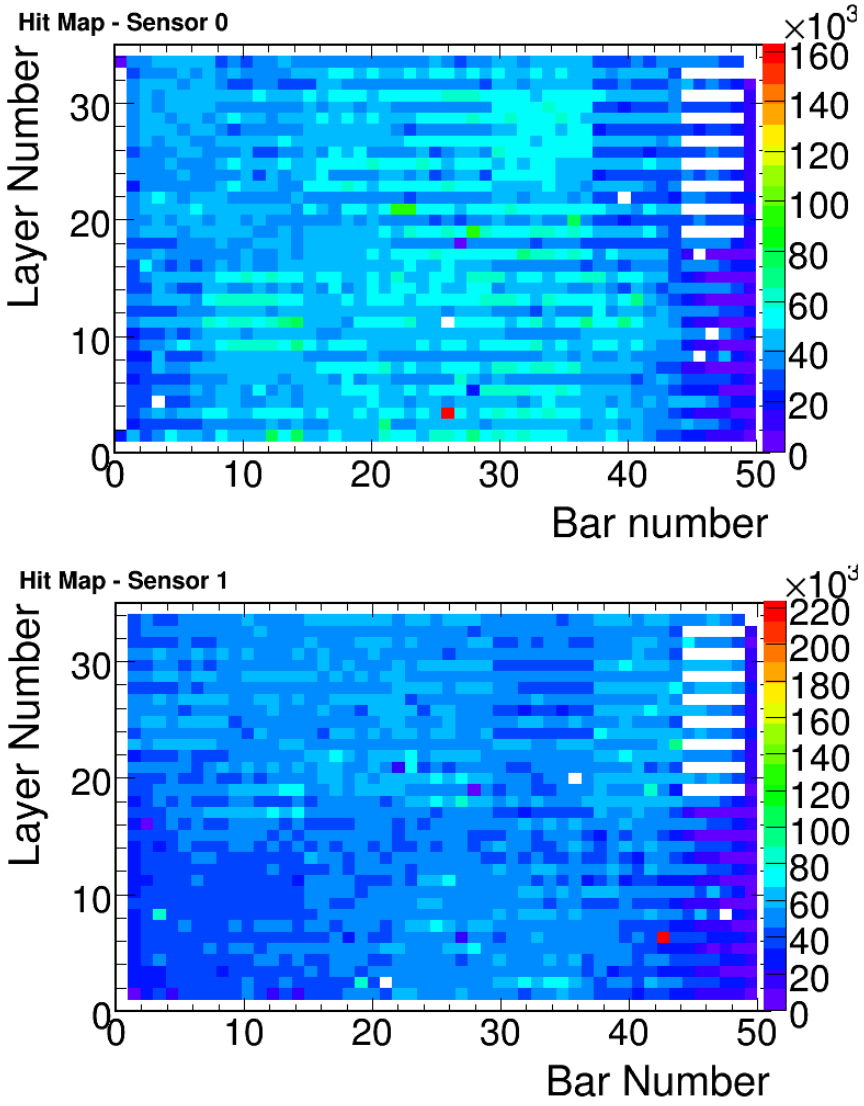

Fig. 8.10. Hit map of CR hit positions from selected tracks. There is a reduction of selected hits at the far ends of bars and notably for the lower half of the DS-ECal because tracks that enter the module from the side are rejected. The strips of white, empty space in the upper right of each hit map represent the region where two TFB's were non-operational during the CERN testbeam. The 'dead' TFBs, coincidentally, read out sensors from opposing ends of bars 46 through 50, in every other layer from 19 onwards. The randomly dispersed white squares are 'dead' channels.

calibration the charge is measured in pixel-equivalent charge units (PEU), that is to say MPPC pixels to avoid confusion with the track-reconstructed pixel positions. This allowed us to compare the results using high gain channel charge information to the results utilising the complete calibration chain with gain range switching. An attenuation and path-length correction are the final stages needed to achieve channel-to-channel response uniformity after the TFB and MPPC

calibration stages. The charge used to populate the charge spectra per reconstructed pixel position is the calibrated charge that is derived from range switching between the high and low gain ADC channels, as described in Section 8.1.3 and shown in Figure 8.1 earlier in this Chapter. The data that is shown in Figure 8.12 is the same CERN CR data as described in the previous section but now with the complete calibration chain applied. This is also compared to CR data recorded in Tokai. The Tokai data was also recorded for the DS-ECal in the 'flat' position on the surface before the module was installed in the ND280 pit underground in its correct upright position. The Tokai data presented in this thesis used a total of 107 CR data files, each containing approximately 15000 CR trigger events, for a total of approximately 1.6 M CR trigger events. This represents half of the size of the dataset used for the CERN CR data analysis in this thesis.

Figure 8.11 shows a comparison between the total charge recorded across the entire detector channels from CERN and Tokai cosmic ray data that have been reconstructed by the track algorithm to produce the charge spectra per pixel and subsequently produce the attenuation correction parameters. The events in the Tokai dataset, marked by the dashed red line, are normalised to the events in the CERN dataset as represented by the solid black line. The datasets are normalised for charge hits above 12 PEU and below 60 PEU since this is the region of interest for CR's. Below 12 PEU the signal is dominated by the electronics noise. There is very limited statistics above 60 PEU. The Tokai and CERN datasets compare well, differing slightly in part due to the fact that the two missing TFB regions in the DS-ECal at CERN led to some inefficiencies of the algorithm as well as the change in operating conditions of the detector and cosmic ray flux at the different locations. A further difference that the track-reconstruction may be sensitive to is that the integration time window of the TFB boards was set to 540 ns for testbeam data, including the CERN CR data, which is slightly longer than for the Tokai data that had the integration window set at 480 ns. This could give rise to possible minor differences in trigger efficiencies, although effects on the reconstruction of hits is likely to be negligible. The Tokai dataset has a slightly narrower CR peak of approximately 34 ± 4 PEU compared

to the CERN CR peak of approximately 37 ± 5 PEU. The spectra do not have Gaussian-like distributions because the algorithm selects the maximum charge hits in layers. This produces spectra that are more Landau-like in shape with a higher charge preference.

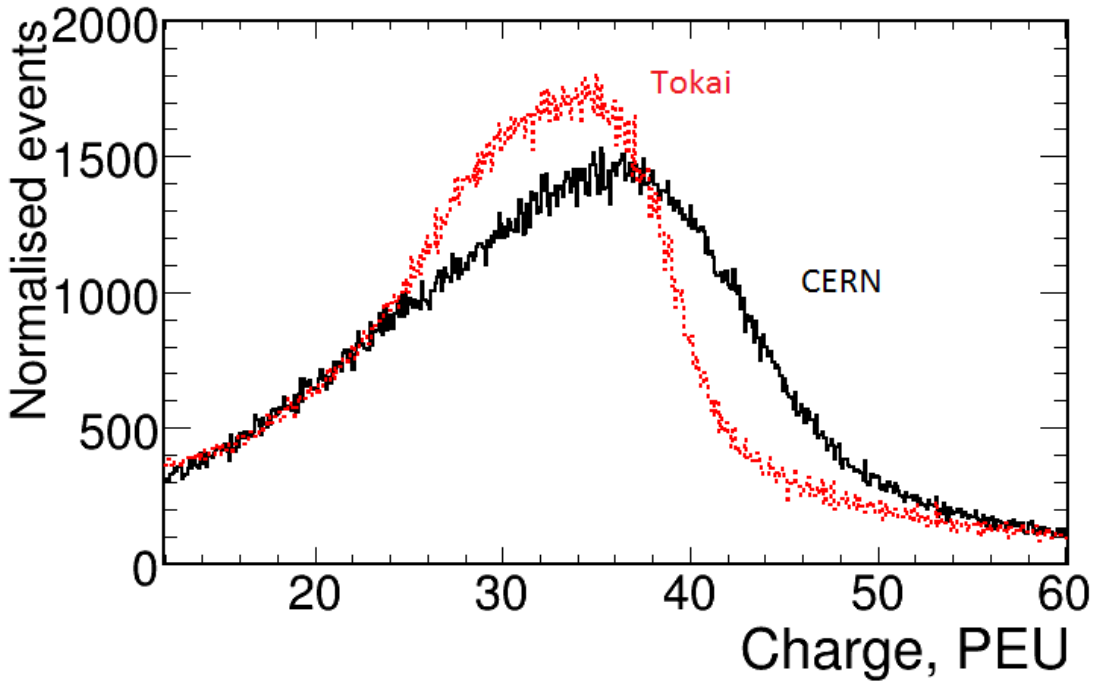

Fig. 8.11. Algorithm selected charge spectra from CERN (solid black) and Tokai (dashed red) cosmic ray datasets. The Tokai dataset is normalised to the CERN dataset for charge hits above 12 PEU and below 60 PEU. The Tokai dataset has a slightly narrower CR peak of approximately 34 ± 4 PEU compared to the CERN CR peak of approximately 37 ± 5 PEU.

The algorithm-selected calibrated charge information with the full range-switching effect is, as noted in Section 8.2.3, collected for each bar into the corresponding pixels which produces a charge spectrum for the bars at 50 points along the bar for each MPPC. A convoluted Landau-Gaussian distribution is fitted to the distribution of charge for each pixel. Figures 8.12 and 8.13 show the distribution of calibrated charge deposited at three positions along a given bar for the CERN and Tokai CR datasets respectively and the convoluted function can be seen to fit each distribution around their peaks. The same corresponding pixel positions as shown in Figure 8.7

are displayed for comparison. in Figure 8.7 the charge spectra was uncalibrated. The biggest contribution that can be observed by applying calibration to the charge is shown by the MPV values for pixel 41. In Figure 8.12 the MPV value for pixel 41 is 43.9 ± 1.9 PE compared to 27.65 ± 0.47 PEU. The calibration has improved the distribution from a broad Landau width of 14.52 ± 1.20 in the uncalibrated case to 1.96 ± 0.34 in the calibrated case. This results in a well defined peak to the calibrated charge distribution.

A contrasting observation that can be made, when comparing the calibrated charge spectra in Figures 8.12 and 8.13 with the high gain channel only charge spectra in Figure 8.7, is that the former are much more Landau-like shape than the latter. There are very few charge hits beyond 40 PEU in the histograms of Figures 8.12 and 8.13 due to the introduction of the full charge calibration chain. In particular the effect of the range-switching between low and high gain channels is apparent.

Comparing the calibrated charge spectra from each of the CERN and Tokai datasets one can see that, for these typical corresponding reconstructed pixel position spectra, the distributions are qualitatively consistent. The total charge spectra distributions for the Tokai and CERN datasets compared in Figure 8.11 are shown to have their mean values separated by approximately 2 - 3 PEUs, with the CERN dataset recording the slightly higher mean peak. The charge spectra MPVs in Figure 8.12, for the CERN dataset, are approximately 2 PEU higher than the MPVs at each pixel position in Figure 8.13 for the Tokai dataset. The MPV at each pixel position is then plotted as a function of distance from sensor readout for each channel. Figure 8.14 is a typical attenuation profile computed using this interpretation. The missing points along the profile are due to the criteria for plotting the MPV's. The chi-squared per number of degrees of freedom (chi-squared/NDF) of the Landau-Gaussian fit must be < 3 in order to use reliably fit MPV values and a further requirement is that the MPV is > 10 PEU since anything lower than this value resulted in a failed fit due to limited statistics for that particular pixel position. The attenuation profiles were fit with a double-exponential function of the form in Equation 6.5 in

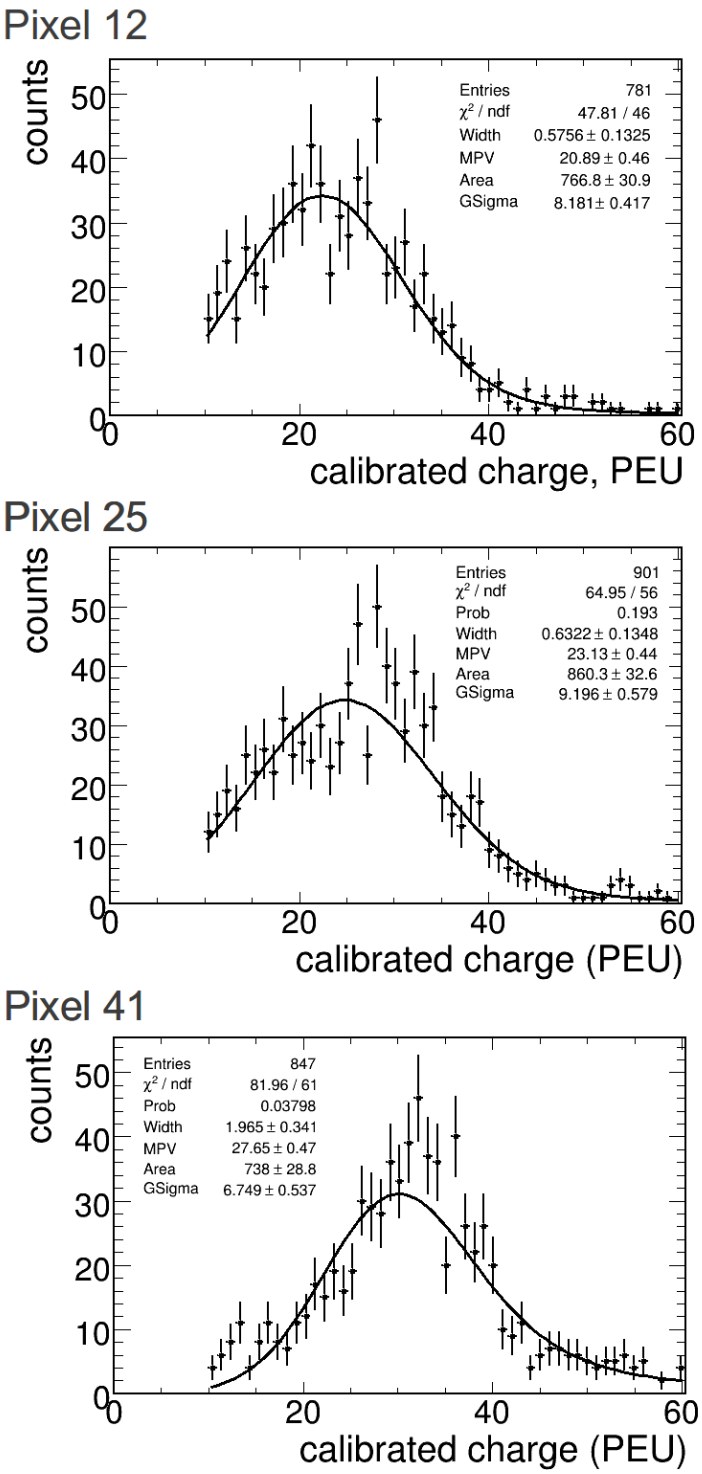

Fig. 8.12. Three examples of calibrated charge spectra for individual pixel numbers for CERN CR data. This data has passed through the complete calibration chain, including the charge range-switching. The charge spectra are for the same pixels shown in Figure 8.12 but calibrated here.

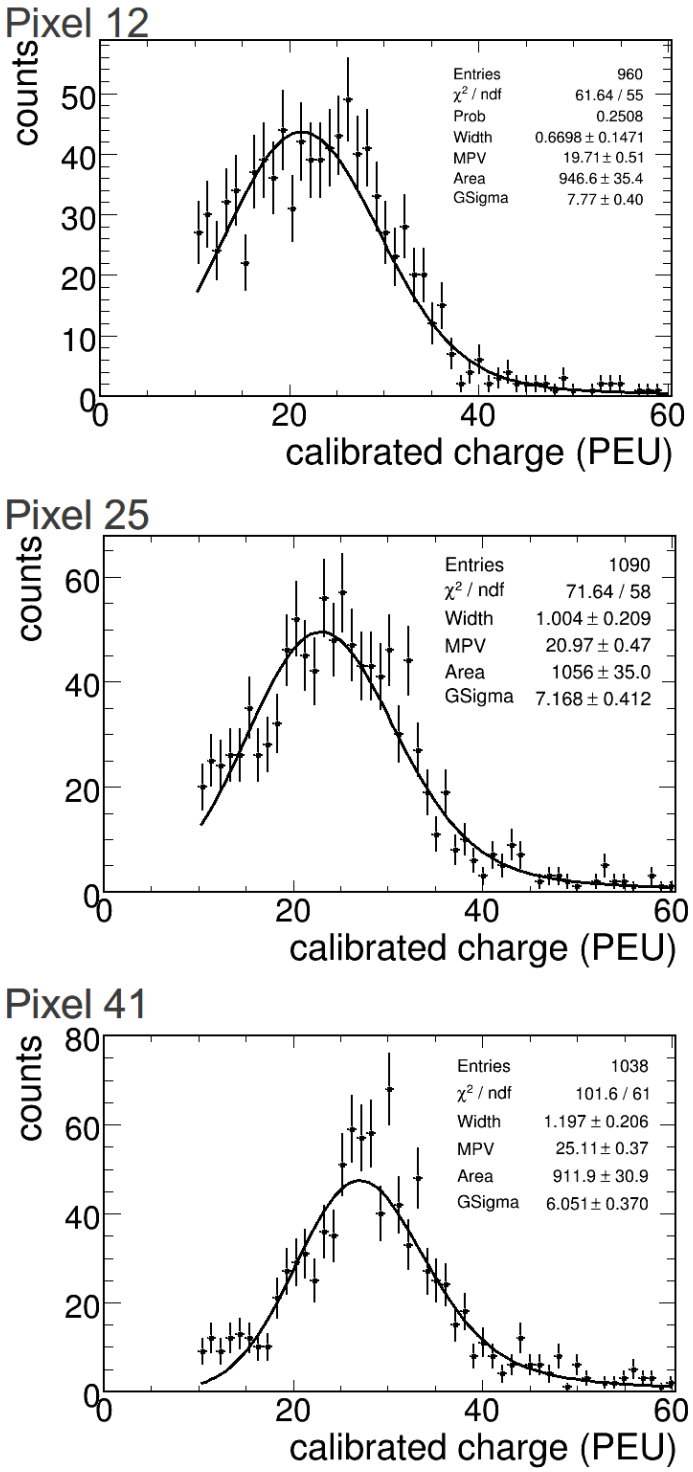

Fig. 8.13. Three examples of calibrated charge spectra for individual pixel numbers for Tokai CR data. This data has passed through the complete calibration chain, including the charge range-switching. The same pixel positions shown in Figure 8.12 are shown here for Tokai CR data.

the central region of the bar. The parameters of the double-exponential function are correlated such that neither relaxing nor constraining the upper and lower limits on the fit parameters could produce a consistent set of parameters across all bars and it resulted in a large number of failed profile fits. In particular, the fit parameters calculated in Figure 8.14 are such that the short attenuation length (pL) of 15 ± 1.1 is the lower limit of this particular fit. The fit is actually reasonably good with a chi-square/NDF value of ~ 4.5.

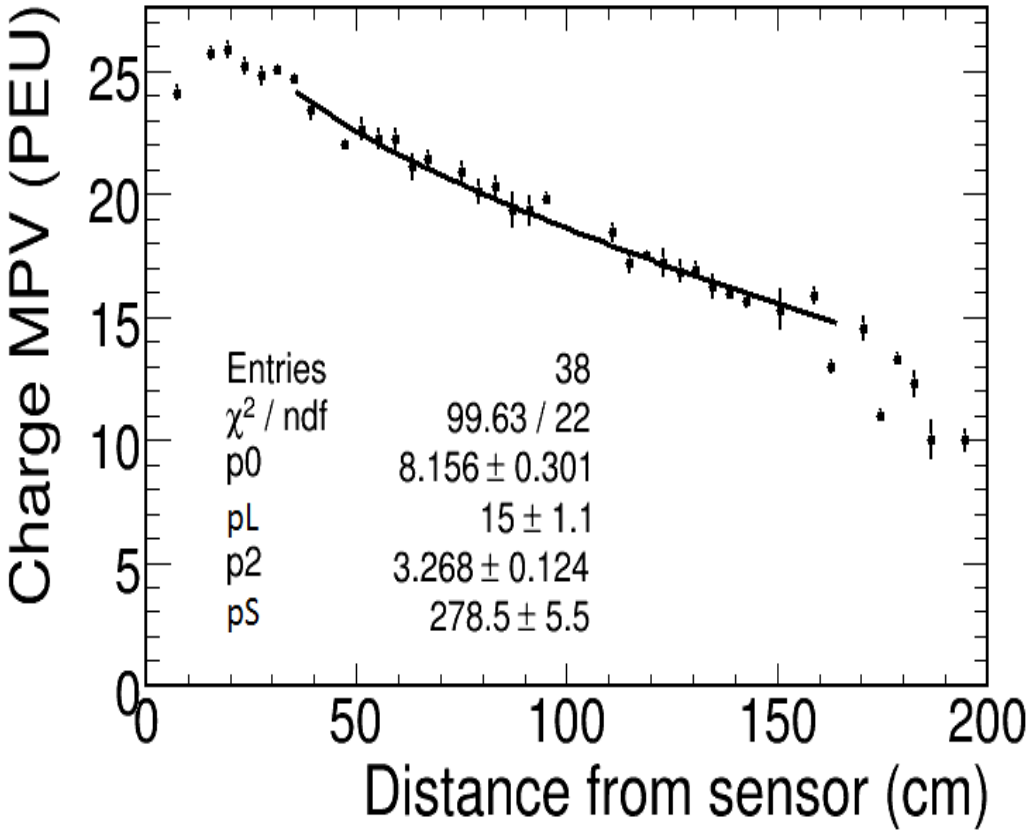

Fig. 8.14. Example attenuation profile of a scintillator bar using Tokai CR data. The profile is fit with a double-exponential in the central region of the bar.

The problem with only fitting a double exponential in the central region is that it doesn't include the complete region where the short attenuation length affects the overall attenuation of the fibre. A double exponential can not fully describe the attenuation profile for each channel.

As a result a function was derived in order to be able to quantitatively and qualitatively describe the attenuation profile along the full length of the channels, thus including the end effects that occur.

8.2.5 End Effects

It would be optimal to understand and parameterise the behaviour of the light attenuation to the very ends of the scintillator bars in order to maximise the fiducial volume of the detector. If end effects are to be included, the attenuation can be described by a quadruple exponential distribution, given by

$$A(x) = P_0 \left[e^{\left(\frac{x}{P_1}\right)} + P_2 * e^{\left(\frac{x}{P_3}\right)} \right] - P_4 * e^{(P_5 * x)} - P_6 * e^{(P_7 * [200 - x])}, \tag{8.5}$$

where x is the distance between the hit position and the MPPC readout, and the function parameters P_i (i = 0,1,2,3,4,5,6,7) are defined as

- P_0 = constant
- P_1 = short attenuation length (cm)
- P_2 = coupling constant (ratio) between the long and short attenuation lengths.
- P_3 = long attenuation length (cm)
- P_4 = normalisation of near end effect
- P_5 = near end effect turnover
- P_6 = normalisation of far end effect
- P_7 = far end effect turnover

In order to maximise the statistics available at the ends of the attenuation profiles, the information from all channels was combined in order to 'fold' the DS-ECal into one bar. To do this, the attenuation profiles from each channel were normalised to a MPV value of 1 in the centre of the scintillator bar, nominally 100 cm from the sensor end. The distribution of the mean MPV at each position along the bar across all channels was calculated. Figures 8.15 and 8.16 show the distribution of the normalised mean MPV across all channels for three particular positions along the bar, namely 153, 101 and 49 cm from the sensor readout, moving along the histogram from left to right, for CERN and Tokai CR data respectively.

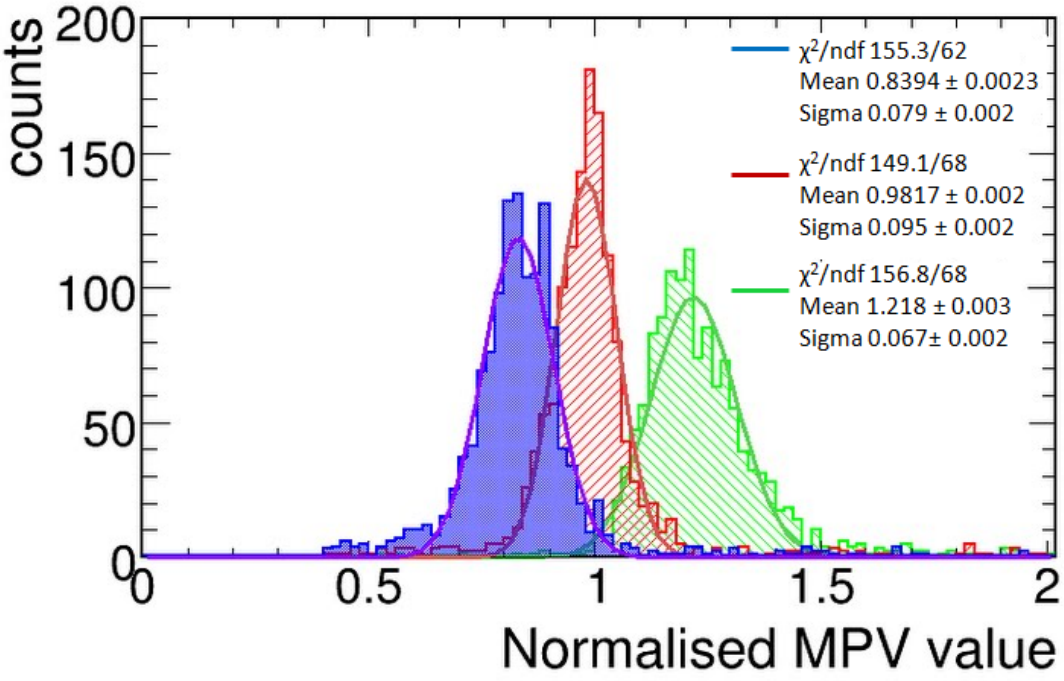

Fig. 8.15. Normalised mean MPV across all channels at three positions along scintillator bar using CERN CR data. The leftmost peak (blue) is closest to the sensor readout end. The MPV values for each pixel position along the bar have been normalised to an MPV of 1 in the middle of the bar. The three positions shown here, from left to right, are 153, 101 and 49 cm from the sensor readout.

In Figure 8.15, the CERN CR data was used and the histograms have a mean value of 1.218 ± 0.003, 0.9817 ± 0.002, and 0.830 ± 0.002 (moving left to right along the histograms) for

positions 153, 101 and 49 cm from the sensor readout. The standard deviation at each position is of the order of 10% which highlights the consistency of the MPV values across the channels. The mean and standard deviation, or width, values are calculated from fitting the distributions with a Gaussian function in each case. The mean normalised MPV's follow the expected trend of decreasing as the distance from the sensor increases. The corresponding mean MPV's using the Tokai CR data are 1.207 ± 0.003, 0.9875 ± 0.002, and 0.8379 ± 0.002. From these values, the CERN and Tokai data are shown to be consistent within approximately 1% for each mean MPV value.

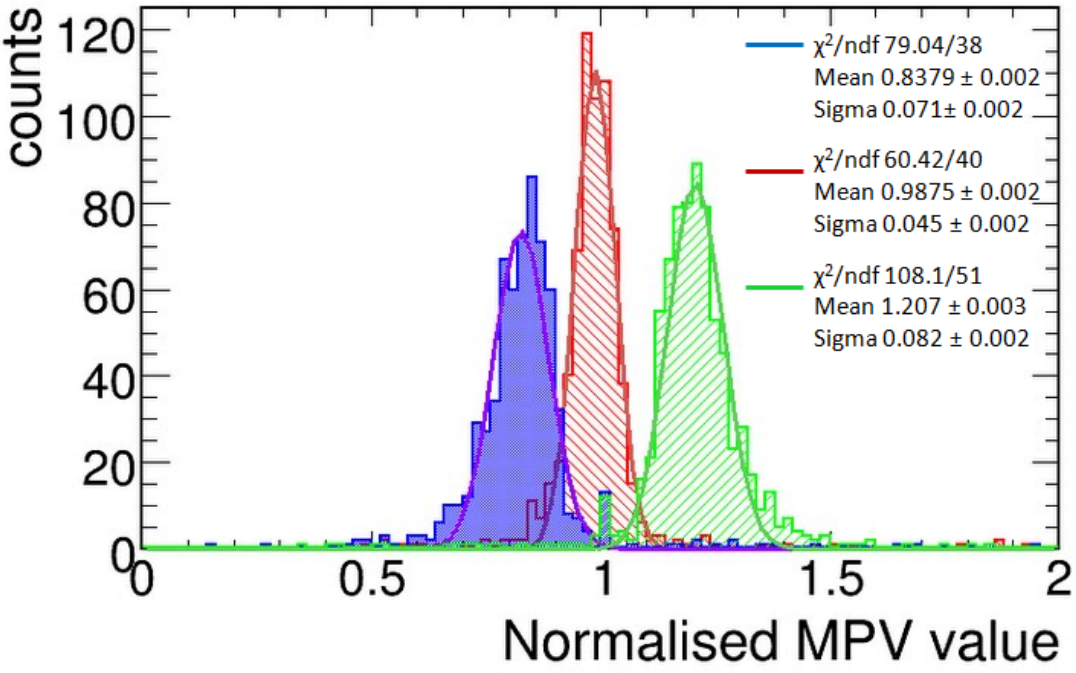

Fig. 8.16. Normalised mean MPV across all channels at three positions along scintillator bar using Tokai CR data. The leftmost peak (blue) is closest to the sensor readout end. The MPV values for each pixel position along the bar have been normalised to an MPV of 1 in the middle of the bar. The three positions shown here, from left to right, are 153, 101 and 49 from the sensor readout.

Figure 8.17 and 8.18 plot the mean of the MPV distribution peak as a function of the distance from the sensor readout, using the CERN and Tokai CR data respectively. The attenuation

profile data points in Figures 8.17 and 8.18 thus represent the mean of a Gaussian distribution of 1700 MPV's at each position along the bars. Due to the nature of the pixel position definition described in Section 8.2.1, there is a total of 98 MPV's, 49 from each sensor, contributed by each bar which is reflected in the combined attenuation profiles in Figures 8.17 and 8.18. The

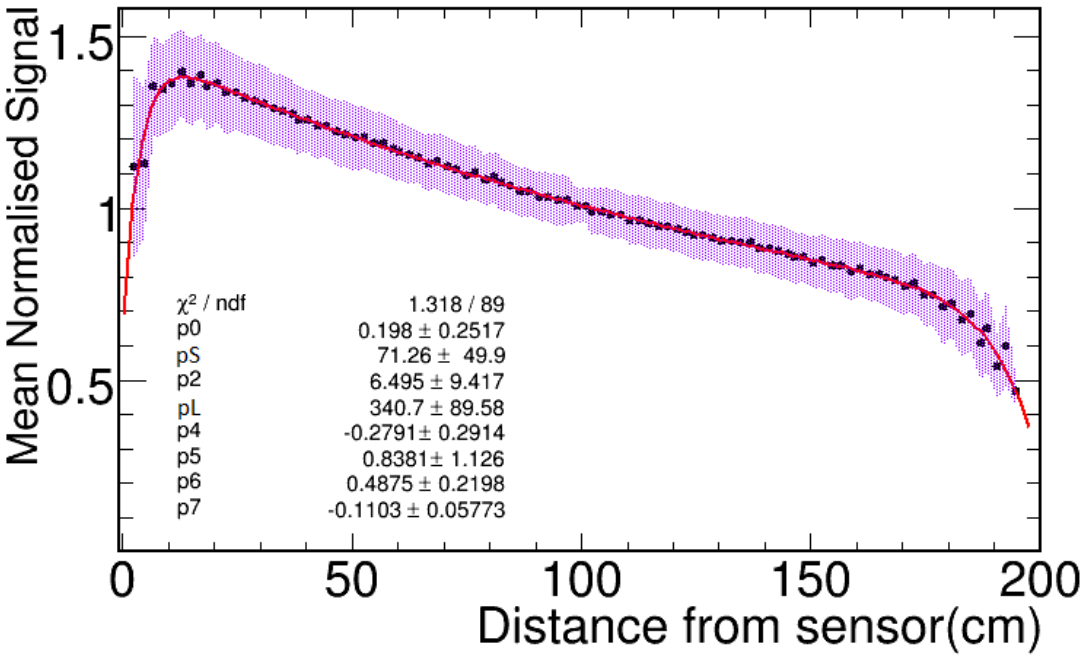

Fig. 8.17. Mean attenuation profile for all channels combined using CERN CR data. The DS-ECal is 'folded' into one bar by plotting the mean of a Gaussian distribution of the MPV's at each position along all bars combined. The profile is fit with a quadruple-exponential function to parameterise the attenuation of the bars. The error on the mean MPV's is represented by an error band.

global fit with the quadruple function calculates the short and long attenuation lengths (pL and pS) to be 71.26 ± 49.9 and 340.7 ± 89.58 respectively. These values are consistent with the expected values of approximately of 70 cm and 350 cm for the short and long attenuation lengths respectively.

The step function in Figure 8.18 arises from the separation of the mean MPV contribution of the sensors at opposing ends of each bar. The pixel position definition leads to an offset of

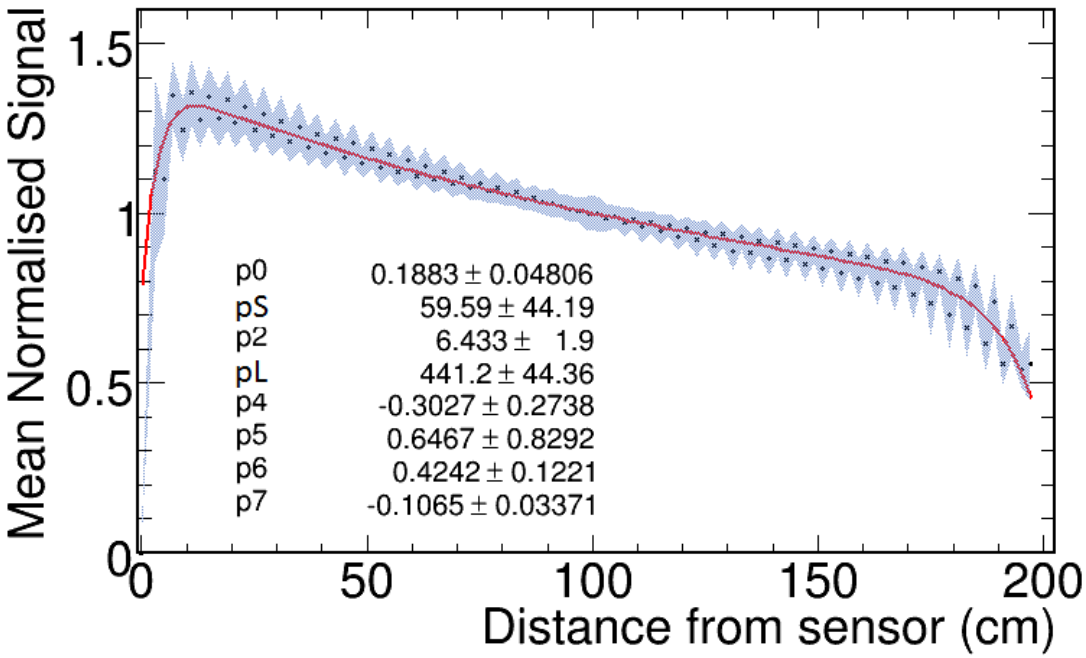

Fig. 8.18. Mean attenuation profile for all channels combined using Tokai CR data.The DS-ECal is 'folded' into one bar by plotting the mean of a Gaussian distribution of the MPV's at each position along all bars combined. The profile is fit with a quadruple-exponential function to parameterise the attenuation of the bars. The error on the mean MPV's is represented by an error band.

2 cm in the position reconstructed at each point along the bar when comparing sensor readouts from each end of the bar. This contribution from both ends should be consistent and this is the case using the CERN CR data. Figure 8.17 shows that the the opposing sensor ends are consistent across all channels, however Figure 8.18 has a step function introduced that has an effect on the overall quadruple-exponential fit and the values determined for the fit parameters. The cause of this step function is as yet undetermined and further work is required to use the Tokai CR data.

The quadruple exponential fit parameters, as determined using the CERN CR data, from the fit of the attenuation profile in Figure 8.17, was consequently applied to the attenuation profiles for each channel and a distribution of chi-squared/NDF was calculated. The chi-squared/NDF distribution is shown in Figure 8.19. The mean of a Gaussian distribution of the chi-squared/NDF

values determines a mean of 11.28 ± 0.39 which highlights the level of consistency within uncertainties of the attenuation of all bars.

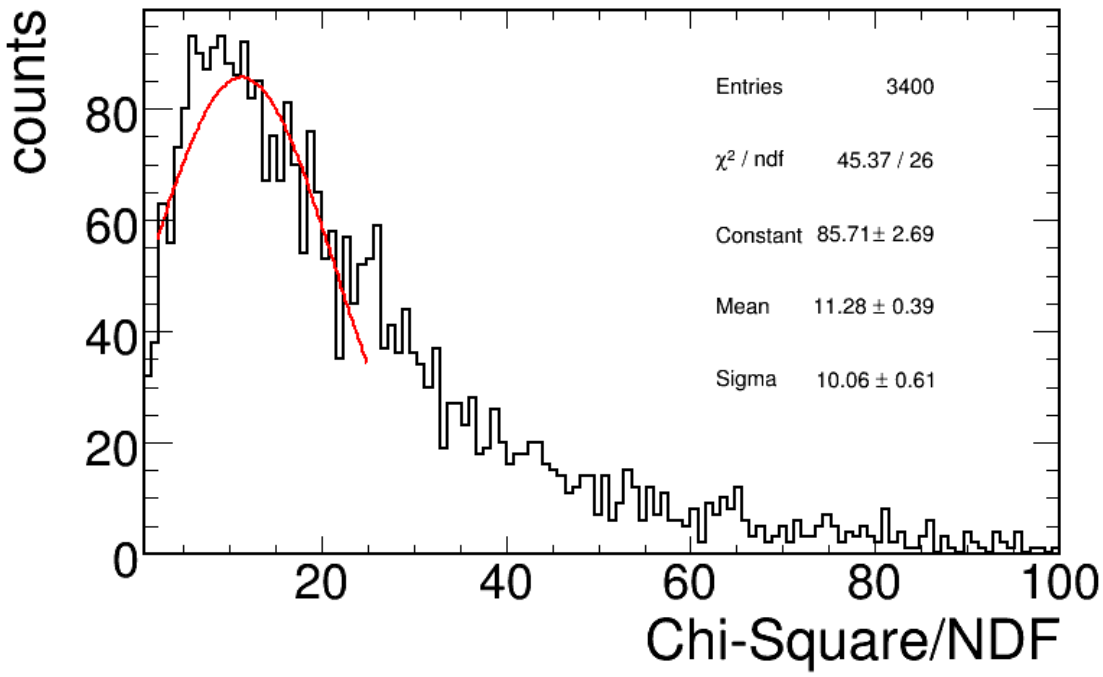

Fig. 8.19. Chi-square distribution from a quadruple-exponential fit to the attenuation profile for each channel. The 3400 entries represent one entry for each sensor readout of the DS-ECal.

Figure 8.20 shows the attenuation profiles from each sensor read out of one bar with the global quadruple-exponential function fit to the data to highlight the extent to which it parameterises the attenuation for one bar. The normalisation parameter, P_0 is the only free parameter of the quadruple-exponential function that was fit for each normalised attenuation profile, then the chi-squared/NDF distribution in Figure 8.19 was found. This led to some normalisation effect questions since the quadruple exponential function was modified slightly so that was allowed to run free so that it is self-normalising to each attenuation profile. Nevertheless the fit is remarkably good and the MPV distributions suggest that the bar-to-bar data are consistent so that one set of parameters can be applied for the attenuation correction factor. As a final remark,

the global quadruple-exponential fit parameters are used in order to correct for the charge, as detailed in Equation 8.3, to produce a normalised charge corrected distribution as shown in Figure 8.21. The sensor is at the left of the histogram. The data was expected to be corrected to a nominal value of 1 normalised PEU across the length of the bar. This demonstrates that the attenuation correction factor can be determined by a global quadruple-exponential fit to produce one set of parameters that can be used to calibrate all channels. The attenuation correction factor enables the charge at each position along the bar to be consistent to the order of ± 10%.

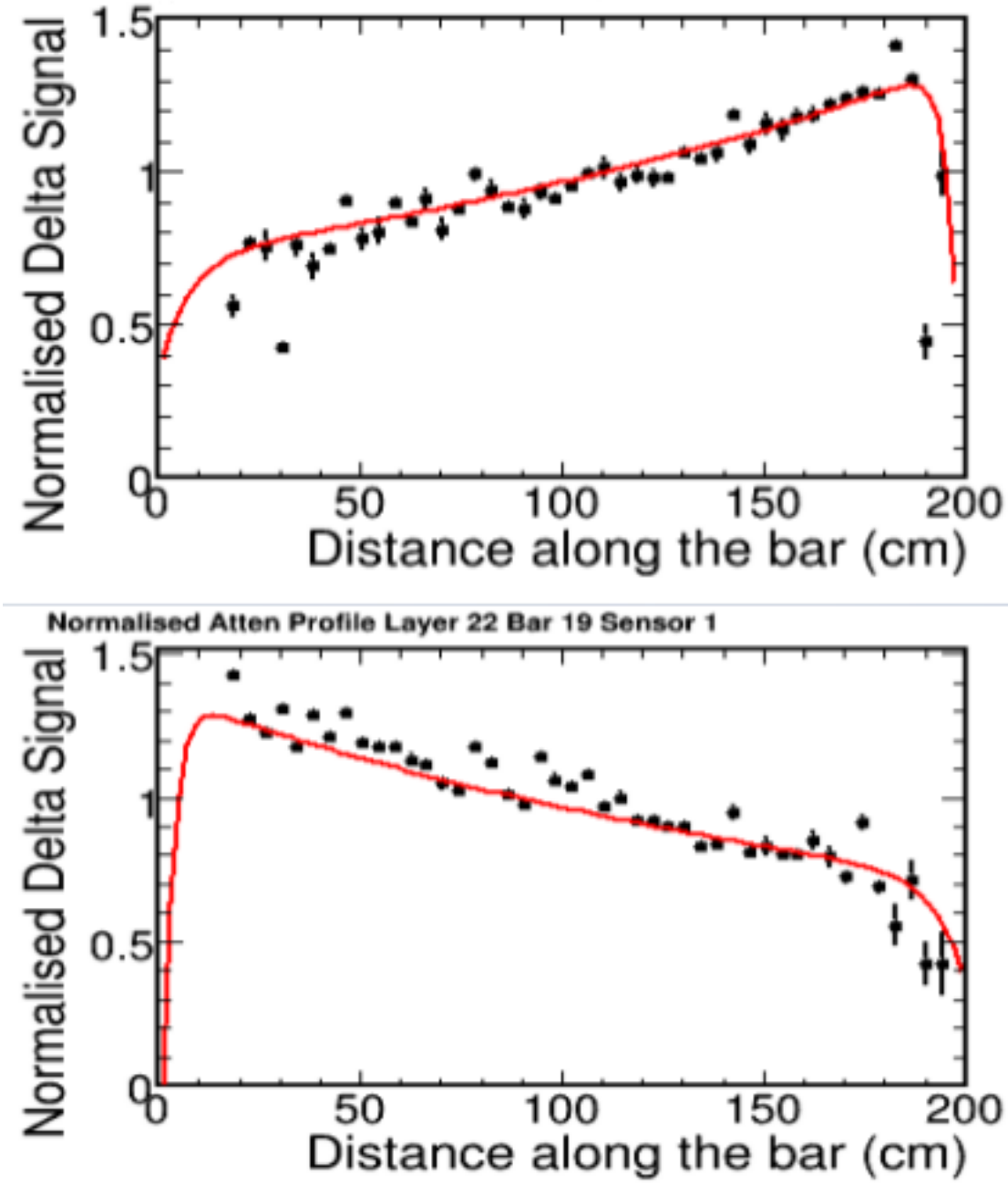

Fig. 8.20. The global quadruple-exponential function fit to the attenuation profiles from both ends of a scintillator bar.

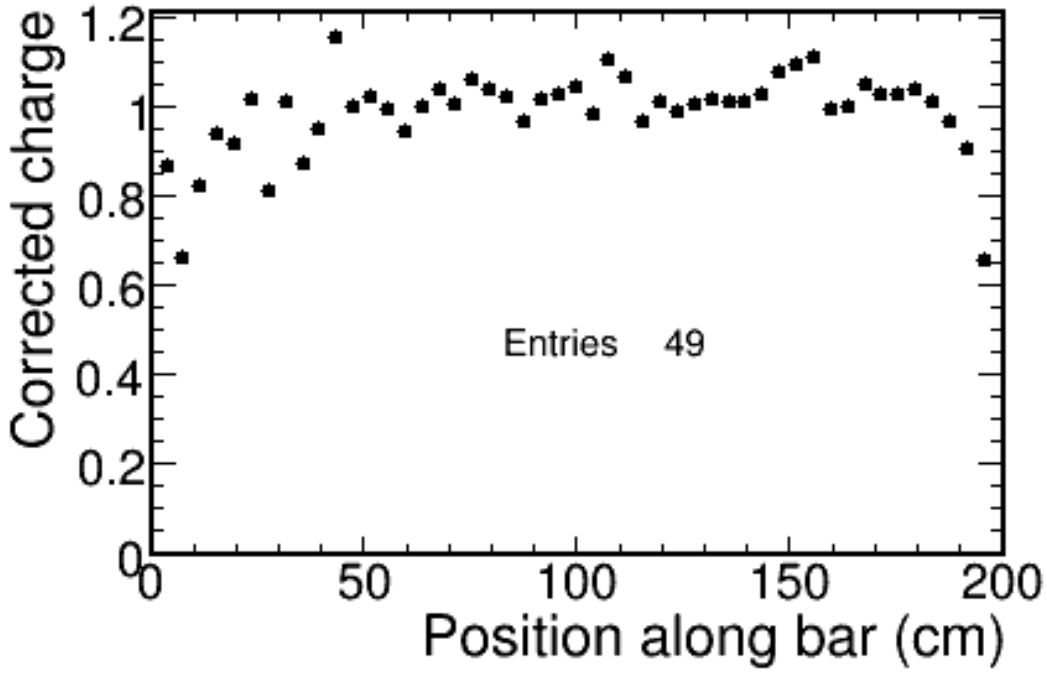

Fig. 8.21. Charge corrected profile using quadruple-exponential attenuation correction factor. The attenuation correction factor, including the path-length correction, as determined by the quadruple-exponential fit parameters, is applied to charge data for one channel. This profile is produced by using CERN CR data.

Chapter 9

Conclusion

This thesis has described some of the key steps required in order to successfully build, commission and understand an Electromagnetic Calorimeter. It may have ended with the complete parameterisation of an attenuation correction factor but without each of the steps this could not be accomplished. From the outset the focus has been on calibrating the detector in order to contribute to an improved energy reconstruction and consequently resolution. By achieving this the DS-ECal will be able to aid the measurement of the flux and energy spectrum of the ν_μ and ν_e neutrinos that interact in the ND280 detector. The neutrino flavours are reconstructed from charged lepton products in CCQE interactions in both the near and far detectors.

In Chapter 5 I outline the optical quality assurance method and results that I achieved. The optical quality assurance of the scintillator bars produced a baseline light yield per MIP of 25 PE/MIP which all tested bars successfully surpassed and hence were selected for production of the DS-ECal. The mean light yield of the tested bars was measured to be 35.9 ± 4.9 PE/MIP measured 66 cm along the 2 m bars with three-fibres coupled to a PMT readout. The optical QA tests successfully demonstrated the consistency of the light yield of the scintillator bars.

I described the subsequent construction of the DS-ECal including the optically QA'd bars in the scintillator layers. I was involved in all aspects of the construction, from defining procedures, threading WLS fibres through the central holes of the scintillator and cabling electronics to the module. I contributed from the start to the finish of the construction of the completed DS-ECal module which really allowed me to see the complete picture. The ability to be able to calculate the ECal eventual response to MIPs really does rely on scanning each of the completed layers and checking the integrity of the fibre coupling to the MPPC which is what I outlined in

Chapter 6. Chapter 6 also introduced the attenuation profile of the scintillator bar and the first attempt to parameterise the attenuation.

Chapter 7 described the commissioning setup at CERN where the DS-ECal collected testbeam data and, more importantly for this thesis, cosmic ray data. My contribution to the testbeam commissioning was to produce hit maps such that hot channels and 'dead' channels could be quickly identified. The hit maps also serve their purpose in checking the distribution of charge hits. Chapter 8 described the calibration chain required in order to achieve that the mean energy deposit per unit path length for all detector channels is the same. The attenuation correction is a second stage effect that needs to be calculated and applied to the ECal data. I presented a simple track-reconstruction algorithm that allowed the reconstruction of the position of charge deposits in the DS-ECal, with which an attenuation profile could be produced for each sensor readout channel. The attenuation has been parameterised with a single function allowing one to use one set of parameters in order to describe the attenuation correction factor. The calculated fit parameters describing the quadruple-exponential function

$$A(x) = P_0 \left[e^{\left(\frac{x}{P_1}\right)} + P_2 * e^{\left(\frac{x}{P_3}\right)} \right] - P_4 * e^{(P_5 * x)} - P_6 * e^{(P_7 * [200 - x])},$$

where x is the distance between the hit position and the MPPC readout, are listed in Table 9.

I demonstrated that the Tokai and CERN cosmic ray datasets are consistent within approximately 1% as calculated for each mean MPV value at positions along the bar for all channels combined. As such this confirms that the algorithms developed on the CERN data also can be used on the Tokai data. The other 12 ECal modules also need to be calibrated for attenuation effects. The reconstruction algorithm and method of calculating the attenuation correction parameters, developed in this thesis work, will form an integral part of that future work.

Fit Parameter	Value and Error
P_0	0.198 ± 0.258
$P_1 = P_S$	71.26 ± 49.90
P_2	6.495 ± 9.417
$P_3 = P_L$	340.7 ± 89.58
P_4	-0.279 ± 0.291
P_5	0.8381 ± 1.126
P_6	0.488 ± 0.220
P_7	-0.111 ± 0.0577

Table 9.1. Fit parameters describing the quadruple-exponential function. The function parameterises the attenuation profile for each sensor readout channel. Parameters P_S and P_L are the short and long attenation lengths respectively.

In conclusion, the work outlined throughout this thesis will ultimately contribute to the measurement of θ_{13} by the T2K experiment. We need to be able to understand the neutrino energy spectrum at SK with a precision of approximately 10%. This means that we need to measure the unoscillated neutrino spectrum at the ND280 with a precision of better than 10%. The energy resolution provided by the ECal plays an important role in the ND280 off-axis detector supporting the energy measurements made by the TPCs for charged particles, and providing an energy measurement for neutral particles.

Appendix A

Mechanical QA

The scintillator bars of the DS-ECal are high-quality extruded plastic scintillator bars with a rectangular cross-section of 10mm x 40mm. Table A states the scintillator bar mechanical parameters and tolerances for bars produced at FNAL for the DS-ECal.

Width (mm)	Height (mm)	Length (mm)	Flatness Tolerance (mm)	Squareness Tolerance (mm)	Corner Rmax (mm)	Hole Diameter (mm)	Hole Position (mm)
$40^{+0.0}_{-0.4}$	$10^{+0.0}_{-0.4}$	2035±5	±0.5	±0.5	0.75	1.8 to 2.2	±0.5

Table A.1. Scintillator bar parameters and tolerances

All bars were checked for the specified physical parameters within the tolerances requested except for the length. The bars were several mm longer than necessary and then cut to length at Lancaster. Each bar was given a "barcode" and identification number in the format T2K##### (e.g. T2K13456). In total, three crates of scintillator bars for the DS-ECal were received, each with bars from different extrusion production runs. The properties of the bars varied slightly from run-to-run.

A.1 Crate 1

We initially received the first crate of bars, Crate 1, in March 2008. Crate 1 contained 306 bars from FNAL's November 2007 production run. Firstly, the bars were checked for width and thickness using custom-made Go and No-Go gauges that could slide easily along bars, as shown in Figure A.1. The bars were then cut to length at Lancaster. The bars needed to measure 2016 mm in order to fit inside the aluminium frames used to construct the layers of the DS-ECal.

Also, the hole size was checked on 10% of the bars using digital calipers. A visual inspection for flatness and squareness of the bars was made whilst the bar sat in a metal angle piece on the QA bench. This is shown in Figure A.2.

Fig. A.1. Using a custom-made Go- No-Go gauge that slides along the scintillator bars to check the width and thickness of the bars.

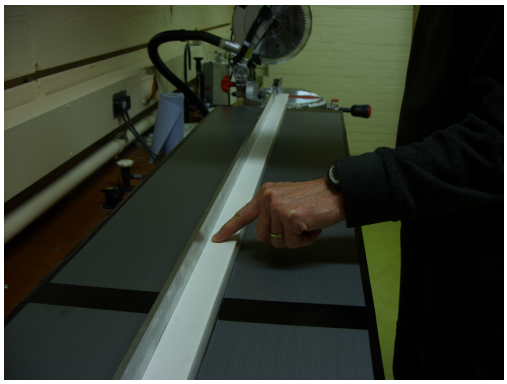

Fig. A.2. A scintillator bar in place along a metal angle piece on the QA bench for visual inspection. Flatness and squareness can be checked visually against the metal trough and the bars can then be cut to the required length of 2016mm to fit in the layer build frame of the DS-ECal.

It soon was noticed that there was a large variation in the hole diameters. The hole diameter was a concern because we needed to make sure that a metal locator pin that was pointed at its tip and then tapered up to 1.6 mm could fit inside the hole so that the bar could be fixed in place during the layer-building phase. If the hole was too small, this would mean that the bar could not be fixed in position in the layer, and if the hole was too big glue would get into the middle of the bar, preventing the subsequent insertion of the WLS fibres. As a result the hole diameter was measured for all of the received bars. In order to assist with the QA of subsequent bars which were still being produced and which would be shipped later in Crates 2 and 3, FNAL sent 300 mm-long offcut bars with hole diameters written on them. The offcut bars were bars cut periodically from sections of the current bars being produced at FNAL. It should also be noted that the holes were found to be not circular, but rather more elliptical in shape, with the minor axis parallel to the 40 mm axis of the bar, and the major axis parallel to the 10 mm axis of

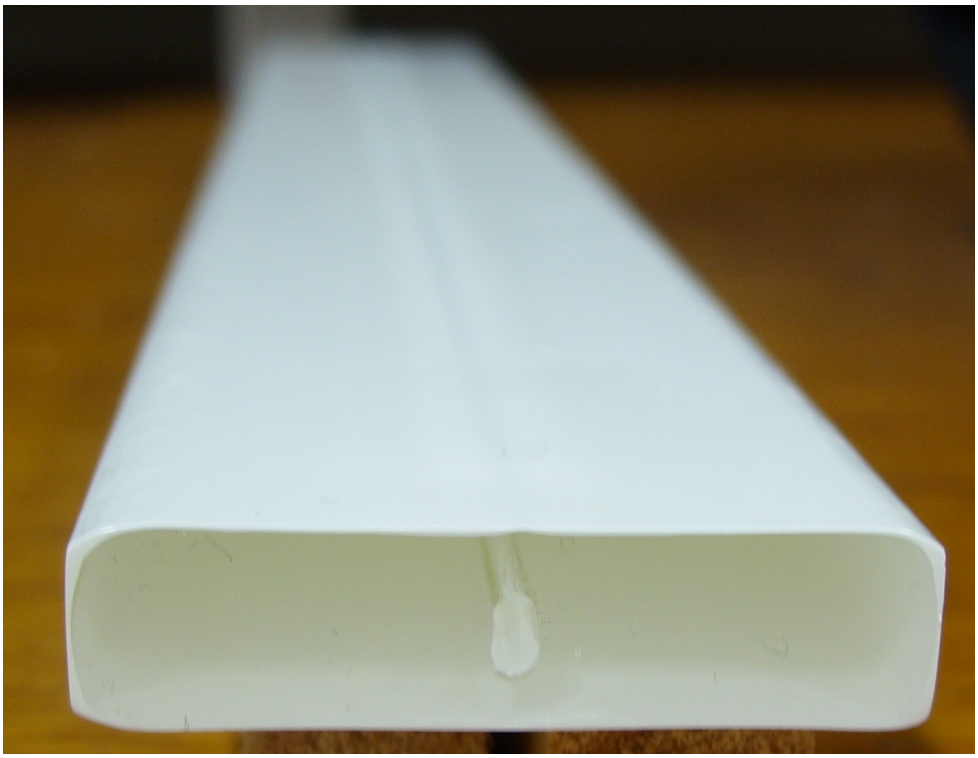

Fig. A.3. Picture of a scintillator bar's elliptical central hole. This highlights the extent to which the holes are elliptical as opposed to circular.

the bar. Due to limitations in the preparation of the extrusion die this was the best that could be achieved by the extrusion process. Figure A.3 shows the elliptical hole shape of a typical bar.

Figure A.4 shows the distribution of hole diameter versus bar ID number of the scintillator bars produced by FNAL in November 2007 and shipped in Crate 1. The average hole diameter measured parallel to the 40 mm bar axis and a 2σ acceptance (upper and lower) is shown. Hole sizes were accepted in the range 2.0 mm $\leq x \leq$ 3.0 mm. Note that the hole size was measured on only one end of each bar here.

The apparent fluctuation in Figure A.4 of hole diameter versus scintillator bar ID was explained by FNAL as a tuning process with the time/production sequence flowing from right to left; that is to say, the better the tuning the more consistent the diameter of the hole. This implies that for this crate of bars, the bars produced last were labeled first and hence have lower ID numbers.

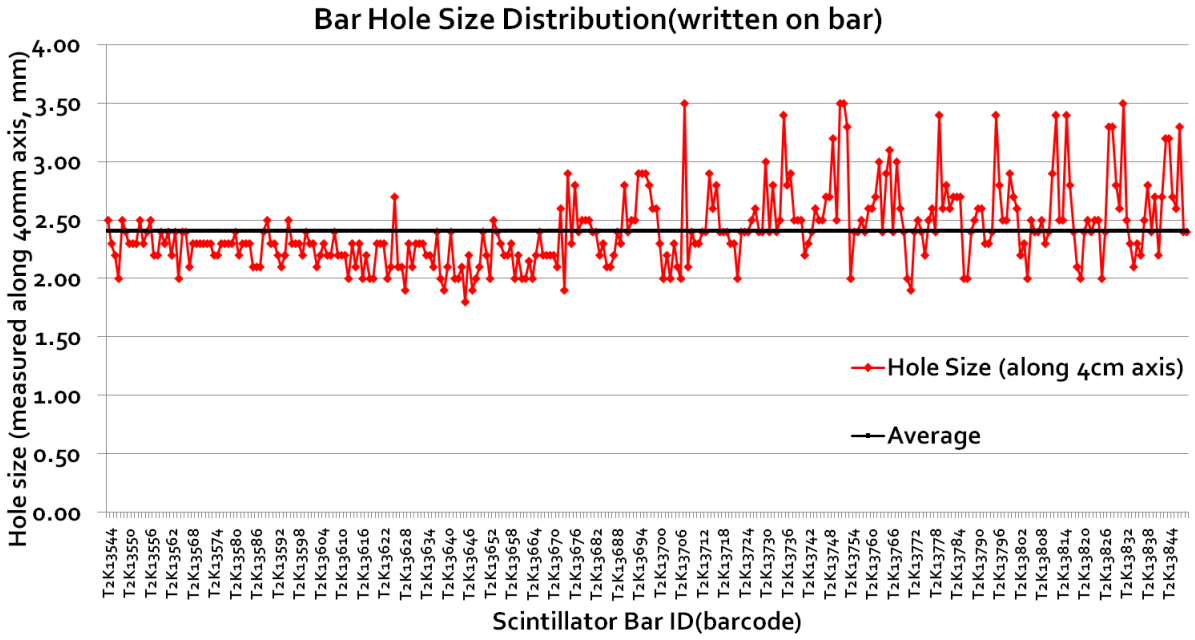

Fig. A.4. Bar hole diameter distribution versus Bar ID for bars from Crate 1, produced in November 2007 (red line). The hole diameters are measured along the 40 mm bar axis, on one end of each bar. A mean bar hole diameter of 2.47 mm is shown (black line) and a 2σ acceptance (upper and lower - dashed lines) is also shown. These bars correspond to the first 300+ bars that were used for the first five layers to be built for the DS-ECal, which then were used as Layers 30 - 34 in the DS-ECal module, corresponding to the far-downstream layers.

A.2 Crates 2 and 3

We received Crates 2 and 3 in April 2008. They each contained approximately 850 bars from FNAL's March 2008 production runs and a combined total of 45 300mm-long offcut bars. For Crate 2, the information of the hole diameters from the offcut bars showed good consistency indicating that we could measure the hole diameters for 5% of the bars rather than for all of the bars. For Crate 3, the QA process was adjusted such that we measured the hole diameters for 100% of the bars due to a number of offcuts in that Crate which had a significant discrepancy in hole diameters on opposite ends of the bar.

Figure A.5 shows the average hole diameter for each bar from Crate 3. It was possible to group the bars from Crate 3 into production days using the information on the offcut bars. In the figure, hole size L or R refers to the end of the bar on which the hole was measured; where L

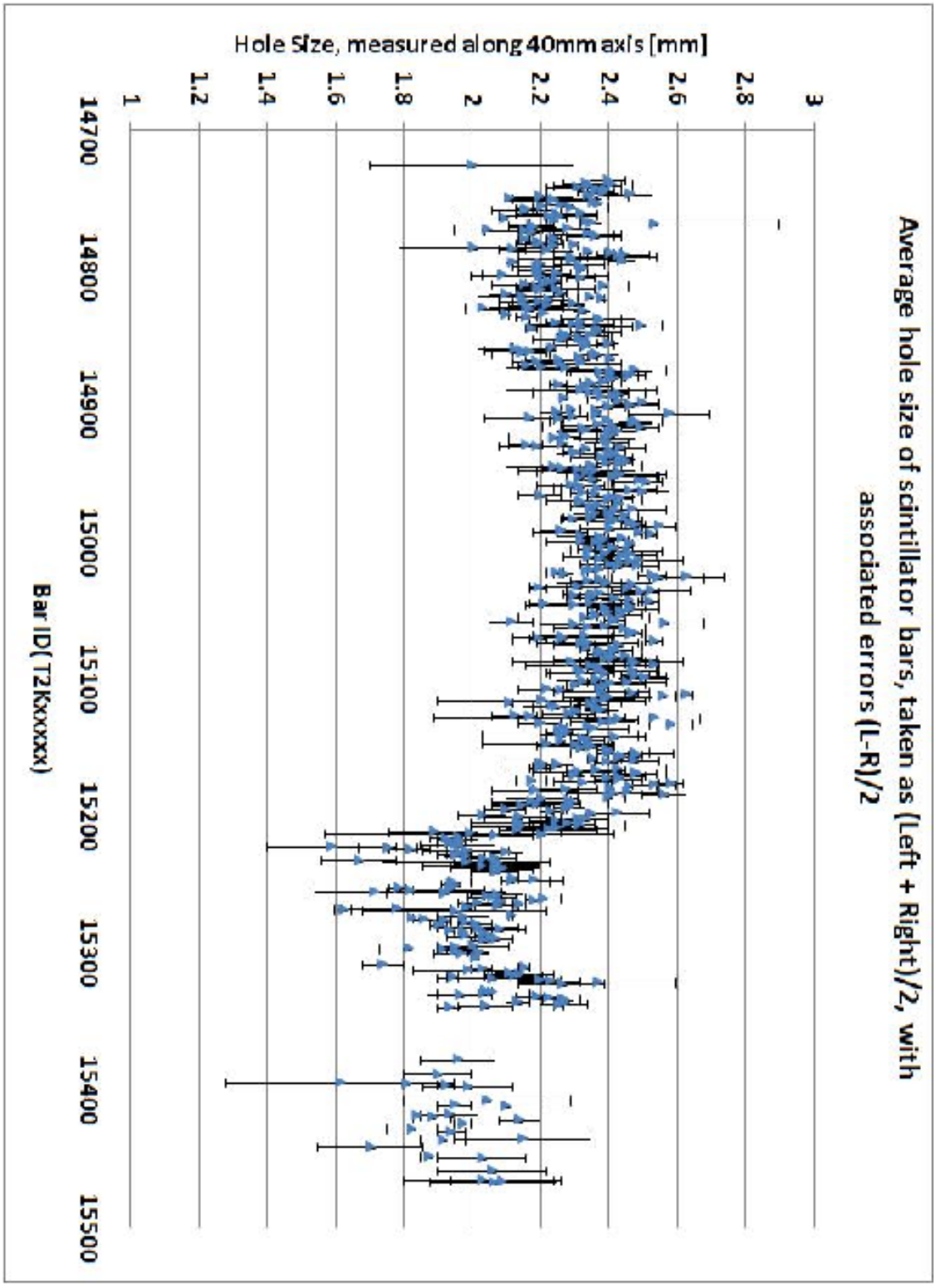

Fig. A.5. Average of left and right hole diameters, computed as (left + right)/2, versus bar ID, for bars from Crate 3. The error is recorded as ± (L-R)/2. This shows that the hole diameter varies significantly from the left end to the right end. Also shown are several bars QA'd by FNAL (pink triangles) and hole diameters, left and right, for 300 mm-long offcut bars (orange and black triangles respectively. These bars were used to build 14 layers, corresponding to layers 1 -13, the upstream layers in the DS-ECal.

= left, R = right. In this case, the average hole size per bar is computed as (L+R)/2 with error ± (L-R)/2. The length of the error bars thus represent the difference between the left and right hole diameters for each of the 2 m bars. There is no way of knowing the hole diameter in the middle of the bar. It can clearly be seen, however, that the hole diameter often does vary significantly from one end to the other. In cases where the offcuts showed significant differences between hole diameters measured at each end, it is assumed that the extrusion process was not stable. Also shown in Figure A.5 are a few hole diameter measurements sent by FNAL. In some cases the variation from the mean hole diameter of all bars reaches ±0.5 mm, and the difference between left and right measurements of 2 m bars is large, implying that during the extrusion there may have been stress on the bar, for example caused by a sudden change in extrusion rate. Several bars have a hole diameter difference over the 2 m length of greater than 0.4 mm. Most bars fall within a difference left-to-right of 0.2 mm.

The values in Table A.2 were obtained for bars from Crates 2 and 3, specifically those bars produced on 11th, 12th and 17th March 2008 as determined from the offcut bars received. Any bars that fell within the barcode ID from one offcut to the next were assigned the same production date. For example, if offcut bars with ID T2K14546 and T2K14560 were produced on the 11th March then all production bars with ID numbers between these numbers in the sequence were assumed to be produced the same day. In order to obtain some statistical understanding of the hole diameters, we define Δx = hole diameter difference (mm) for a particular bar left-to-right and $<|\Delta x|>$ = mean hole diameter difference (mm).

Data Set	# of bars	$< \lvert\Delta x\rvert >$	Δx_{Max}	Δx_{Median}
11th March	33	0.277 ± 0.183	0.700 ± 0.005	0.240
12th March	346	0.133 ± 0.099	0.730 ± 0.005	0.110
17th March	240	0.155 ± 0.130	0.850 ± 0.005	0.130
Entire Set	619	0.150 ± 0.122	0.850 ± 0.005	0.120

Table A.2. Measurements of bars from Crates 2 and 3 produced 11th, 12th and 17th March 2008. This table only includes bars where the hole diameters were measured on both ends.

Table A.2 records measurements of the mean bar hole diameter difference left-to-right for bars produced on March 11th, 12th and 17th, as well as the maximum difference, median difference and their associated errors. The table also combines the measurements for a total mean across the time period. Measurements on March 11th have a much larger mean hole diameter difference from one end of the bar in comparison to the other two days, although the data set is sparse with as much as 10 times less statistics than March 12th. A significant number to note is the maximum hole diameter difference of 0.850 mm. This is the most extreme difference between the hole diameters measured on the left and right ends of a bar. This is a bar that would not pass the Mechanical QA process. The left and right hole diameters for all of the 2m bars used in layer production, and for the offcut bars from FNAL, are plotted on Figure A.6. Dates the bar were produced, and which layer of the DS-ECal they were used in, is also shown. Data furthest to the left is for the November bars (Crate 1) presented in Figure A.4. The shaded regions show data from corresponding scintillator production run dates. The hole diameters measured on bars from Crate 2 are seen in the middle of the plot where data is sparse as a result of measuring only 5% of hole diameters for bars from this Crate. Fewer checks were performed on these bars due to knowledge obtained from the offcuts received from FNAL which indicated that the extrusion was stable. Only when the hole was too small for the aforementioned tapered metal locator pin to fit was the diameter recorded for Crate 2. The bars for the final 14 layers constructed are from Crate 3. The data seen here for bars from this crate is the same as seen in Figure A.5. It is shown again so that all the data can be seen together for comparison.

In Figure A.7, the entire data set of left and right hole diameter differences measured parallel to the 40 mm axis is represented with a frequency distribution with a bin width of 0.05 mm. A Gaussian fit was then applied in order to obtain a standard deviation of $\sigma = 0.167$ mm. This indicates that for most bars the difference in hole size between the left and right ends is less than 0.167 mm.

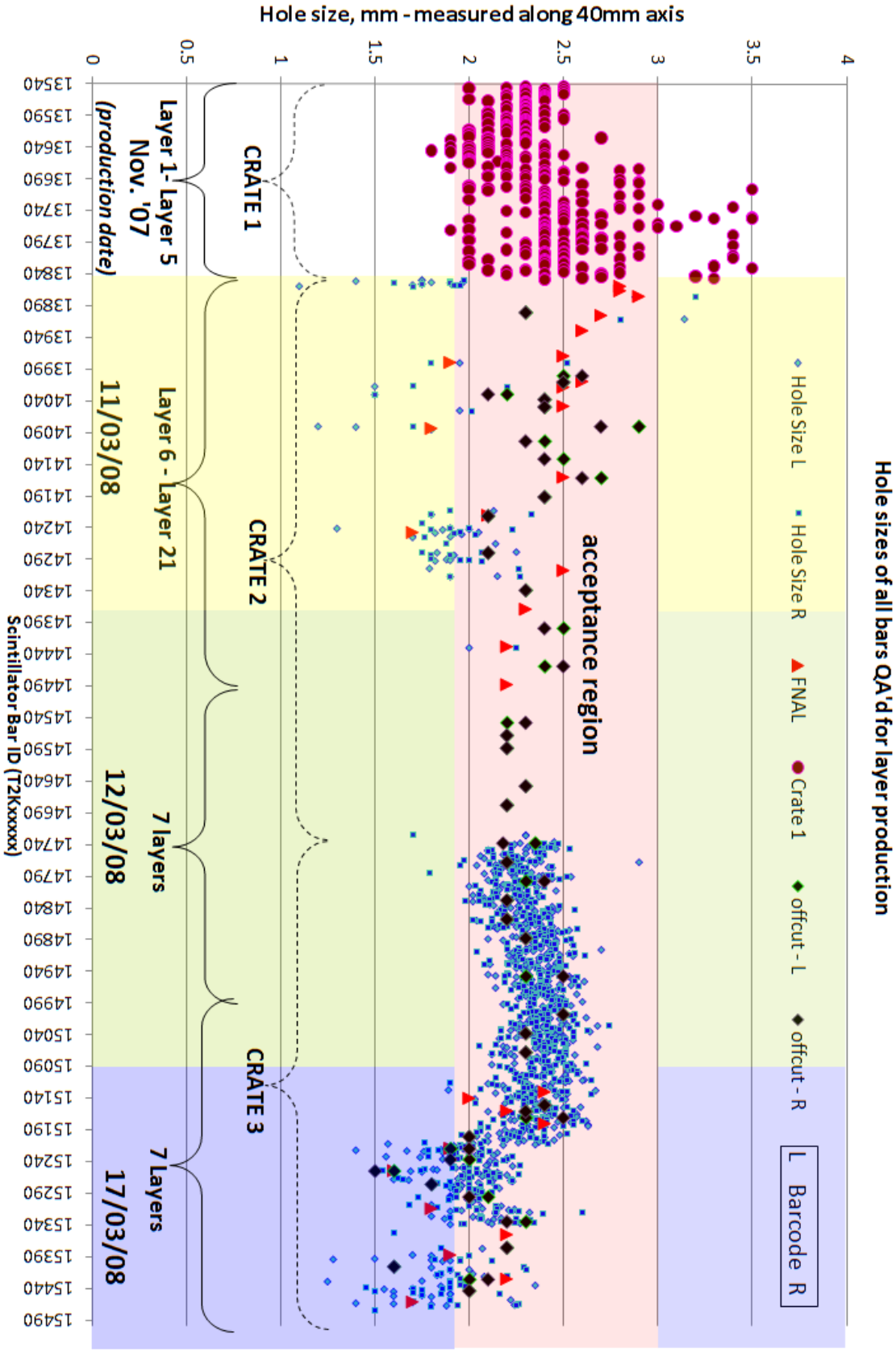

Fig. A.6. Hole diameter versus bar ID for all bars received from FNAL. Hole diameters are measured parallel to the 40 mm axis of the bar. Included are offcut bar measurements (diamonds) and some QA'd bars from FNAL (orange triangles). Also shown are the dates that the bars were produced and the DS-ECal layers they are contained within. The data show the relative stability of the extrusion process on different days. Data is sparse from Crate 2 because fewer bars from this crate were measured.

Using only bars that have both a left and right end measurement, the average hole diameter is 2.247 ± 0.4 mm. Given that we used bars with hole diameters ranging from 1.8 mm to 3.0mm, we accepted bars with -2σ and $+4\sigma$ of the mean. This highlights that it was more critical that the hole diameter was not too small because this had mechanical implications for the construction of a layer. It must also be added that most bars that were used lay within the -0σ to $+3\sigma$ range.

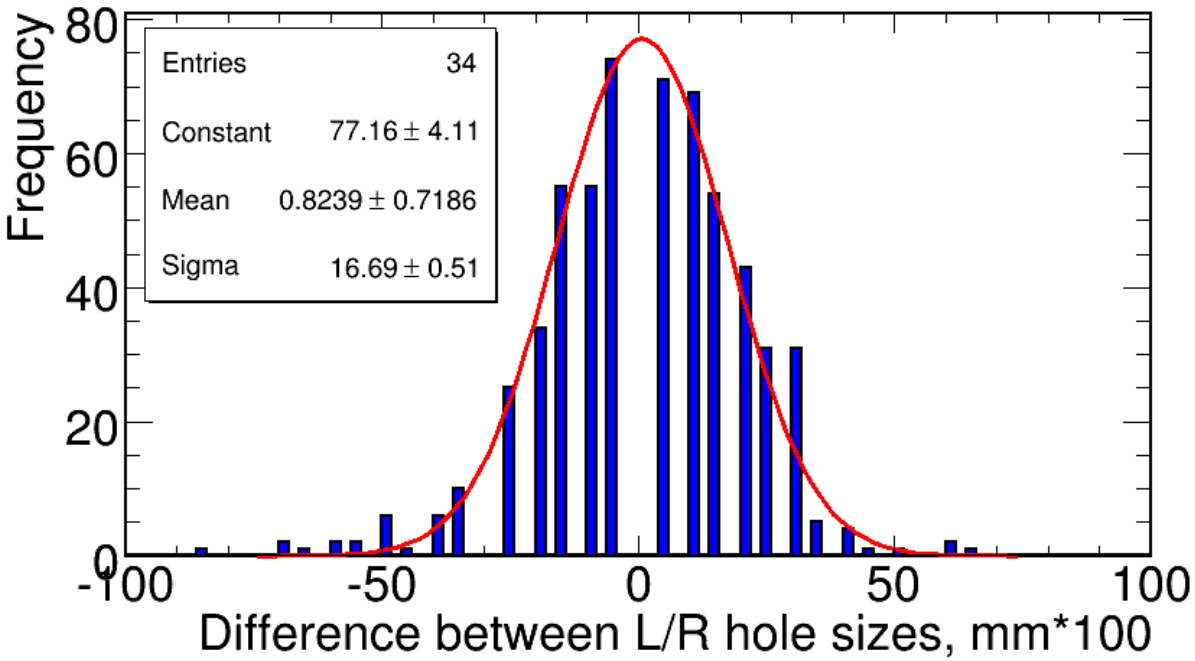

Fig. A.7. Frequency Distribution for March 2008 production bars, Crates 2 and 3. The difference between left and right end hole diameters is plotted in bins of 0.05 mm, where the plot multiplies all mm values by 100. The Gaussian fit obtains a standard deviation for the left and right hole diameter differences of σ = 0.167 mm.

When the original order for scintillator bars was placed, 10% more bars were ordered than were required. Taking into account the hole diameter deviations from the hole diameter requested in the specification this extra 10% was, in the end, imperative in order to be able to

complete construction of layers with bars that would be acceptable within tolerances chosen from the Mechanical QA process.

Figure A.8 is a frequency distribution of the average hole diameters that were computed using (L+R)/2. The data were plotted in bins of 0.05 mm in size from 1.40 to 3.10 mm. The data has two peaks, one with a mean of 2.38 ± 0.01 mm and a second with a mean of approximately 2.00 mm, as given by Gaussian fits. The two peaks in Figure A.8 clearly correspond to the data shown in Figure A.5, indicating a change in production conditions partway through the extrusion run of 17th March 2008.

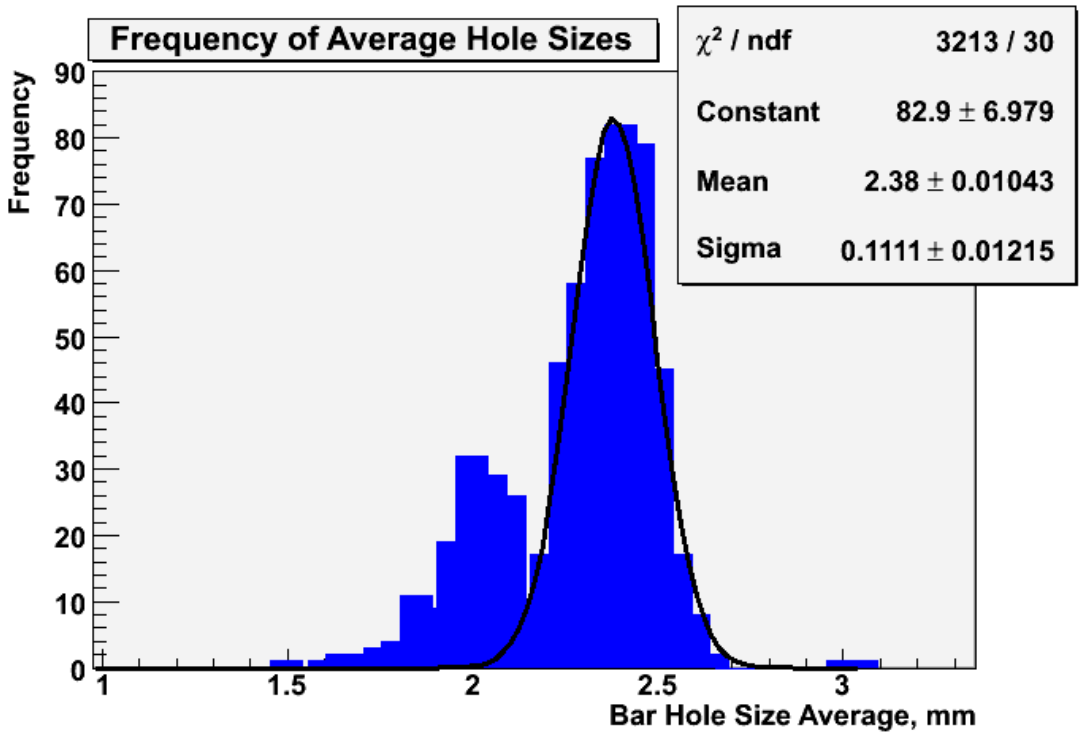

Fig. A.8. Frequency distribution of the bar hole diameter average, taken to be (left + right)/2. Data is plotted in bins of 0.05 mm. The data has two peaks, one with mean of 2.38 mm ± 0.01 mm and a second with a mean of approximately 2.00 mm, as given by Gaussian fits. The bimodal distribution indicates a likely change in the extrusion process.

Upon completion of the Mechanical QA sequence the total mechanical rejection rate was approximately 7%.

Bibliography

[1] W. Pauli. Dear radioactive ladies and gentlemen. *Phys. Today*, 31N9:27, 1978.

[2] J. Chadwick. Possible Existence of a Neutron. *Nature*, 129:312, 1932.

[3] E. Fermi. Trends to a Theory of beta Radiation. (In Italian). *Nuovo Cim.*, 11:1–19, 1934.

[4] Carl D. Anderson. The positive electron. *Phys. Rev.*, 43(6):491–494, Mar 1933.

[5] F. Reines and C. L .Cowan. The neutrino. *Nature*, 178:446–449, 1956.

[6] C. Giunti. Neutrino Flavour States and the Quantum Theory of Neutrino Oscillations. *AIP Conf. Proc.*, 1026:3–19, 2008. hep-ph/0801.0653.

[7] C. Amsler *e*t al. Particle data group. *Physics Letters*, B667:1–20. 2008 and 2009 partial update for the 2010 edition.

[8] B.R. Martin and G. Shaw. *Particle Physics*. John Wiley and Sons Ltd, 2008.

[9] C. S. Wu *et. al*. Experimental Test of Parity Conservation in Beta Decay. *Phys. Rev*, 105(4):1413–1415, 1957.

[10] L. M. Lederman R. L. Garwin and M. Weinrich. Observations of the Failure of Conservation of Parity and Charge Conjugation in Meson Decays: the Magnetic Moment of the Free Muon. *Phys. Rev*, 105(4):1415–1417, 1957.

[11] L. Grodzins M. Goldhaber and A. W. Sunyar. Helicity of Neutrinos. *Phys. Rev*, 109(103):1015–1017, 1958.

[12] G. S. Abrams *et. al*. Measurements of Z-boson resonance parameters in e^+e^- annihilation. *Phys. Rev. Lett.*, 63(20):2173–2176, 1989.

[13] D. DeCamp *et.al* ALEPH Collaboration. Determination of the number of light neutrino species. *Phys. Rev. Lett.*, 231(4):519–529, 1989.

[14] R. Wigmans. *Calorimetry: Energy Measurements in Particle Physics*. Oxford University Press, 2000.

[15] G. P. Zeller. Low energy neutrino cross sections from K2K, MiniBooNE, SciBooNE, and MINERvA. *J. Phys. Conf. Ser.*, 136:022028, 2008.

[16] R. Davis Jr. Report on the Homestake solar neutrino experiment. *Front. Phys.*, 5:47–60, 1993.

[17] N. A. Bahcall J. N. Bahcall and G. Shaviv. Present Status of the Theoretical Predictions for the ^{37}Cl Solar-Neutrino Experiment. *Phys. Rev. Lett.*, 20:1209–1212, 1968.

[18] D. S. Harmer R. Davis Jr. and K. C. Hoffman. Search for Neutrinos from the Sun. *Phys. Rev. Lett.*, 20(21):1205–1209, 1968.

[19] K. S. Hirata *et. al* Kamiokande-II Collaboration. Results from one thousand days of real-time, directional solar-neutrino data. *Phys. Rev. Lett.*, 65:1287–1300, 1990.

[20] K. Hirata *et. al*. Observation of ^{8}B Solar Neutrinos in the Kamiokande-II Detector. *Phys. Rev. Lett.*, 63:16, 1989.

[21] Y. Fukuda *et. al*. Solar Neutrino Data Covering Solar Cycle 22. *Phys. Rev. Lett.*, 77(9):1683–1686, 1996.

[22] P. Anselmann *et. al*. *Phys. Lett. B*, 285:376, 1992.

[23] D. N. Aburashitov *et. al*. *Phys. Lett. B*, 328:234, 1994.

[24] M. Altmann *et. al* GNO Collaboration. *Phys. Lett. B*, 616:174, 2005. hep-ex/0504037.

[25] C. Arpesella *et. al* Borexino Collaboration. *Phys. Rev. Lett.*, 101:091302, 2008. arXiv:0805.3843.

[26] Y. Fukuda *et. al* SUPER-KAMIOKANDE Collaboration. Evidence for Oscillation of Atmospheric Neutrinos. *Phys. Rev. Lett.*, 81(8):1562–1567, 1998.

[27] Q. R. Ahmad *et. al* SNO Collaboration. Measurement of the Rate of $\nu_e + d \rightarrow p + p + e^-$ Interactions Produced by ^8B Solar Neutrinos at the Sudbury Neutrino Observatory. *Phys. Rev. Lett.*, 87(7):071301, 2001.

[28] T. J. Haines *et. al*. Calculation of Atmospheric Neutrino-Induced Backgrounds in a Nucleon-Decay Search. *Phys. Rev. Lett.*, 57(16):1986–1989, 1986.

[29] K2K Collaboration. *Phys. Rev. Lett.*, 94:081801, 2005.

[30] Y. Oyama K2K Collaboration. K2K (KEK to Kamioka) neutrino oscillation experiment at KEK-PS. hep-ex/9803014.

[31] S. Eliezer and A.R. Swift. Experimental Consequences of ν_e-ν_μ Mixing in Neutrino Beams. *Nucl. Phys.*, B105:45, 1976.

[32] H. Fritzsch and P. Minkowski. Vector-Like Weak Currents, Massive Neutrinos and Neutrino Beam Oscillations. *Phys. Lett.*, B62:72, 1976.

[33] S.M. Bilenky and B. Pontecorvo. *Sov. J. Nucl. Phys.*, 24:316–319, 1976.

[34] S.M. Bilenky and B. Pontecorvo. *Nuovo Cim. Lett.*, 17:569, 1976.

[35] R.D. Peccei. Neutrino Physics. *AIP Conf. Proc.*, 490:80–124, 1999. hep-ph/9906509v1.

[36] C. Giunti and C. W. Kim. *Fundamentals of Neutrino Physics and Astrophysics*. Oxford University Press, 2007.

[37] COBRA Collaboration. *Phys. Rev. Lett.*, C76:025501, 2007.

[38] CUORICINO Collaboration. *Phys. Rev. Lett.*, C78:035502, 2008.

[39] IGEX Collaboration. *Phys. Rev. Lett.*, D65:092007, 2002.

[40] NEMO Collaboration. *Phys. Rev. Lett.*, C80:032501, 2009.

[41] A. M. Bakalyarov, A. Y. Balysh, S. T. Belyaev, V. I. Lebedev, and S. V Zhukov. *Phys. Part. Nucl. Lett.*, 2:77–81, 2005.

[42] A. Aguilar et al. Evidence for neutrino oscillations from the observation of $\overline{\nu}_e$ appearance in a $\overline{\nu}_\mu$ beam. *Phys. Rev.*, D64:112007, 2001.

[43] E.D.Church *et. al.* Statistical analysis of different $\overline{\nu}_\mu \rightarrow \overline{\nu}_e$ searches. *Phys. Rev.*, D66:013001, 2002.

[44] P. Astier et al. Search for $\nu_\mu \rightarrow \nu_e$ oscillations in the NOMAD experiment. *Phys. Lett.*, B570:19–31, 2003.

[45] A.A. Aguilar-Arevalo et al. A Search for electron neutrino appearance at the $\Delta m^2 \sim 1$ eV^2 scale. *Phys. Rev. Lett.*, 98:231801, 2007.

[46] S. Abe et al. Precision Measurement of Neutrino Oscillation Parameters with KamLAND. *Phys. Rev. Lett.*, 100:221803, 2008.

[47] MINOS Collaboration. *Phys. Rev. Lett.*, 101:131802, 2008.

[48] NOνA Collaboration. 2004. arXiv hep-ex/0503053.

[49] ND280 Collaboration. Document for ND280 review. 2006. Internal Document.

[50] T. Schwetz, M. A.Tortola, and J. W. F. Valle. Three-flavour neutrino oscillation update. *New J. Phys.*, 10:113011, 2008.

[51] M. Apollonio et al. Search for neutrino oscillations on a long base-line at the CHOOZ nuclear power station. *Eur. Phys. J.*, C27:331–374, 2003.

[52] S. Boyd. Cross-section Measurements in the T2K ND280 Detector, 2009. Presented at the WIN09 22nd International Workshop on Weak Interactions and Neutrinos.

[53] A. D. Marino. Status of the T2K experiment. *AIP Conf. Proc.*, 1182:80–83, 2009.

[54] GEANT: Detector Description and Simulation Toolkit. CERN Programming Library Long Writeup W5013, GEANT version 3.21.

[55] S. Agostinelli et al. GEANT4: A simulation toolkit. *Nucl. Instrum. Meth.*, A506:250–303, 2003.

[56] Magdalena Posiadala. Status of the NA61 (SHINE) experiment at CERN. 2009.

[57] C. Blume. Recent results from the NA49 experiment. Prepared for 18th International Conference on Particles and Nuclei (PANIC 08), Eilat, Israel, 9-14 Nov 2008.

[58] M. Otani et al. Design and construction of INGRID neutrino beam monitor for T2K neutrino experiment. *Nucl. Instrum. Meth.*, A623:368–370, 2010.

[59] R. Tacik. The T2K fine-grained detectors. *Nucl. Instrum. Meth.*, A623:309–311, 2010.

[60] Dean Karlen. Time projection chambers for the T2K experiment. *Nucl. Instrum. Meth.*, A623:108–110, 2010.

[61] A. Izmaylov et al. Scintillator counters with WLS fiber/MPPC readout for the side muon range detector (SMRD) of the T2K experiment. *Nucl. Instrum. Meth.*, A623:382–384, 2010.

[62] A. D. Bross A. Pla-Dalmau and V. V. Ryalkin. Extruding plastic scintillator at Fermilab. FERMILAB-CONF-03-318-E.

[63] J. B. Birks. Scintillators from Organic Crystals: Specific Fluorescence and Relative Response to Different Radiations. *Proc. Phys Soc.*, A64(10):874–877, 1951.

[64] M. Hirschberg *et. al*. Precise measurement of Birks k_B parameter in plastic scintillators. *IEEE Trans. Nucl. Sci.*, 39:511–514, 1992.

[65] V. V. Rykalin A. Pla-Dalmau, A. D. Bross and B. M. Wood. Extruded plastic scintillator for MINERvA. To appear in the proceedings of 2005 IEEE Nuclear Science Symposium and Medical Imaging Conference, El Conquistador Resort, Puerto Rico, 23-29 Oct 2005.

[66] D. Orme *et. al*. Development of mulit-pxel photon counters for the T2K long baseline experiment. *Nucl. Instr. and Meth.*, In Press, Corrected Proof, 2010.

[67] B. Hoeneisen J. Estrada, C. Garcia and P. Rubinov. MCM II and the trip chip. 2003. FERMILAB-TM-2226.

[68] G. Ward. DS-ECal Light Injection System, 2010. T2K Internal Document.

[69] A. Hatzikoutelis, N. Graham, and M. Blecher. Performance of a prototype detector for use as the sweeping magnet photon-veto in the KOPIO experiment. *JINST*, 1:P06004, 2006.

[70] D. Simon. Secondary beams for tests in the PS east experimental area. 1993. http://cern-accelerators-optics.web.cern.ch/cern-accelerators-optics/FT61DIRAC/PS

[71] A. Carver. Electron identification in and performance of the ND280 Electromagnetic Calorimeter, 2010. PhD Thesis.

[72] M. Tadel. EVE: Event visualization environment of the ROOT framework. *PoS*, ACAT08:103, 2008.

[73] A. Waldron. Ds-ECal Test Beam TFB Calibration, 2009. T2K Internal Document.

[74] R.P. Litchfield. Trip-t Calibration Status, 2010. T2K Internal Document.

[75] Y. Sirois and R. Wigmans. Effects of Long Term Low Level Exposure to Radiation as Observed in Acrylic Scintillator: Cause and Prevention of Radiation Disease in Uranium Calorimeters. *Nucl. Instr. and Meth.*, A240:262, 1985.